WARSAW UNIVERSITY OF TECHNOLOGY

PHYSICAL SCIENCES
NATURAL SCIENCES

Ph.D. Thesis

Bartosz Kozłowski, M.Sc.

$K^*(892)^0$ production in Ar+Sc collisions at CERN SPS energies measured by NA61/SHINE

Supervisor
Katarzyna Grebieszkow, Prof., Ph.D., D.Sc.

WARSAW 2025

Abstract

Title of the thesis: $K^*(892)^0$ production in Ar+Sc collisions at CERN SPS energies measured by NA61/SHINE

In this Ph.D. thesis, results of $K^*(892)^0$ resonance production in the 10% most central Ar+Sc collisions at beam momenta 40*A*, 75*A*, and 150*A* GeV/*c* are presented. Data on Ar+Sc collisions were collected by the NA61/SHINE experiment at the CERN SPS (Super Proton Synchrotron). $K^*(892)^0$ meson production was analysed in the $K^+\pi^-$ decay channel using the template method introduced in $K^*(892)^0$ analysis in *p+p* (Eur. Phys. J. C 80, 460, 2020).

For each beam momentum, two separate analyses of $K^*(892)^0$ resonance production were performed. The first analysis was conducted in four rapidity bins and a single transverse momentum bin. In this analysis, rapidity distributions and the mean multiplicities of $K^*(892)^0$ resonance were calculated. The second analysis was performed in four transverse momentum bins and a single rapidity bin. In this analysis, transverse momentum distributions, transverse mass distributions (together with corresponding fitting functions) and the mean transverse momentum were calculated.

The rapidity distributions were compared with predictions from the EPOS1.99 and FTFP-BERT models. The comparison revealed discrepancies between the model predictions and the experimental results. The values of the mean $K^*(892)^0$ multiplicities and the inverse slope parameters of transverse momentum exponential shape were compared with results from the NA49 and NA61/SHINE experiments obtained from various collision systems and energies.

Using the obtained in this analysis mean multiplicities of $K^*(892)^0$ resonances, along with results from *p+p* collisions and the mean multiplicities of charged kaons, the lower limits of the time intervals between chemical and kinetic freeze-out were estimated.

Keywords:
[NA61/SHINE, resonance production, $K^*(892)^0$, quark–gluon plasma, particle physics, nucleus-nucleus collisions, time between freeze-outs]

Streszczenie

Tytuł pracy: Produkcja $K^*(892)^0$ w zderzeniach Ar+Sc przy energiach akceleratora CERN SPS zmierzona przez NA61/SHINE

Niniejsza praca doktorska przedstawia wyniki analizy produkcji rezonansu $K^*(892)^0$ w 10% najbardziej centralnych zderzeniach Ar+Sc przy pędach wiązki 40*A*, 75*A* i 150*A* GeV/*c*. Dane zostały zebrane w ramach eksperymentu NA61/SHINE przy akceleratorze SPS (Super Proton Synchrotron) w CERN. Analiza została wykonana przy użyciu metody szablonów wyprowadzonej wcześniej w analizie w zderzeniach *p+p* (Eur. Phys. J. C 80, 460, 2020) dla kanału rozpadu $K^+\pi^-$.

Dla każdego pędu wiązki zostały wykonane dwie analizy produkcji rezonansu $K^*(892)^0$. Pierwsza analiza została wykonana w czterech przedziałach pospieszności i jednym przedziale pędu poprzecznego. W tej analizie wyznaczono rozkłady pospieszności oraz średnie krotności rezonansu $K^*(892)^0$. Druga analiza została wykonana w czterech przedziałach pędu poprzecznego i jednym przedziale pospieszności. Z tej analizy otrzymano rozkłady pędu poprzecznego, masy poprzecznej (wraz z dopasowaniami odpowiednich funkcji) oraz średni pęd poprzeczny.

Otrzymane rozkłady pospieszności zostały porównane z przewidywaniami modeli EPOS1.99 i FTFP-BERT. Porównanie wykazało niezgodności przewidywań z otrzymanymi wynikami. Uzyskane wartości średnich krotności rezonansu $K^*(892)^0$ oraz odwrotnych parametrów nachylenia w eksponencjalnym rozkładzie pędu poprzecznego porównano z wynikami eksperymentów NA49 i NA61/SHINE otrzymanymi dla różnych zderzanych systemów i energii.

Wykorzystując wyznaczone w tej analizie wartości średnich krotności rezonansu $K^*(892)^0$ razem z wynikami ze zderzeń *p+p* oraz wartościami średnich krotności naładowanych kaonów, oszacowano dolne limity czasu pomiędzy wymrożeniem chemicznym i kinetycznym.

Słowa kluczowe:
[NA61/SHINE, produkcja rezonansów, $K^*(892)^0$, plazma kwarkowo-gluonowa, fizyka cząstek elementarnych, zderzenia jądro-jądro, czas pomiędzy wymrożeniami]

Contents

CONTENTS

1 Introduction

1.1 Standard Model

Particle physics explores the fundamental building blocks of matter. The term "elementary" refers to particles with no known internal structure, meaning they are considered pointlike. Nearly all experimental results from high-energy physics align with the Standard Model of particle physics, developed in the 1970s as a result of the work of many scientists. The Standard Model is a quantum field theory that classifies all fundamental particles and describes three of the four fundamental forces [1, 2]. Standard Model describes all matter as being composed of three small sets of fundamental particles: quarks, leptons and mediators [3]. A table containing all fundamental particles with their corresponding masses, electric charges and spins, included in the Standard Model is presented in Fig. 1. Fermions is a group of fundamental particles building the matter and characterised by spin $\frac{1}{2}$. Fermions can be divided into two subgroups leptons and quarks, and three generations of particles composed by two quarks, two leptons, and their antiparticles.

Leptons are categorised based on their electric charge Q, electron lepton number L_e, muon lepton number L_μ, and tau lepton number L_τ, whereas for antileptons, these characteristics are reversed. These characteristics divide leptons into six flavours. Each generation of leptons consists of one charged lepton and one neutral lepton of the same flavour. Additionally, charged leptons in higher generations are heavier than in lower ones. The charged leptons are electron e, muon μ and tau τ, while the neutral ones are called electron neutrino ν_e, muon neutrino ν_μ and tau neutrino ν_τ.

Quarks are categorised by electric charge Q, isospin I, strangeness S, charm C, beauty B, and truth T. All quarks are charged and has fractional charge $+\frac{2}{3}|e|$[1] or $-\frac{1}{3}|e|$. Each generation of fermions consists of two quarks whose electric charges differ by e. Quarks are divided into six flavours: up quark u and down quark d (first generation), charm quark c and strange quark s (second generation), top/true quark t and bottom/beauty quark b (third generation). Similar to leptons, quarks from higher generations have bigger masses than those from the lower ones. Unlike leptons, under normal conditions, quarks cannot exist as free particles, they can only be found in bound states held together by the strong force. There are at least three combinations of quark bound states: qqq or $\overline{qqq}$ and $q\overline{q}$ (q – quark, $\overline{q}$ – antiquark), these bound states are called hadrons. Hadrons build from three quarks or antiquarks are called baryons. All baryons have baryon quantum number $B = 1$, antibaryons $B = -1$ (for quark $B = \frac{1}{3}$, for

[1] Elementary electric charge equal to electric charge of proton $1e = 1.602 \cdot 10^{-19}$ C.

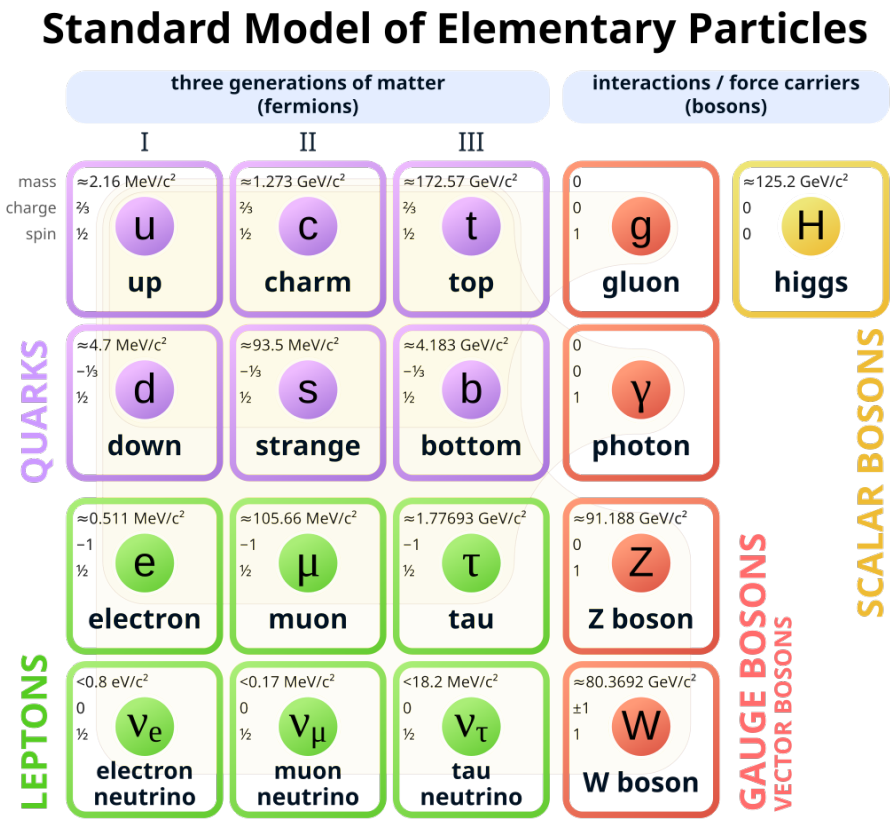

Figure 1: Table of fundamental particles in the Standard Model [4]. For the most recent values of particle masses, see Ref. [5].

antiquark $B = -\frac{1}{3}$). Examples of baryons are proton (uud), neutron (udd). Hadrons build from pair quark-antiquark are called mesons. Examples of mesons are π^- ($d\bar{u}$), π^+ ($u\bar{d}$), K^+ ($u\bar{s}$), $K^*(892)^0$ ($d\bar{s}$), $\phi(1020)$ ($s\bar{s}$). Quarks determining properties (quantum numbers) of hadrons presented above are called valence quarks, beside it hadrons are composed of gluons (carriers of strong force) and sea quarks (pairs of $q\bar{q}$ of the same flavour). Additionally, quarks have additional quantum number called colour (red, green, blue for quarks and antired, antiblue, antigreen for antiquarks) connected to strong interactions. This additional degree of freedom allows existence of hadrons like Δ^{++}, composed by three u quarks with the same spin direction ($u\uparrow u\uparrow u\uparrow$), without violating Pauli principle. All hadrons are colourless. Baryons are build from one red quark, one blue quark, and one green quark and antibaryons by one antired antiquark, one antiblue antiquark, and one antigreen antiquark. Mesons are build from one colour quark and antiquark with corresponding atnticolour (e.g. red – antired) like K^+ or from colourless combination of quarks like $\rho(770)^0$ ($\frac{u\bar{u}-d\bar{d}}{\sqrt{2}}$). All stable matter which builds our Universe consists of only fermions from the first generation of particles.

Standard Model describes three fundamental interactions: strong, weak and electromagnetic. Every interaction is characterised by the exchange of specific particles known as gauge bosons, which serve as the carriers of these interactions. The properties of these bosons are responsible for the features of interactions which they carry. Strong interactions bind quarks together within hadrons and hold neutrons and protons together within atomic nuclei. This force is mediated by eight gluons. Gluons are electrically neutral, massless particles that, similarly to the quarks, carry colour charge (more precisely, combination of a colour and an anticolour charge). Gluons interact only with particles which have colour charge, thus strong force works only on quarks and gluons. Additionally, gluons can interact with each other, and these self interactions cause that the range of strong interactions is very small. Electromagnetic force is responsible for nearly all phenomena outside the nucleus. Electromagnetic interactions occur only between electrically charged particles. They are responsible for binding electrons to nuclei in atoms, atoms in molecules and for the intermolecular forces in liquids and solids. Electromagnetic interactions are carried by photons. Photons are massless and electrically neutral, which explains the long-range nature of the electromagnetic force. Weak interactions are responsible, for example, for radioactive decay processes, and they are mediated by $W^{\pm}$ and Z^0 bosons. The masses of both bosons are approximately 100 times that of the proton, resulting in the very short range of the weak force. Additionally, the Standard Model includes the Higgs boson, which is responsible for masses of fundamental particles [1, 6].

The Standard Model is the most advanced theory describing particles, but it is not complete. It does not include gravitational force. Moreover, Standard Model treats neutrinos as massless particles when there is experimental evidence of neutrino oscillation, which proves that neutrinos should have mass [7, 8]. The Standard Model includes approximately 20 arbitrary parameters whose values must be taken from experimental results. It does not explain dark matter, dark energy, an asymmetry between matter and antimatter, why the electric charge is quantified and why electron and proton charges are equal [1].

1.2 Phase diagram of strongly interacting matter

The matter around us exists in various phases, which can change from one to another due to changes in conditions such as temperature or pressure. These phase transitions often bring about significant changes in a material's physical properties, such as elasticity, light transmission, or electrical conductivity. A familiar example is water, whose phases are partially observable in everyday life. Similarly, the strongly interacting matter also can be represented on a phase diagram. A classical phase diagram is typically shown as a relationship between pressure

and temperature. The phase diagram of strongly interacting matter, however, is depicted as a relationship between temperature T and baryochemical potential μ_B. The baryochemical potential is the thermodynamic variable which reflects the asymmetry between baryons and antibaryons. It describes how the internal energy of a system changes if one particle is added or removed while maintaining entropy and volume. When multiple types of particles exist in a system, separate chemical potentials are introduced for each particle type. The phase diagram of strongly interacting matter is shown in Fig. 2. Figure shows estimated positions of phase transition lines with points obtained from Pb+Pb and Au+Au collisions, measured by experiments at RHIC (Relativistic Heavy Ion Collider), SPS (Super Proton Synchrotron), AGS (Alternating Gradient Synchrotron) and SIS accelerators. The area near point $\mu_B = 940$ MeV and $T = 0$ MeV[2] corresponds to normal nuclear matter. The region with low baryochemical potential and temperature consists of hadron gas phase (HG), where point $\mu_B = 0$ MeV and $T = 0$ MeV represents vacuum [9]. The grey band corresponds to the first-order phase transition, which is predicted to end with the critical point (E in Fig. 2) where a second-order phase transition is anticipated. Beyond the critical point, a "cross-over" region lies where continuous but rapid changes in physical parameters occur. The area beyond the phase transition and "cross-over" lines with higher temperatures represents the quark-gluon plasma phase (QGP). The quark-gluon plasma is a state in which quarks and gluons are free to move independently inside the plasma region rather than being confined within hadrons. According to the most recent lattice calculations for $\mu_B = 0$ MeV, the transition between the hadron gas and the quark-gluon plasma state occurs at approximately $T_c = 158.9 \pm 0.6$ MeV [10]. The region with high baryochemical potential and low temperature corresponds to colour superconductors, which are predicted to only occur under extreme conditions present in the cores of neutron stars. The phase diagram of strongly interacting matter can be explored experimentally through nucleus-nucleus collisions at ultrarelativistic energies, those in which the energy per nucleon in the centre-of-mass frame far exceeds the rest mass of a nucleon in the colliding nuclei [11]. Experiments can adjust both temperature and baryochemical potential by changing collision energy and system size to explore the chosen part of the phase diagram, accessible for particular particle accelerator. Increasing collision energy causes a shift on the phase diagram towards higher temperature and lower baryochemical potential, while increasing system size causes a shift towards lower temperature [12].

[2]Temperature $T = 1$ MeV corresponds to approximately $1.2 \cdot 10^{10}$ K.

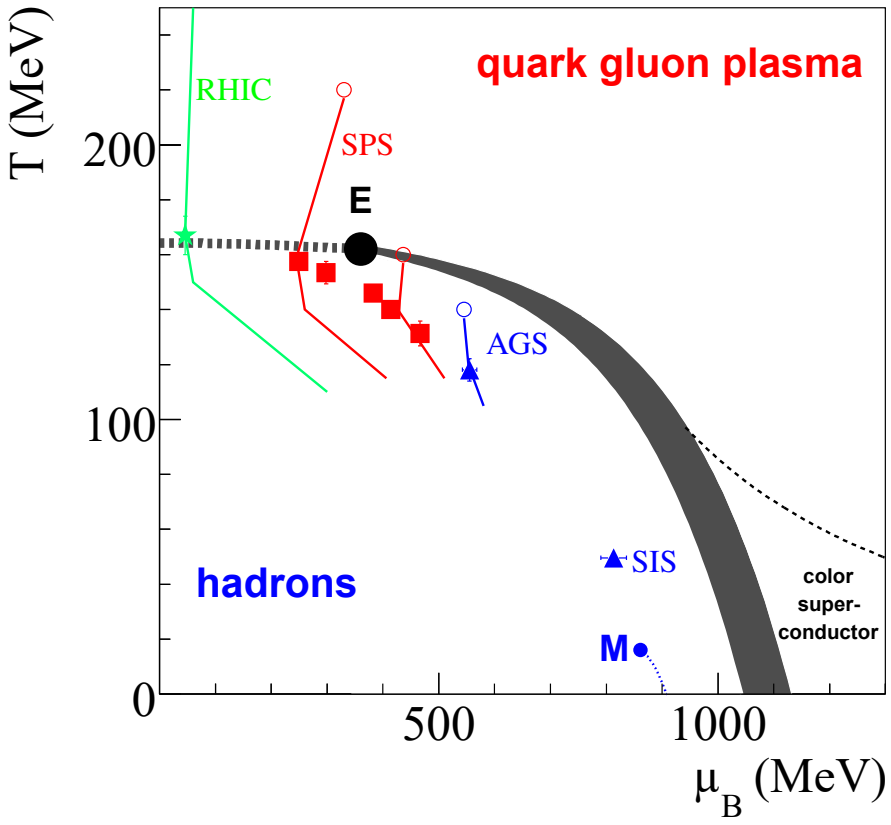

Figure 2: Sketch of the phase diagram of strongly interacting matter with points showing experimental measurements performed at RHIC, SPS, AGS, and SIS accelerators. Open symbols represent hypothetical positions of the early stage, full symbols – chemical freeze-out points (see Sec. 1.3), the end of the lines – thermal freeze-out (see Sec. 1.3), M – critical point for nuclear liquid-gas transition, E – critical point for hadron-gas and QGP transition. Open symbol placed on phase transition line (for middle SPS energy) shows onset of deconfinement point (see Sec. 1.4). Figure taken from Ref. [13].

1.3 Evolution of heavy ion collision

Analysis of heavy ion collisions is a useful tool for studying properties of the phase diagram of strongly interacting matter, elementary particles and interactions between them. The space-time evolution of such collision is presented in Fig. 3. There are two ways of conducting heavy ion collision: colliding two accelerated beams (collider experiment) or colliding an accelerated beam with a stationary target (fixed-target experiment). At the beginning, beam particles are accelerated to a speed close to the speed of light. Due to Lorentz contraction, the accelerated nuclei can be represented in the form of thin discs. Ion collisions are characterised by centrality, defined by the distance between the centres of the colliding nuclei. All nucleons involved in a collision (included in the nuclei overlap region) are known as participants, while

those that interact inelastically are specifically called wounded nucleons. Nucleons that do not participate in the collision are called spectators.

The scenario where quark-gluon plasma is produced starts with a pre-equilibrium phase, during which matter undergoes thermalization, leading to the formation of quark-gluon plasma after time $\tau_0 \approx 1$ fm/c[3] at SPS and $\tau_0 \approx 0.6$ fm/c at RHIC and LHC (Large Hadron Collider). In Fig. 3, the stage of the quark-gluon plasma is shown by an orange colour. In experiments conducted at the SPS accelerator, the QGP temperature reaches approximately $T \sim 230$ MeV, at RHIC $T \in (300;500)$ MeV, while at the LHC, the temperatures achieved are about 30% higher than at RHIC. The energy density for SPS is approximately $\varepsilon \sim 3$ GeV/fm^3, for RHIC at least $\varepsilon \sim 5$ GeV/fm^3, and for the LHC at the energy of 2.76 TeV, it is at least $\varepsilon \sim 15$ GeV/fm^3 [14]. For a comparison, the normal nuclear matter has energy density $\varepsilon \sim 0.15$ GeV/fm^3. Later, the system may go to the mixed phase (characteristic for the first-order phase transition), when plasma starts to convert into hadron gas. This process is called hadronization. The next phase is chemical freeze-out, when inelastic processes leading to the production of new particles cease and the chemical composition of the products becomes fixed. Exceptions of this rule are resonances, which can still be produced (via pseudo-elastic interactions), destroyed and regenerated also after chemical freeze-out [15–18]. The last phase of collision evolution is kinetic/thermal freeze-out. When expanding hadron gas temperature drops below T_{fo}, all interactions between produced particles end, thus the kinematic properties of the system are fixed. Particles after this last phase can be detected by the instruments used in experiments.

1.4 Onset of deconfinement

The onset of deconfinement is the energy threshold required for the creation of the quark-gluon plasma in nucleus-nucleus collisions. At such energy, even small changes in temperature and baryochemical potential can lead to dramatic changes in the properties of matter. To detect such changes, we have to search for signatures which will show differences between results from collisions where quark-gluon plasma appeared and where it did not. One of the models that predicts such structures is the Statistical Model of the Early Stage of nucleus-nucleus collision (SMES) [20].

SMES model has several assumptions, which all in detail are described in Refs. [20, 21]. The first assumption is that, in the early stage of nucleus-nucleus collisions, the production of new degrees of freedom proceeds as a statistical process. All microscopic states allowed by conservation laws are assumed to be equally probable. Consequently, the probability of realising

[3]The time 1 fm/c corresponds to approximately $3.3 \cdot 10^{-24}$ s.

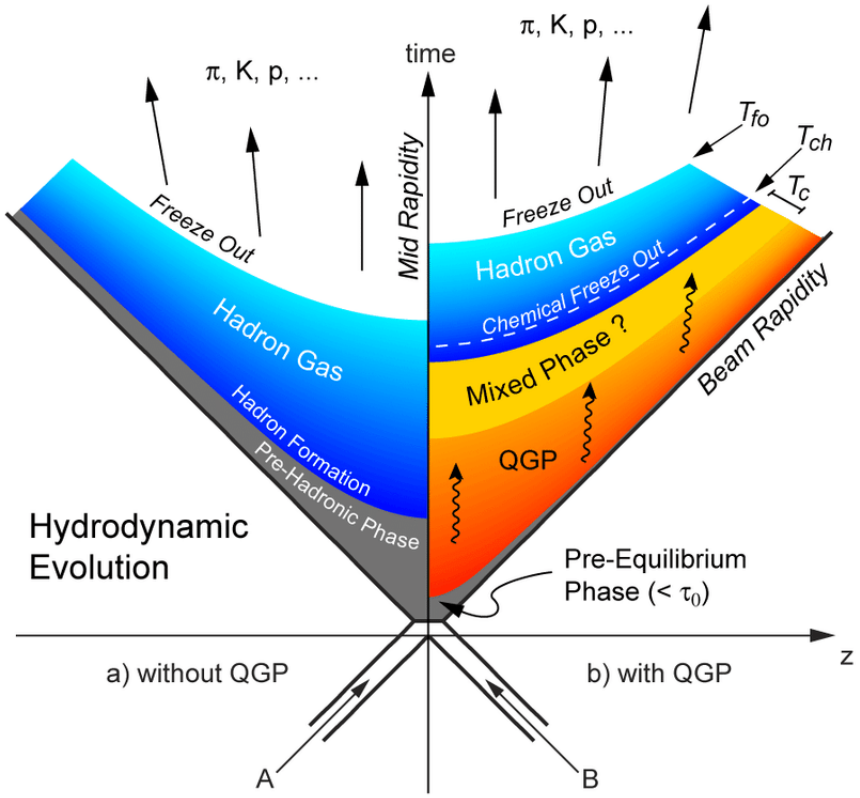

Figure 3: Space-time evolution of heavy ion collision. The left diagram shows a collision scenario without the formation of quark-gluon plasma. The right diagram shows a collision scenario with the formation of quark-gluon plasma. The τ_0 is defined as plasma formation time, T_c denotes temperature of QGP-hadron gas transition. T_{ch} and T_{fo} are chemical and thermal freeze-out temperatures, respectively. Figure taken from Ref. [19].

a specific macroscopic state is proportional to the number of its corresponding microscopic configurations. Accordingly, the probability P of a macroscopic state can be expressed as $P \sim e^S$, where S denotes the entropy associated with the macroscopic state. Since the particle production mechanism does not generate net baryon number, strangeness, or electric charge, only those states with total baryonic, flavour, and electric quantum numbers equal to zero are considered. The macroscopic properties of the system are thus fully determined by the volume in which particle production occurs, the total available energy, and the corresponding partition function. For collisions involving large nuclei, the thermodynamical approximation can be invoked, allowing the system to be characterised in terms of energy density rather than the absolute values of volume and energy. Under these conditions, the properties of the produced matter can be described by an equation of state. The SMES model assumes that in central nucleus-nucleus (A+A) collision, particle creation volume is defined as the Lorentz contracted volume occupied

by the colliding nucleons (participants) from a single nucleus, $V = \frac{V_0}{\gamma}$, where $V_0 = \frac{4}{3}\pi r_0^3 A_p$, A_p is the number of participants from a single nucleus, $r_0 = 1.3$ fm, $\gamma = \frac{\sqrt{s_{\mathrm{NN}}}}{2m_{\mathrm{N}}}$, $\sqrt{s_{\mathrm{NN}}}$ is collision centre-of-mass energy per nucleon pair, and m_{N} is nucleon mass. Another assumption is that, during A+A collision, only part of the total energy is converted into the energy of new degrees of freedom, while the remaining energy is carried by the net baryon number, which is conserved during the collision. The third assumption is that quarks and gluons are the most elementary strongly interacting particles. The model includes u, d, and s quarks and antiquarks in its calculation, while contributions of c, b, and t quarks and antiquarks are neglected due to their large masses. The masses of gluons and non-strange quarks and antiquarks are assumed to be zero, while the mass of strange quarks and antiquarks is set to 175 MeV. Finally, the strongly interacting matter produced in the early stage is assumed to undergo expansion, hadronization, and freeze-out. These later stages were not modelled in the original formulation of the SMES model. However, it was postulated that the total entropy and the total number of s quarks and antiquarks remain conserved during these stages. Additionally, it was assumed that the only process affecting the entropy content of the produced matter during the expansion phase is interaction with the baryonic subsystem, which results in a final hadronic state with a non-zero baryon number and electric charge.

SMES model assumes the existence of three phases of strongly interacting matter. First, the hadron gas phase represents the confined phase, where quarks and gluons are confined inside hadrons. Second, the quark-gluon plasma phase represents the deconfined phase, where quarks and gluons can move freely inside the QGP region. Third, the mixed phase, where both confined and deconfined states coexist.

SMES model predicts several distinctive signatures, which give information about the early stages of collisions. They can be seen by analysing the energy dependence of variables which are sensitive to change of phase in the early stage of collision evolution and do not change due to hadronization and system expansion processes.

The first structure is "kink" shown in Fig. 4. It is described by the ratio of total entropy S to the number of nucleons participating in the collision (approximately two times mass number for central nucleus-nucleus collision), depending on the Fermi energy[4] $F \approx (\sqrt{s_{\mathrm{NN}}})^{1/4}$, where $\sqrt{s_{\mathrm{NN}}}$ is collision centre-of-mass energy per nucleon pair. The majority of particles produced in high-energy interactions are π mesons (pions), thus making them the main source of information about the entropy generated during collisions. Entropy production is expected to be influenced by the type of matter present in the early stage of the collision. The deconfined

[4]Fermi energy represents the highest occupied energy level of non-interacting fermions system at temperature 0 K.

matter is anticipated to have higher entropy than confined matter. Therefore, collisions where transition to quark-gluon plasma occurs are expected to have higher entropy and increased pion production. The ratio of total entropy to the number of nucleons participating in the collision is proportional to the ratio of mean multiplicity[5] of pions $\langle\pi\rangle$ to the mean number of wounded nucleons $\langle W\rangle$. Outside the transition region, the slope of $\langle\pi\rangle$ to $\langle W\rangle$ ratio can be estimated as $\frac{\langle\pi\rangle}{\langle W\rangle} \propto g^{1/4}F$, where g is the number of degrees of freedom in the initial state. For confined phase (hadron gas) $g = 16$, while in deconfined phase (quark-gluon plasma) $g = 47.5$ [21]. The experimental measurements presented in Fig. 4 show that, in p+p collisions, the slope remains constant, while comparing two heaviest systems Au+Au (at low energies) and Pb+Pb (at high energies) we can see change of slope between these two energy regions.

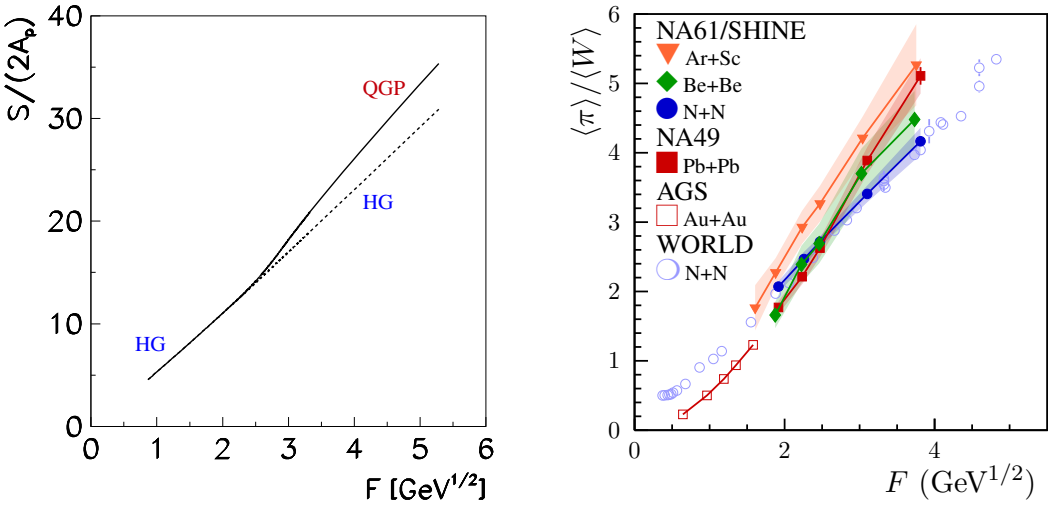

Figure 4: Left: "kink" structure predicted by the SMES model showing the phase transition [20]. Right: ratio of mean pion multiplicity $\langle\pi\rangle$ to the mean number of wounded nucleons $\langle W\rangle$ as a function of Fermi energy F taken from results of NA61/SHINE and other experiments [22].

The second signature of the onset of deconfinement is "step" shown in Fig. 5. It is described by temperature distribution as a function of the Fermi energy. When a purely confined or deconfined phase is formed at both low and high energies, the early stage temperature T should increase. During the mixed phase, the temperature is expected to remain constant and equal to the phase transition temperature; in SMES $T = T_c = 200$ MeV [20]. The measure, which may be connected with the early stage temperature, can be estimated using particles' transverse mass spectra, which can be parametrised using a simple exponential function $\frac{dn}{m_T dm_T} \cong C \cdot \exp\left(-\frac{m_T}{T}\right)$,

[5]Multiplicity is the number of particles of a given type per collision. The symbol $\langle\ldots\rangle$ denotes averaging over collisions.

where $m_T = \sqrt{m^2 + p_T^2}$[6] is transverse mass and T is inverse slope parameter of transverse mass exponential shape, corresponding to temperature of kinetic freeze-out modified by transverse flow velocity. Experimental measurements presented in Fig. 5 show the energy dependencies of the inverse slope parameters calculated using charged K mesons (kaons) at mid-rapidity[7]. The Pb+Pb and Au+Au results show the step signature around SPS energy range. Surprisingly, the plateau is also visible for intermediate (Ar+Sc) and light (Be+Be, p+p) systems.

The third signature is "horn" which can be observed in strangeness to entropy ratio as function of the Fermi energy (Fig. 6). The SMES model predicts increase of strangeness to entropy ratio with an increase of collision energy for confined state. At temperature $T = T_c$, the model predicts suppression of the strangeness to entropy ratio when crossing the phase transition line from lower energies. At the deconfined state, only a weak dependence of the strangeness to entropy ratio on the Fermi energy is expected. The "horn" signature can be obtained experimentally from the kaon to pion multiplicity ratio, where pion production is proportional to entropy, and kaon yield gives information about the strangeness. Experimental measurements presented in Fig. 6 show the multiplicity ratio of positively charged kaons to positively charged pions as a function of collision centre-of-mass energy per nucleon pair. Results of Pb+Pb and Au+Au show sharp peak around energy $\sqrt{s_{NN}} \approx 7.6$ GeV signalizing appearance of the mixed phase. Neither intermediate nor light systems show the horn signature. Results of p+p and Be+Be are very similar, while Ar+Sc and Xe+La measurements are much higher and below Pb+Pb and Au+Au.

[6]Mass m is defined as rest mass of the particle. Transverse momentum $p_T = \sqrt{p_x^2 + p_y^2}$ is component of the total momentum $p = \sqrt{p_x^2 + p_y^2 + p_z^2}$ perpendicular to the beam axis.

[7]Rapidity is kinematic property of particle defined as $y = \frac{1}{2} \ln \frac{E+p_L}{E-p_L}$, where E is the total energy of particle, and $p_L = p_z$ is component of total momentum longitudinal to the direction of the beam. At the collision centre-of-mass reference system mid-rapidity region corresponds to particles with $y \approx 0$.

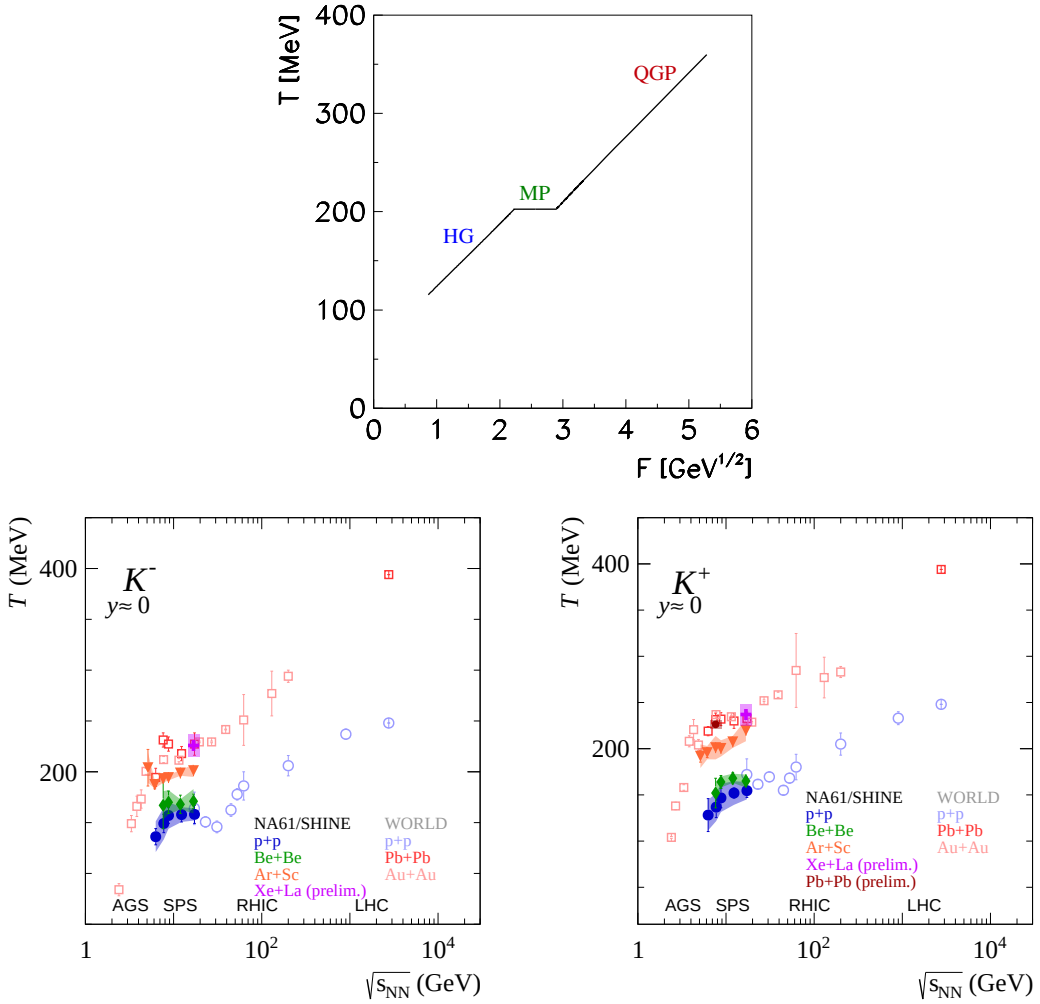

Figure 5: Top: "step" structure predicted by the SMES model showing the phase transition [20]; MP denotes mixed phase. Bottom: inverse slope parameter T of transverse mass/momentum exponential shape at mid-rapidity for charged kaons as a function of collision centre-of-mass energy per nucleon pair $\sqrt{s_{\mathrm{NN}}}$ taken from results of NA61/SHINE and other experiments [23].

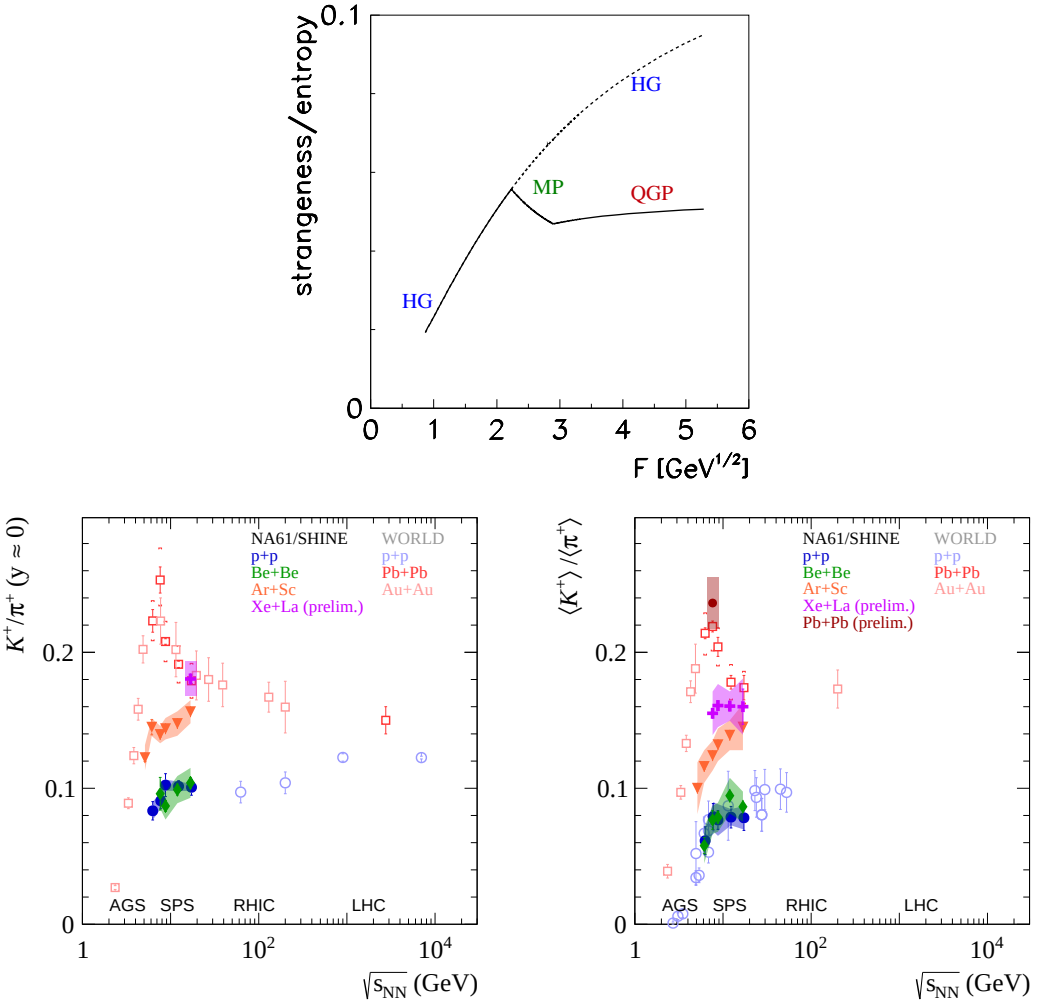

Figure 6: Top: "horn" structure predicted by the SMES model showing the phase transition [20]; MP denotes mixed phase. Bottom: charged kaon to pion ratio at mid-rapidity (left) and full 4π acceptance (right) as a function of collision centre-of-mass energy per nucleon pair $\sqrt{s_{\mathrm{NN}}}$ taken from results of NA61/SHINE and other experiments [23].

1.5 Resonances

Resonances are very short-lived states of particles. Such particles are unstable and intermediate states that appear as a peak in the scattering cross-section or decay rate of a reaction at a particular energy. The position of the peak is equivalent to the mass of the particle while the width of that peak is equivalent to the time of life. The mean lifetime of strongly decaying resonances is on the order of 10^{-23} s and it is usually presented using width Γ value according to the following equation [24]:

$$\Gamma = \hbar W = \hbar/\tau, \tag{1}$$

where:
- W is the decay rate,
- τ is the mean lifetime,
- $\hbar = h/2\pi$ is the Dirac constant.

The resonance curve peak can be described using the Breit-Wigner formula presented in Fig. 7. The two most important parameters of this function are peak energy and width, which represent mass and mean lifetime of resonance:

$$\sigma(E) = \sigma_{\max} \frac{\Gamma^2/4}{(E - E_{\mathrm{R}})^2 + (\Gamma^2/4)}, \tag{2}$$

where:
- $\sigma(E)$ is the cross section representing probability of two particles forming resonance,
- $\sigma_{\max}$ represents maximum value of the function,
- Γ is the full width at half maximum of resonance,
- E_{R} is resonance energy.

Resonances can have several decay channels. The probability that particle decays in a certain way is called the branching ratio:

$$BW = \frac{\Gamma_i}{\Gamma}, \tag{3}$$

where:
- Γ_i represents resonance width for the certain decay channel.

The width of particle which has several decay channels is calculated as the sum of the widths from all these channels:

$$\Gamma = \sum_i \Gamma_i. \tag{4}$$

Due to their short lifetimes, resonances cannot be directly observed in detectors and can

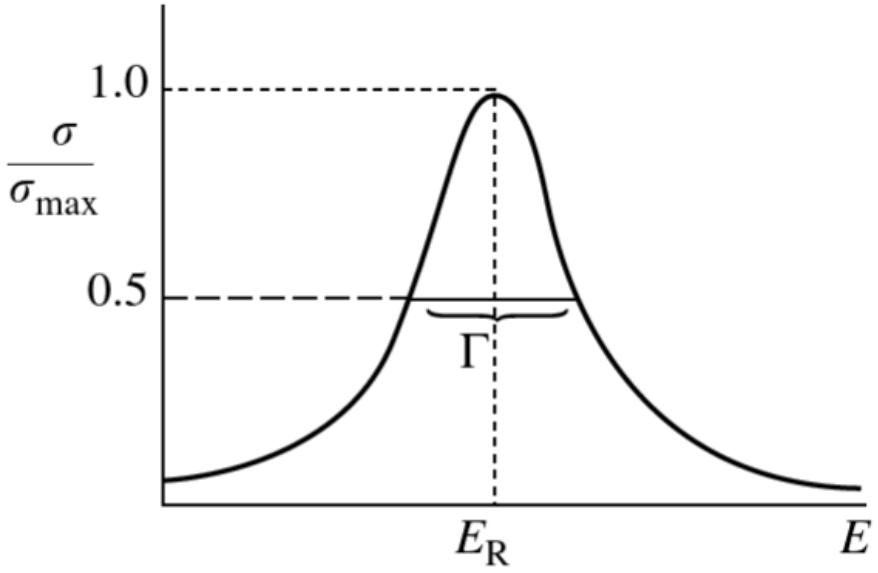

Figure 7: Breit-Wigner resonance curve [24].

only be studied by analysing their decay products. Research of properties of resonances is done by analysing invariant mass distributions of resonance decay products from the chosen decay channel.

1.6 Motivation

Resonance production is a key observable for studying the dynamics of high-energy collisions. In the dense systems created during heavy nucleus-nucleus collisions, the properties of certain resonances, such as their widths, masses, and branching ratios, are predicted to be modified due to the partial chiral symmetry restoration [25–28]. Measurements of short-lived resonance production serve as a unique tool for understanding one of the aspects of high-energy collisions, which is the time evolution of heavy ion interaction (described in Sec. 1.3). Resonance yields can help differentiate between chemical and kinetic freeze-outs [15]. The ratio of $K^*(892)^0$ to charged kaons can be used to estimate the time between freeze-outs in heavy ion collisions. The mean lifetime of $K^*(892)^0$ resonance is approximately 4.17 fm/c [5], which is comparable to the expected duration of the rescattering hadronic gas phase between the chemical and kinetic freeze-out. Resonances can only be observed through their decay products, and because of their short lifetimes, they may decay within the interacting hadron gas (before kinetic freeze-out). Consequently, momenta of the resonance decay products can be modified via elastic rescattering processes, thus preventing reconstruction of these resonances

using invariant mass analysis (Fig. 8). These effects should cause the visible suppression of the observed $K^*(892)^0$ yield.

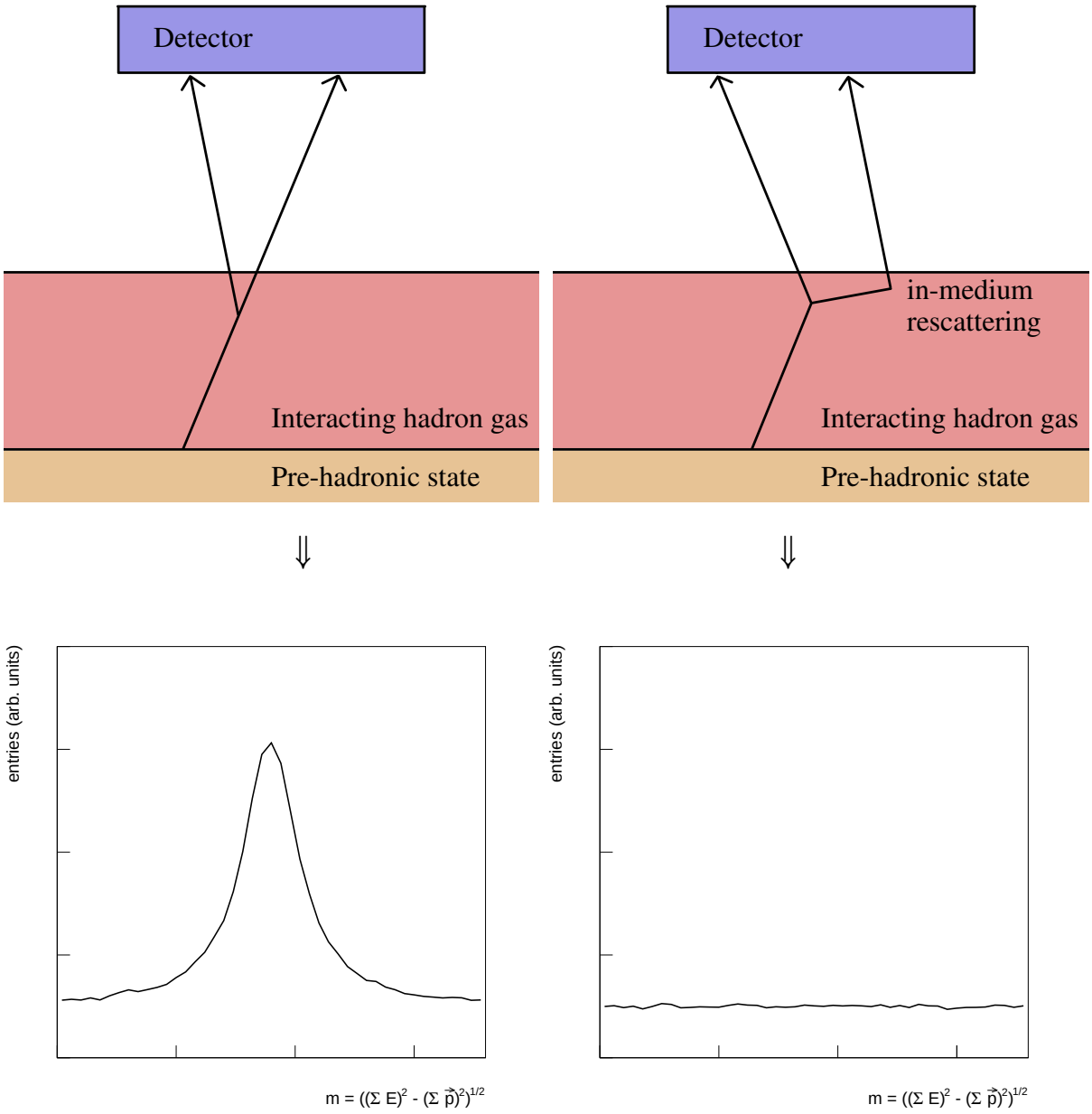

Figure 8: Mechanism of the suppression of the observed $K^*(892)^0$ production. The m represents invariant mass, E – energies of resonance decay products, and $\vec{p}$ – momentum vectors of resonance decay products. Figure inspired by Ref. [15].

The effect of $K^*(892)^0$ yield suppression was observed at SPS and RHIC energies [16, 17, 29–35]. The same phenomenon was observed by the ALICE Collaboration at LHC energies [18, 36–40]. Figure 9 shows a decrease of $K^*(892)^0$ to charged kaon ratio with an

increase in collision system size at SPS energy. Suppression is caused by increasing the time window when $K^*(892)^0$ resonance decay products can interact and change their momenta.

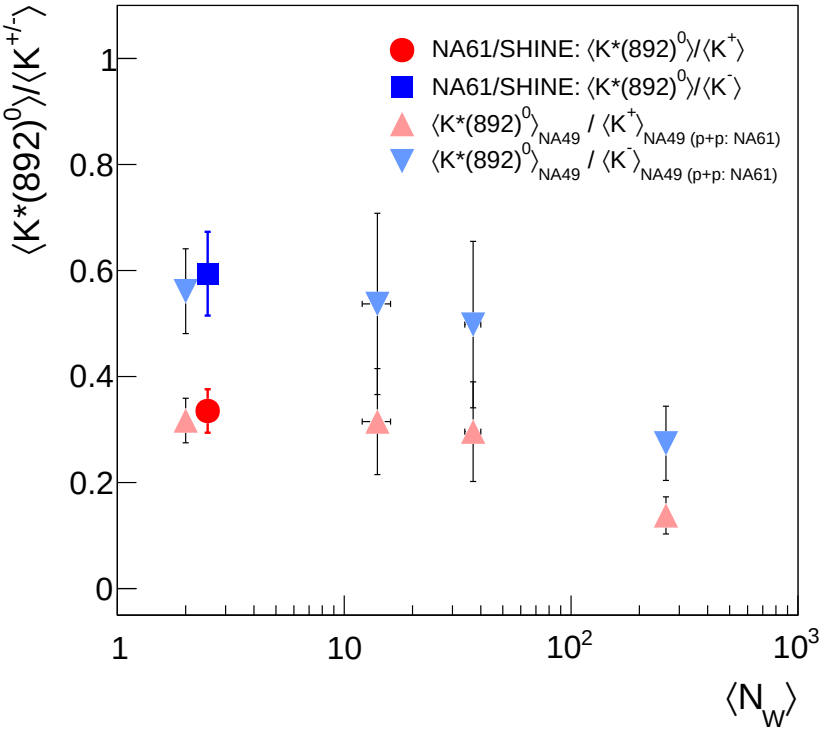

Figure 9: System size dependence of mean multiplicities of $K^*(892)^0$ to charged kaon ratio in p+p, C+C, Si+Si, and Pb+Pb collisions at beam momentum 158A GeV/c ($\sqrt{s_{\mathrm{NN}}}$ = 17.3 GeV) from results of NA61/SHINE and NA49 experiments. N_{W} represents the number of wounded nucleons. For better visibility, the NA61/SHINE points were shifted on the horizontal axis. Figure taken from Ref. [41].

Results of the STAR experiment at RHIC energy range, presented in Fig. 10, show similar suppression of K^{*0} resonance and no such effect for similar $\phi(1020)$ resonance which has factor 10 longer[8] mean lifetime than K^{*0}. The K^{*0}/K ratio in function of collision energy shows an expected decrease of value with heavier collision system of the same collision energy.

Figure 11 presents K^{*0} to charged kaon ratio obtained by the ALICE experiment at LHC energies. Results show a decrease of K^{*0}/K ratio with an increase in system size (reflected by values of $\langle dN_{\mathrm{ch}}/d\eta\rangle^{1/3}$). In the function of collision energy, $\sqrt{s_{\mathrm{NN}}}$, ratio values from p+p collisions are larger than in heavier systems. The comparison of K^{*0}/K ratio from ALICE and STAR experiments shows that measured values align between themselves according to the collision system size from which they come (heavier system, lower ratio). Results of ϕ/K

[8] $\phi(1020)$ resonance has mean lifetime τ = 46.4 fm/c and mass m = 1019.461 MeV [5].

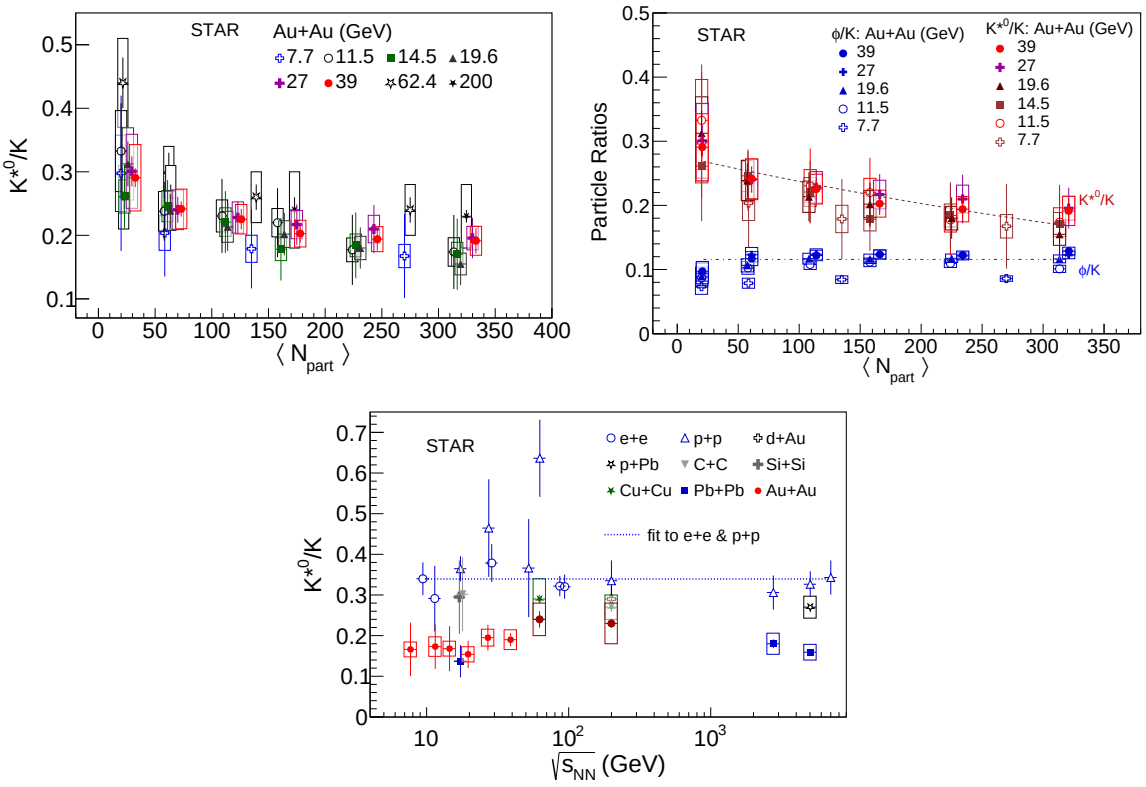

Figure 10: K^{*0} to charged kaon ratio reported by the STAR Collaboration. The K^{*0} denotes $K^*(892)^0$ and/or $\overline{K}^*(892)^0$, and K denotes K^+ and/or K^-. The top left plot presents K^{*0}/K ratio at mid-rapidity as a function of an average number of participating nucleons $\langle N_{\text{part}} \rangle$ in Au+Au interactions at collision energy $\sqrt{s_{\text{NN}}} = 7.7 - 200$ GeV. The top right plot compares K^{*0}/K and ϕ/K ratios. The bottom plot shows STAR and world data on K^{*0}/K ratio as a function of collision energy in e+e, p+p, d+Au, p+Pb, C+C, Si+Si, Cu+Cu, Au+Au, and Pb+Pb collisions. Figures are taken from Ref. [17].

ratio show almost no change of value with system size increase, and in the function of collision energy, the ratio values in p+p collisions and in heavier systems agree within uncertainties.

Similar suppression of visible production was also observed for charged $K^*(892)^{\pm}$ by the ALICE experiment at LHC energy [42], which is presented in Fig. 12.

The motivation of this Ph.D. thesis was to analyse the $K^*(892)^0$ resonance production in 0-10% central Ar+Sc collisions at beam momenta 40A, 75A, and 150A GeV/c ($\sqrt{s_{\text{NN}}} = 8.8$, 11.9, and 16.8 GeV) in decay channel $K^*(892)^0 \to K^+\pi^-$ using experimental data measured by the NA61/SHINE experiment at the CERN SPS accelerator.

[9] Pseudorapidity is an approximation of rapidity $y \approx \eta = -\ln[\text{tg}\frac{\theta}{2}]$, where θ is an angle between the particle momentum vector and the beam axis.

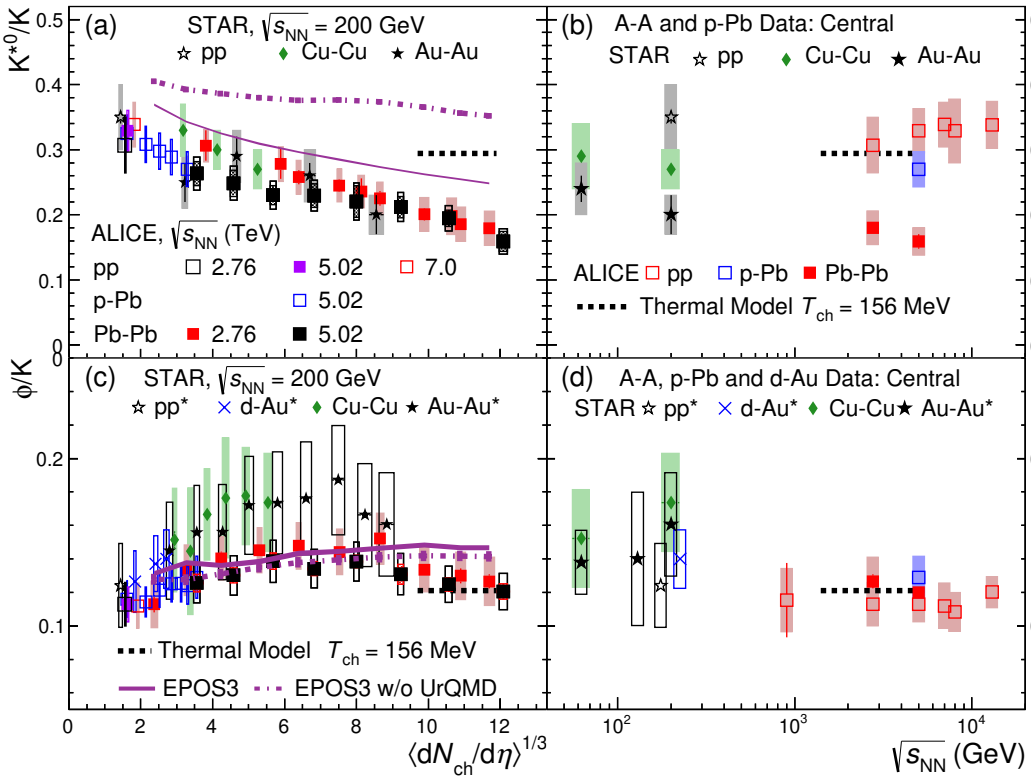

Figure 11: K^{*0}/K and ϕ/K ratios obtained by the ALICE Collaboration, compared with results of the STAR Collaboration. K^{*0} denotes $K^*(892)^0$ and $\overline{K}^*(892)^0$, and K denotes K^+ and K^-. The top plots present results of K^{*0}/K ratio. Bottom plots show results of ϕ/K ratio. Left plots present ratios as a function of pseudorapidity[9]density of charged particles $\langle dN_{ch}/d\eta \rangle^{1/3}$. The right plots show ratios as a function of collision energy $\sqrt{s_{NN}}$. Figure taken from Ref. [40].

1.7 Author's contribution to NA61/SHINE

The author of this thesis has been an active contributor to the NA61/SHINE Collaboration since 2018. He participated in many data-taking campaigns as a shifter and participated in the upgrade of NA61/SHINE detectors during Long Shutdown 2 at CERN. The author was working in the Monte Carlo group responsible for producing simulated data. Additionally, author contributed to resolving problems connected with the calibration and software of the NA61/SHINE experiment.

The author was showing his results at many collaboration meetings. After results of analysis shown in this thesis were accepted by the NA61/SHINE Collaboration as "preliminary", they have been shown at several conferences both by the author and by other members of NA61/SHINE. First, the results were shown at the "15th Workshop on Critical Point and Onset of Deconfinement" in May 2024 by NA61/SHINE member. Second, the results were shown by the author in the form of a poster and by NA61/SHINE member in a presentation at "The

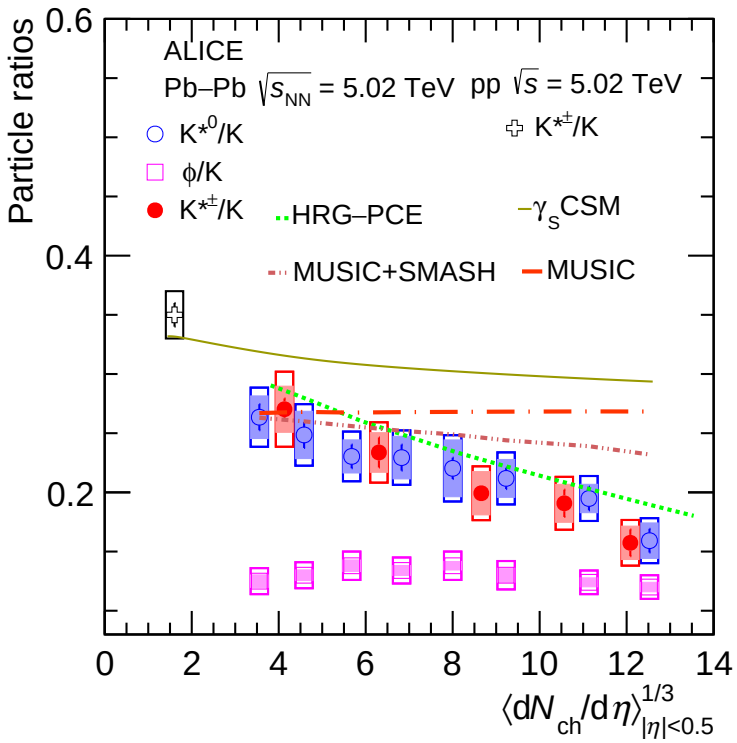

Figure 12: $K^*(892)^{\pm}/K$, K^{*0}/K, and ϕ/K ratios at mid-rapidity as a function of $\langle dN_{\rm ch}/d\eta\rangle^{1/3}$ in Pb+Pb and p+p collisions at $\sqrt{s_{\rm NN}}$ = 5.02 TeV. Figure taken from Ref. [42].

21st International Conference on Strangeness in Quark Matter" in June 2024. After that, the results were shown by the author (in presentations) at the "42nd International Conference on High Energy Physics" in July 2024 and at the "XIII International Conference on New Frontiers in Physics" in August 2024. Finally, the results were presented by NA61/SHINE members at the "New Trends in High-Energy and Low-x Physics 2024" conference in September 2024 (presentation), at the "XXXI International Conference on Ultra-relativistic Nucleus-Nucleus Collisions" in April 2025 (presentation and poster), and at the "24th Zimányi School Winter Workshop on Heavy Ion Physics" in December 2024 (presentation). The preliminary results were published in PoS ICHEP2024 [43] and NA61/SHINE Status Report [44]. The results presented in this thesis are accepted by the NA61/SHINE Collaboration as "final" and are ready to be published as an official NA61/SHINE paper.

2 NA61/SHINE experiment

NA61/SHINE (SPS Heavy Ion and Neutrino Experiment) is a fixed-target experiment located in the North Area at the CERN accelerator complex (Fig. 13). The experiment measures collisions of hadrons and ions accelerated by SPS (Super Proton Synchrotron). NA61/SHINE experiment was proposed in 2006 with the rich program to make measurements of nucleus-nucleus, proton-proton, proton-nucleus, and hadron-nucleus collisions for studying strongly interacting matter and providing reference measurements for cosmic-ray and neutrino physics [45].

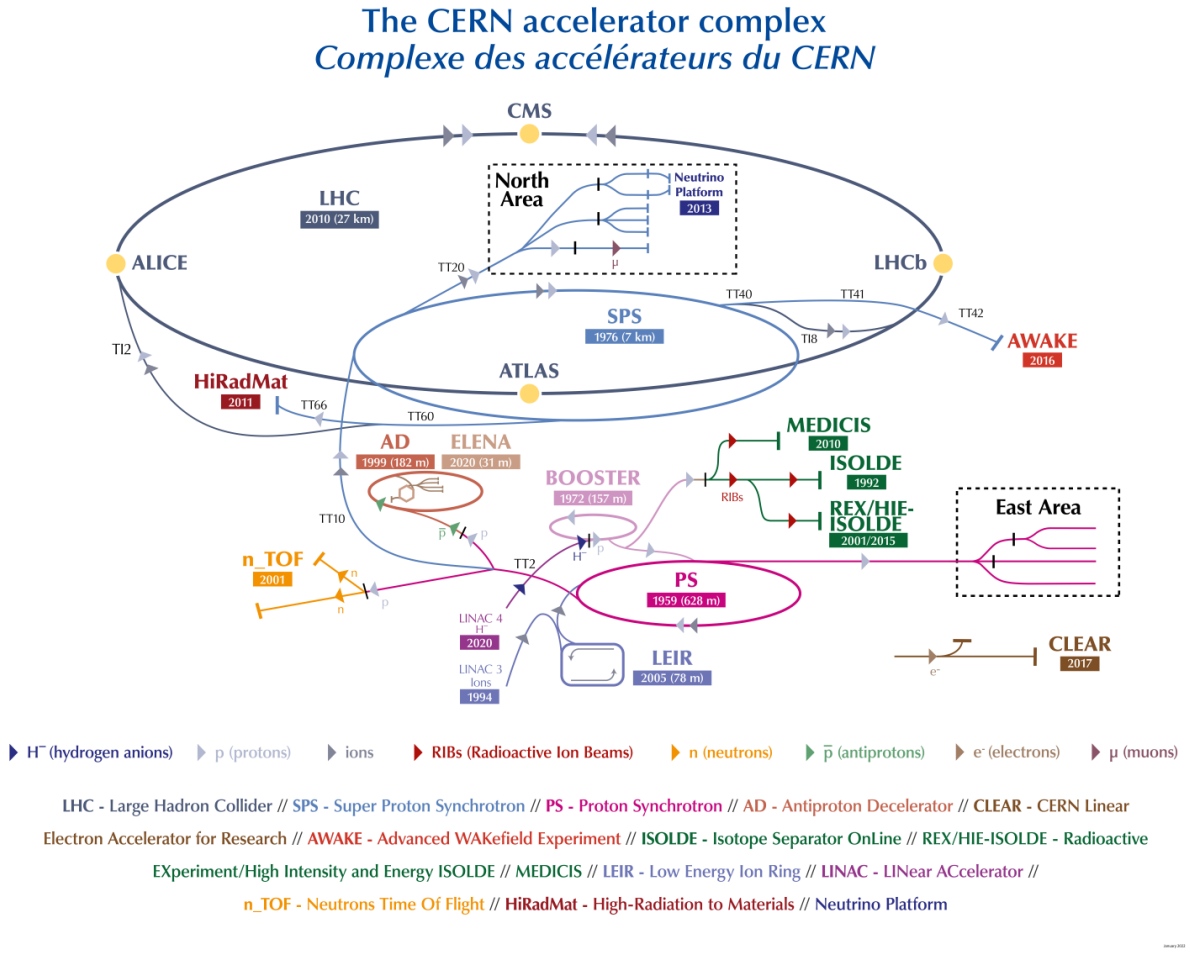

Figure 13: CERN accelerator complex in 2022 [46].

2.1 Physics program

The NA61/SHINE experiment features a diverse and rich physics program, which is divided into three parts. The first goal of the NA61/SHINE experiment is the strong interaction program. The other two physics program parts are the neutrino and cosmic-ray programs.

The strong interaction program focuses on investigating the onset of deconfinement and searching for the critical point. The NA61/SHINE experiment conducts a comprehensive study of the properties of the onset of deconfinement (looking for kink, step, and horn plots in collisions of light and intermediate-mass nuclei) by performing a beam momentum scan, which range is presented in Fig. 14. Following Particle Data Group (PDG) convention, the momenta are expressed in MeV/c or GeV/c, and masses and energies in MeV or GeV. The unit system in this thesis assumes $c = 1$. The experiment recorded interactions at beam momentum range from 13A to 150(8)A GeV/c for many collision systems p+p, p+Pb, Be+Be, Ar+Sc, Xe+La, and Pb+Pb to cover the biggest as possible area of the phase diagram of strongly interacting matter, where potential critical point is expected to be found.

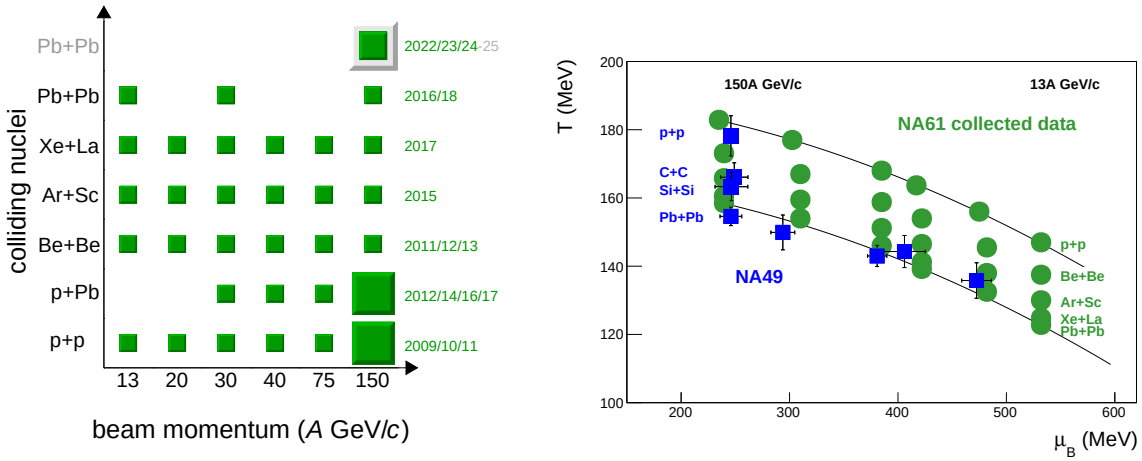

Figure 14: Left: the data collected within the NA61/SHINE strong interaction program, along with those scheduled for the future. All NA61/SHINE data with the proton beam were actually taken at 158 GeV/c. Right: NA49 and NA61/SHINE data coverage of the phase diagram of strongly interacting matter (measured and expected chemical freeze-out points). Figures taken from Ref. [47].

The neutrino program focuses on providing reference data for experiments at J-PARC and Fermilab. The NA61/SHINE experiment measures productions and cross sections of charged pions and kaons, protons, K^0_S, and Λ. These measurements allow for a more accurate estimation of the neutrino fluxes required in neutrino experiments. The NA61/SHINE experiment performs measurements of p+C collisions using a 90 cm graphite replica of the T2K target [48] (J-PARC experiment), a 120 cm graphite replica of the NuMI target [49,50] (MINOS [51,52], NOvA [53],

MINERvA [54, 55], and DUNE [56] experiments at Fermilab), and measurements of p+C, p+Be, p+Al, $\pi^{\pm}$+C, π^{+}+Be, π^{+}+Al collisions using thin targets [57, 58].

The cosmic-ray program focuses on providing reference data for Pierre-Auger [59], KASCADE [60], KASCADE-Grande [61], Telescope Array [62], IceTop [63] and satellite experiments (PAMELA [64], AMS-02 [65], CALET [66], and DAMPE [67]). The NA61/SHINE experiment measures cross sections and hadron production measurements in among others p+p, p+C, π^{-}+C, C+C/CH_2 collisions to improve cosmic-ray shower simulations used for a better understanding of cosmic-ray properties. Additionally, the measurements of nuclear fragmentation cross sections improve understanding of the cosmic-ray propagation in galaxies [68, 69].

2.2 NA61/SHINE detector

The NA61/SHINE detector [70] is a multi-purpose large acceptance hadron spectrometer designed to investigate hadron production in different types of collisions, including proton-proton, hadron-proton, hadron-nucleus, and nucleus-nucleus interactions. The detector is placed on the H2 beamline of the SPS accelerator. The layout of the NA61/SHINE detector during Ar+Sc data taking is presented in Fig. 15.

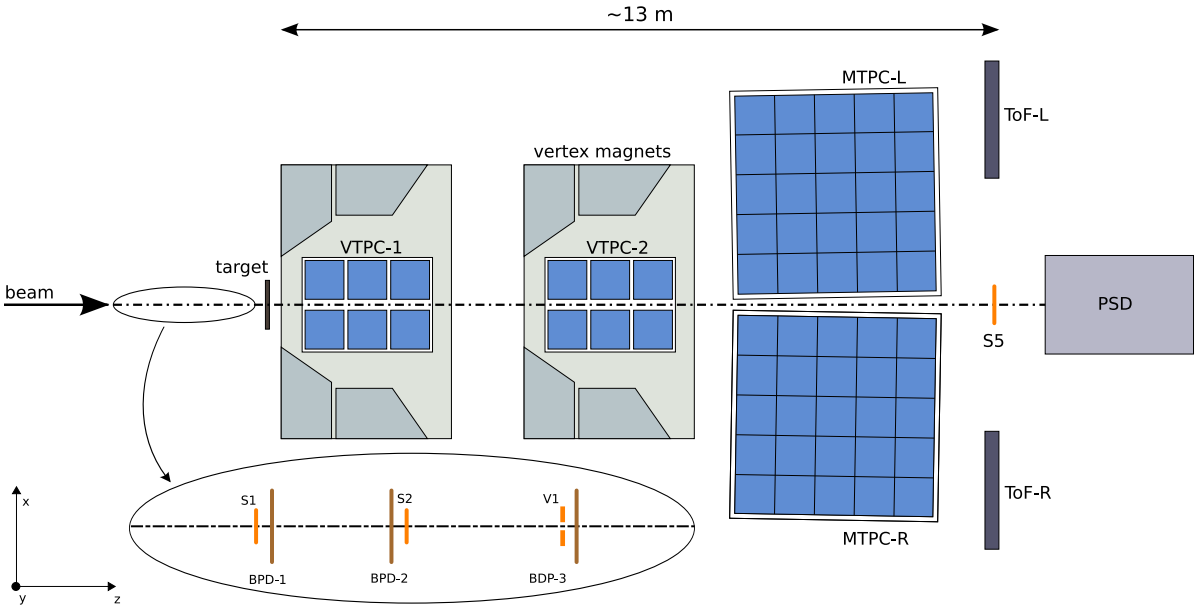

Figure 15: NA61/SHINE detector layout during Ar+Sc data taking [71]. The centre of the coordinate system of the detector is placed on the beam axis, in the middle of the VTPC-2.

The main detectors used in analysis are four large-volume Time Projection Chambers

(TPCs), which work as main tracking devices. Two smaller of them, called Vertex TPCs (VTPC-1, VTPC-2), are placed inside the magnetic field of superconducting magnets with a maximum combined bending power of 9 Tm, downstream of the target. Two bigger TPCs called Main TPCs (MTPC-L, MTPC-R) are located symmetrically on both sides of the beamline downstream of the VTPCs. The TPCs consist of a large gas volume of Ar/CO_2 mixture in proportions 90/10 for the VTPCs and 95/5 for the MTPCs, where passing charged particles leave tracks of ionisation electrons. The uniform vertical electric field is generated by a surrounding field cage composed of aluminized Mylar strips. Under the influence of the electric field, ionisation electrons drift with constant velocity towards the top plate, where their position, arrival time, and total count are measured using proportional wire chambers. Using those measurements and information about drift velocity of electrons in TPCs and magnetic field (in VTPCs) one gets a sequence of 3-dimensional measured points along the particle trajectories. Behind MTPCs, two Time of Flight (ToF-L, ToF-R) detectors are placed symmetrically on both sides of the beamline (measurements from these two detectors are not used in this analysis). All TPC detectors are used for particle identification by measuring the energy loss of passing particles. The curvature of tracks under a magnetic field measured in VTPCs is used for momentum determination. The measurements from ToF detectors are used to enhance particle identification.

The last detector downstream of the target is the Projectile Spectator Detector (PSD). It is a zero-degree hadronic calorimeter positioned 20.5 m (16.7 m) downstream of the target for Ar+Sc measurements with beam momenta of 75*A* and 150*A* GeV/*c* (40*A* GeV/*c*). It is centred in the transverse plane on the deflected beam position. The PSD detector is build from 44 modules, where the central part consists of 16 small modules with transverse dimension of 10x10 cm^2 each, while the outer part consists of 28 large modules with transverse dimension of 20x20 cm^2 each. The fragmentation of the measured transverse area allows to reduce the spectator occupancy in one module and improves the reconstruction of the reaction plane. To mitigate electronic saturation effects and shower leakage from the downstream side, a degrader in the shape of a 5 cm diameter and 10 cm long brass cylinder was positioned in front of the centre of the PSD. The purpose of PSD is selection of central collisions at the trigger level. Additionally, a calorimeter allows for precise measurements of the energy carried by projectile spectators and extraction of the number of interacting nucleons, allowing measurements of collision centrality.

The target consisted of Sc plates with transverse dimension of 2x2 cm^2 and total thickness 6 mm, placed 75 cm upstream of the VTPC-1 (~ -580 cm in the detector coordinate system) [71].

2 NA61/SHINE EXPERIMENT

Upstream of the target Beam Position Detectors (BPD-1, BPD-2, BPD-3) and beam counters (S1, S2, V1) are placed. BPDs are responsible for measurements of beam position in transverse plane and reconstruction of beam particle track. These three detectors are proportional chambers, filled with Ar/CO_2 mixture in proportions 85/15. BPDs measure the position of the beam selected by trigger in two orthogonal directions (x-z and y-z) separately, which gives 3-dimensional point in each detector. Beam counters placed upstream the target, together with beam counter S5 placed downstream of MTPCs and PSD detector are responsible for trigger definitions (T1, T2, T4 triggers). The S1, S2, and V1 scintillator detectors provide the definition of the beam before the target. The S1 counter serves as the timing reference, providing the start time for all other counters. The V1 is a veto counter featuring a 1 cm diameter hole. Beam particles are selected by the trigger system through the coincidence of signals from S1, S2, and no signal from V1 ($S1 \wedge S2 \wedge \overline{V1}$). This trigger is called T1 trigger. The T4 trigger defines minimum bias collisions (beam interacts with target) and is defined as $S1 \wedge S2 \wedge \overline{V1} \wedge \overline{S5}$. The T2 trigger is used to select central interactions. It requires the T4 trigger and that the energy signal, defined as the sum of measured signals from the 16 central modules of the PSD, to be below a threshold value ($S1 \wedge S2 \wedge \overline{V1} \wedge \overline{S5} \wedge \overline{PSD}$). The centralities of T2 events were 35% (Ar+Sc 40A GeV/c), 20% (Ar+Sc 75A GeV/c), and 23% (Ar+Sc 150A GeV/c) [72].

3 Data processing

3.1 Experimental data

Data measured by detectors (raw data) undergo calibration and reconstruction processes before they can be used for analysis. The recorded data are stored as events, with each event corresponding to a single collision and containing digitised signals from all detector components. The raw data are then processed through a reconstruction procedure, which converts these raw signals into particle trajectories and associated physical quantities. The reconstruction process consists of several main parts. First, signals measured in the same place and time are grouped, creating clusters, whose positions are determined by centre-of-gravity formation over the charge distributions of the raw signals in the cluster. These clusters represent points through which the particles measured by the TPCs have passed. Second, based on the positions of the clusters, local tracks are reconstructed in each TPC. Third, local tracks from different TPCs are matched to form global tracks. Lastly, the tracks are fitted through the magnetic field, allowing the determination of particle momenta.

3.2 Monte Carlo data

Monte Carlo (MC) simulations are utilised to correct analysis results for effects related to detector efficiency, geometrical acceptance, and the performance of reconstruction algorithms. Monte Carlo data can also be used to improve background description in the analysis of invariant mass spectra. The main model used in Monte Carlo simulations by the NA61/SHINE experiment is EPOS1.99 [73, 74] with the CRMC package [75]. Simulation is divided into two parts. First, beam + target interaction is generated by the EPOS1.99 model. Then, particles created in interaction are propagated through the detector by GEANT4 software [76–78]. Finally, obtained data are processed by dedicated detector response simulation incorporated into the NA61/SHINE implementation of the GEANT4, converting data to a format identical to the real data recorded by the detectors. In the second part, obtained data undergo the same reconstruction process as real data. This allows to compare generated data (pure MC) with reconstructed data (reconstructed MC) and estimate the efficiency of the reconstruction algorithm (see Sec. 6.3). Matching procedure allows to connect reconstructed tracks with their generated counterparts. In this process, each reconstructed track is associated with the generated track that shares the highest number of common points in TPC detectors, and the ratio of common points to all clusters in the reconstructed track is equal or higher than 50%.

4 Event and track selection

The first step of analysis is a selection of useful data for resonance study from the dataset collected by experiment. A series of event and track cuts ensures good quality of data and the selection of correctly reconstructed events. Cuts also minimise errors and uncertainties of the obtained uncorrected numbers of $K^*(892)^0$ resonances by the signal extracting procedure and improve the quality of the Monte Carlo corrections. In this section, event and track selection criteria are presented.

4.1 Event selection

All event selection cuts are applied to the T2 trigger (target inserted) sample. In the NA61/SHINE measurement campaigns, data are recorded with the target inserted (Sc in this case) as well as with the target removed. The analyses presented in this work, together with the quoted event statistics, refer exclusively to the data sets obtained with the target inserted. Inelastic Ar+Sc collision events recorded in the experiment were selected based on the following criteria:

- **WFA (beam off-time particle cut)** – This selection removes events with additional beam particles registered in close time proximity to the triggering particle, which could interact with the target or detector material. An event is rejected if an additional beam particle is detected by the S1 counter within a ± 4 μs time window relative to the primary interaction (Fig. 16), or if a minimum bias event (T4 trigger) is recorded within a ± 25 μs time window around the main triggering particle.
- **BPD cut** – This selection ensures that selected events have precise measurements of the beam trajectory. The beam signal must be detected in BPD-3 as well as BPD-2 or BPD-1. Additionally, the BPD-3 measurements in x and y planes must fall within predefined limits (Table 1) to ensure a Gaussian-like shape of the signal (Fig. 17). Beam position measurement is necessary to extrapolate the beam trajectory to the target used in the next event cut.

	BPD-3 x plane charge (arb. units)	BPD-3 y plane charge (arb. units)
Ar+Sc 150A GeV/c	$3200 < x < 8100$	$2500 < y < 7000$
Ar+Sc 75A GeV/c	$3800 < x < 7200$	$3600 < y < 6800$
Ar+Sc 40A GeV/c	$3500 < x < 8000$	$3000 < y < 7000$

Table 1: Numerical values of cuts on BPD-3 x and y plane measurements.

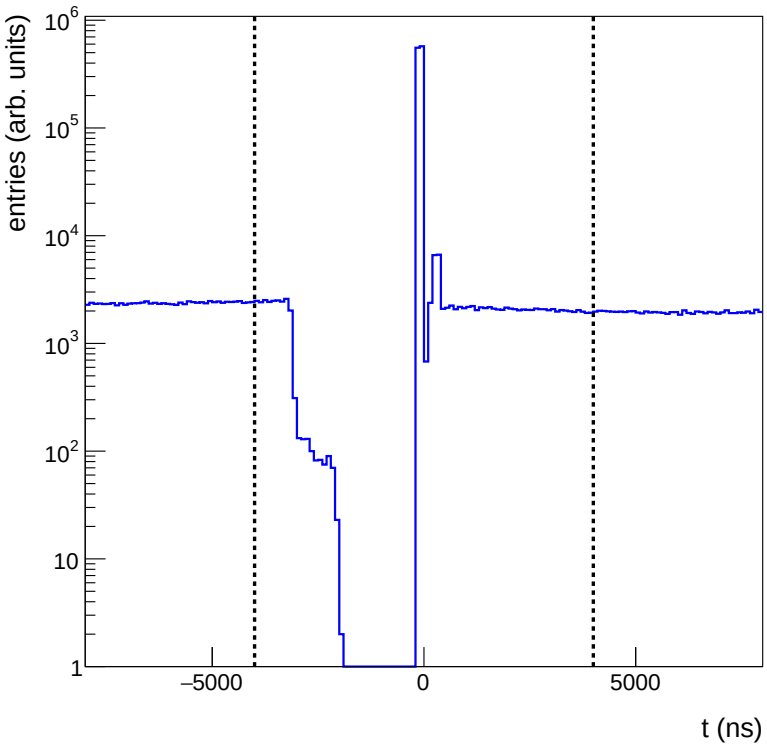

Figure 16: Time between triggering signal and registration of beam particle by S1 counter for T2 events in Ar+Sc collisions at beam momentum 150*A* GeV/*c*. Peak at zero represents the triggering particle. The black dashed lines represent cut values.

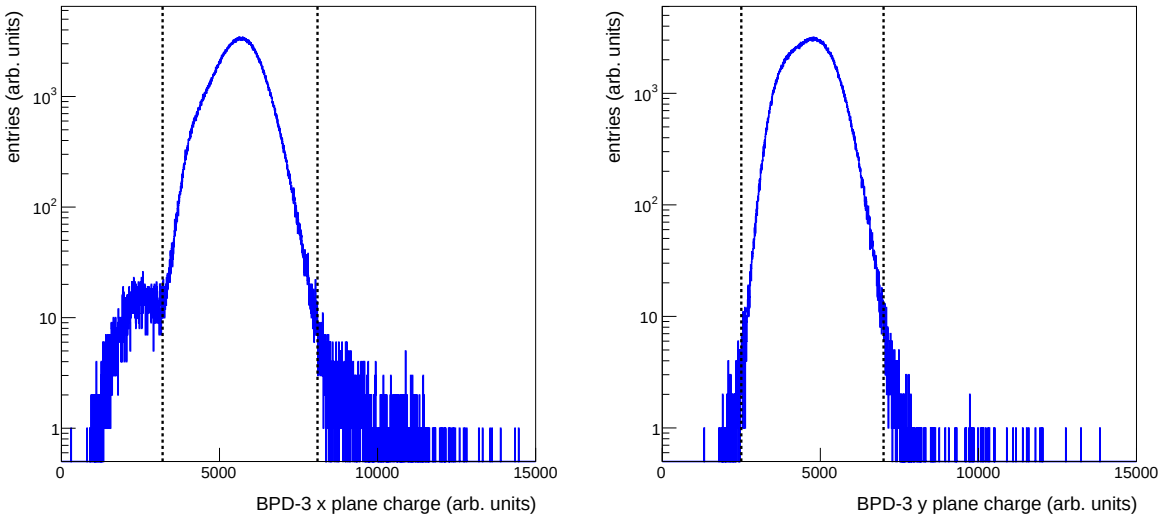

Figure 17: Charge measured by BPD-3 detector in *x* and *y* planes for T2 events after WFA cut in Ar+Sc collisions at beam momentum 150*A* GeV/*c*. The black dashed lines represent cut values.

- **Primary vertex, main vertex, and fit status** – This selection ensures the quality of the reconstructed primary vertex. The event is selected if the position of the primary vertex is correctly reconstructed. The x and y positions are taken from beam trajectory extrapolation from BPD detectors. The z position is fitted using extrapolated particle trajectories from TPC detectors. The position of the primary vertex is determined using several fitting algorithms, and the one with the best fit quality is designated as the main vertex.
- **Vertex z cut** – This selection removes all events where primary interactions are outside the target. The event is accepted if the z position of the reconstructed main vertex is within ±2 cm around the nominal target position (Fig. 18).

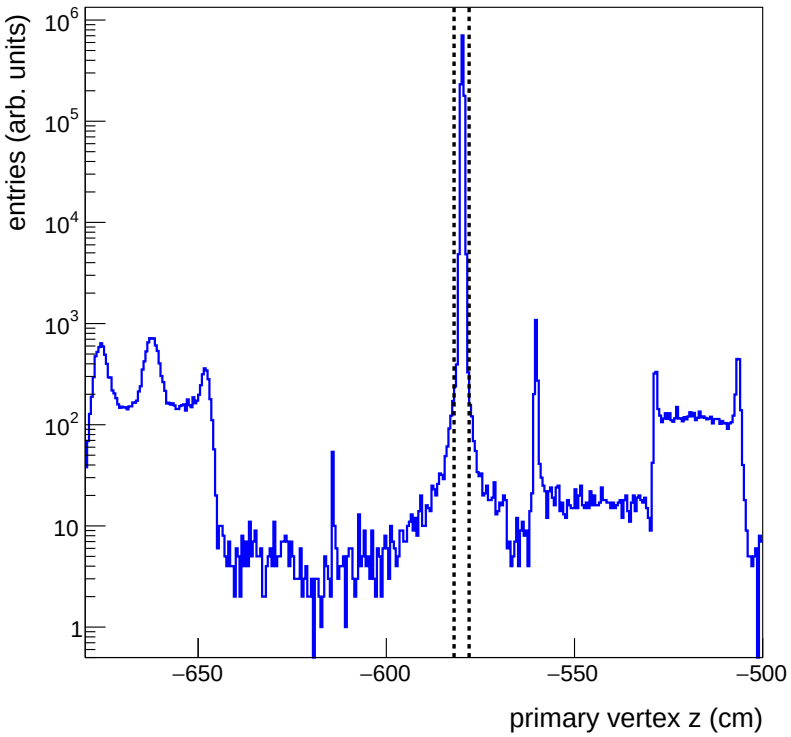

Figure 18: Position of primary vertex in z plane for T2 events in Ar+Sc collisions at beam momentum 150A GeV/c. The black dashed lines represent cut values.

- **PSD energy** – This selection accepts events where the total energies accumulated in PSD small modules $E_{\mathrm{PSD}}^{\mathrm{Small}}$ (modules 1-16) and large modules $E_{\mathrm{PSD}}^{\mathrm{Large}}$ (modules 17-28 for Ar+Sc at 40A and 75A GeV/c, and modules 21, 22, 27, 28 for Ar+Sc at 150A GeV/c, see Fig. 22) are in a certain range. The cut allows to remove events which are distorted by the PSD malfunctions (Fig. 19). Values of cuts on PSD energy are presented in Table 2.
- **Track ratio** – This selection rejects events where the number of tracks originating from the

	$E_{\mathrm{PSD}}^{\mathrm{Small}}$ (GeV)	$E_{\mathrm{PSD}}^{\mathrm{Large}}$ (GeV)
Ar+Sc 150A GeV/c	≤ 2800	[800; 5000]
Ar+Sc 75A GeV/c	≤ 1300	[300; 1700]
Ar+Sc 40A GeV/c	≤ 900	[200; 1000]

Table 2: Numerical values of cuts on measured PSD energy in small and large modules.

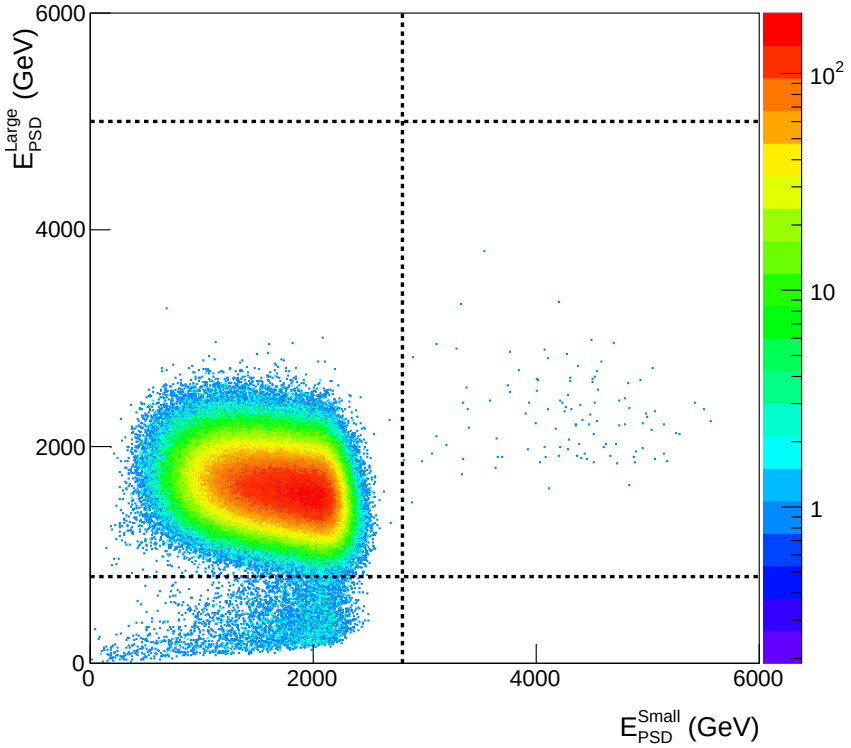

Figure 19: Distribution of energy deposited in small PSD modules (horizontal axis) and large PSD modules (vertical axis) for T2 events after WFA, BPD, primary vertex, main vertex, fit status, and vertex z cuts in Ar+Sc collisions at beam momentum 150A GeV/c. The black dashed lines represent cut values.

main vertex $N_{\mathrm{VtxTracks}}$ and the ratio of main vertex tracks to all reconstructed tracks N_{Tracks} is smaller than the designated threshold (Fig. 20). Values of cuts on main vertex tracks and the ratio of main vertex tracks to all reconstructed tracks are presented in Table 3.

- **S5 cloud** – This selection verifies whether the number of main vertex tracks is anticorrelated with energy measured in the PSD detector for less central events ($\mathrm{S5_{ADC}} > 80$). The cut is applied in $E_{\mathrm{PSD}}^{\mathrm{All}}$ (PSD small and large modules used for given beam momentum) to $N_{\mathrm{VtxTracks}}$ plane. Events are removed if they lie below a straight line defined by two points (coordinates presented in Table 4). The cut is presented in Fig. 21.
- **Centrality** – This selection chooses the 10% most central events to ensure that only the

4 EVENT AND TRACK SELECTION

	$N_{\mathrm{VtxTracks}}$	$N_{\mathrm{VtxTracks}}/N_{\mathrm{Tracks}}$
Ar+Sc 150A GeV/c	< 51	≤ 0.25
Ar+Sc 75A GeV/c	< 31	≤ 0.17
Ar+Sc 40A GeV/c	< 16	≤ 0.13

Table 3: Numerical values of cuts on number of main vertex tracks and ratio of main vertex tracks to all reconstructed tracks.

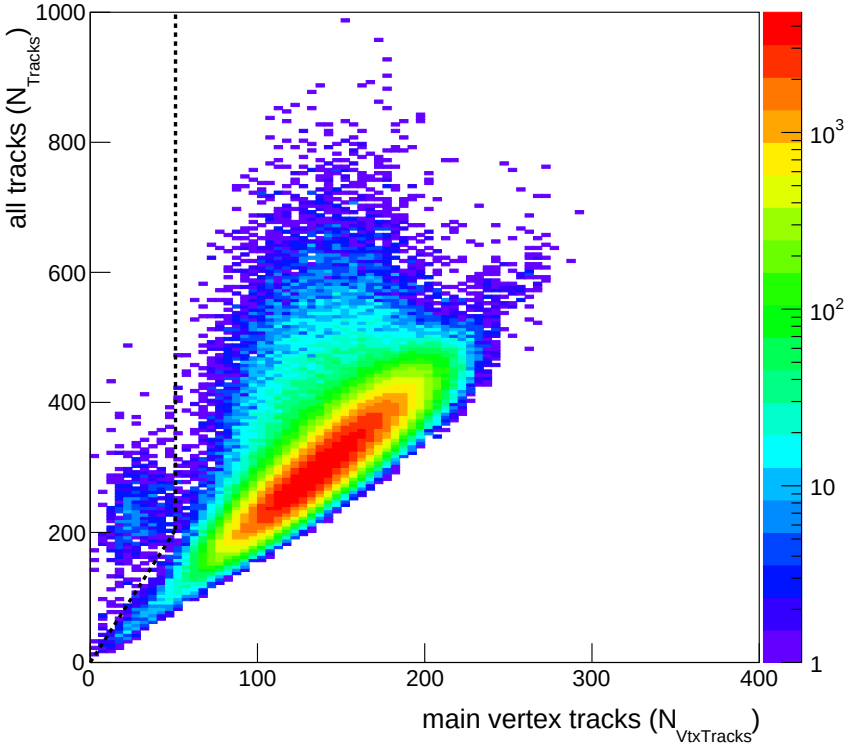

Figure 20: Distribution of number of tracks originating from the main vertex (horizontal axis) and number of all reconstructed tracks (vertical axis) for T2 events after WFA, PBD, primary vertex, main vertex, fit status, vertex z, and PSD energy cuts in Ar+Sc collisions at beam momentum 150A GeV/c. The black dashed lines represent cut values.

	Point 1 coordinate ($E_{\mathrm{PSD}}^{\mathrm{All}}, N_{\mathrm{VtxTracks}}$)	Point 2 coordinate ($E_{\mathrm{PSD}}^{\mathrm{All}}, N_{\mathrm{VtxTracks}}$)
Ar+Sc 150A GeV/c	4800, 0	0, 250
Ar+Sc 75A GeV/c	2200, 0	0, 160
Ar+Sc 40A GeV/c	1200, 0	0, 140

Table 4: Coordinates of points in $E_{\mathrm{PSD}}^{\mathrm{All}}$ and $N_{\mathrm{VtxTracks}}$ plane, used for S5 cloud cut. Events are removed if they lay below a straight line crossing these two points.

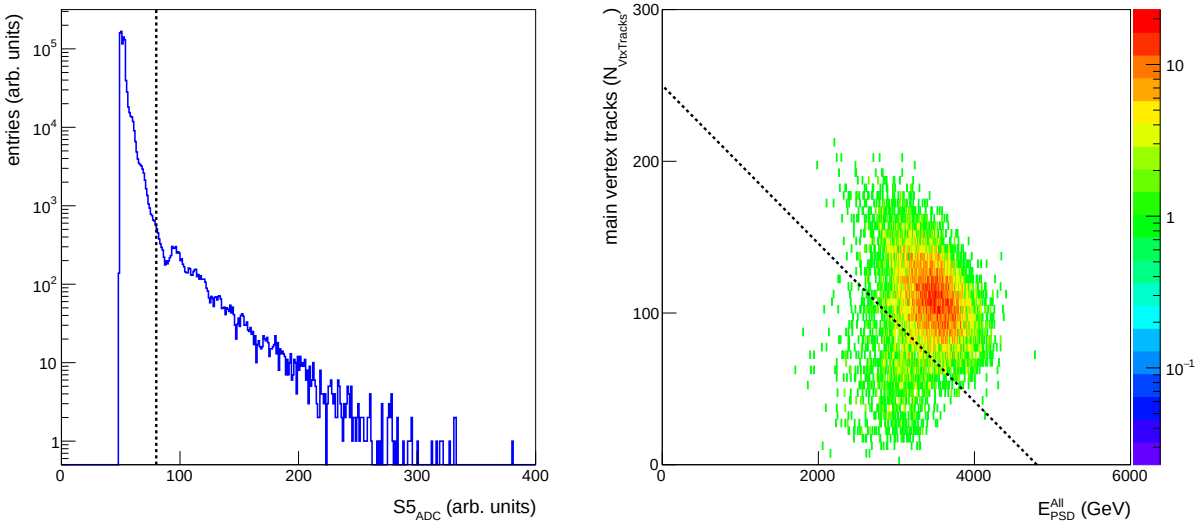

Figure 21: Left: distribution of ADC signal in S5 counter. Right: distribution of number of tracks originating from the main vertex to energy deposited in all PSD modules (for a given beam momentum; see Fig. 22) for events where $S5_{\mathrm{ADC}} > 80$. Events shown in these distributions are T2 events after WFA, BPD, primary vertex, main vertex, fit status, vertex z, PSD energy, and track ratio cuts in Ar+Sc collisions at beam momentum 150A GeV/c. The black dashed lines represent cut values.

highest multiplicity events are selected. Centrality is defined as percentile of collisions with the highest multiplicity (measured by detector) or with the highest number of participants. Central collisions have the highest number of participants, whereas the peripheral ones have the lowest number of participants. Collision centrality can also be defined using the impact parameter, defined as the distance between the centres of the beam and the target nucleus at the moment of interaction/overlap. The next method for defining centrality is based on measuring the number of wounded nucleons. Both last methods cannot be directly applied under experimental conditions. The centrality value, in NA61/SHINE experimental conditions is estimated using energy measured by PSD calorimeter E_{PSD}. The E_{PSD} corresponds to forward energy E_{F}, which is defined as the sum of energies of all particles produced in collision in the forward rapidity region, defined by acceptance maps [79]. Since the PSD measures the energy of projectile spectators as well as particles produced in the collision, its performance must be optimised to ensure accurate centrality determination. To achieve this, the correlation between the energy deposited in the PSD modules and the total multiplicity of charged particles registered by the TPCs is measured. If results show anticorrelation between energy in module and multiplicity of charged particles, it means that the module measures mainly energy of projectile spectators. The selection of PSD modules used for centrality determination (modules with visible anticorrelation) at a given beam momentum is shown in Fig. 22. The

numerical values of E_{PSD} corresponding to the 10% most central collisions are presented in Table 5. Figure 23 shows example E_{PSD} distribution for Ar+Sc collisions at 150A GeV/c.

	E_{PSD} (GeV)
Ar+Sc 150A GeV/c	≤ 2276.0
Ar+Sc 75A GeV/c	≤ 1290.6
Ar+Sc 40A GeV/c	≤ 665.6

Table 5: Numerical values of centrality cut for 10% most central events. Taken from Ref. [72].

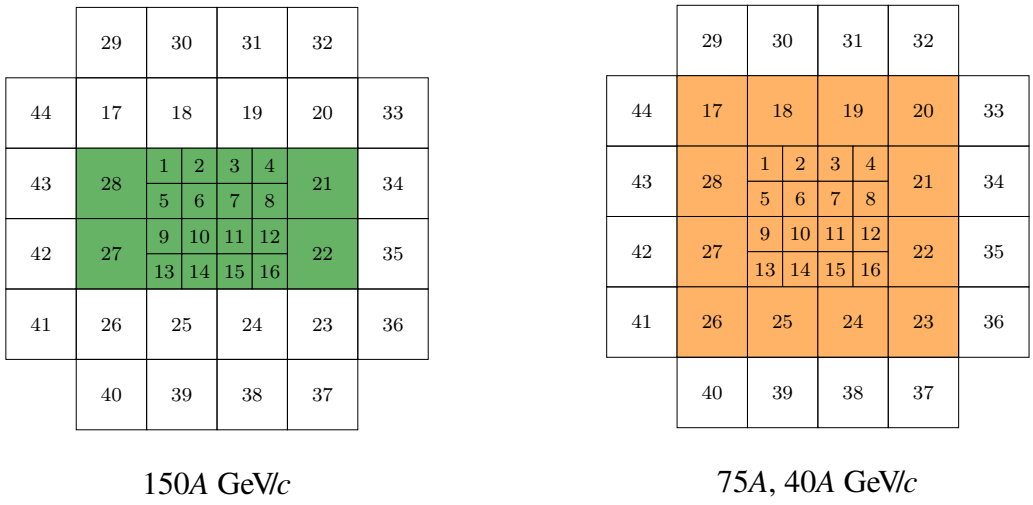

Figure 22: Schematic diagrams showing the PSD modules used in centrality selection at the respective beam momenta. Figure taken from Ref. [22].

The numerical values of the impact of cuts on statistics of events for each analysed beam momentum are presented in Table 6.

The reconstructed Monte Carlo data are subjected to similar event selection criteria as the experimental data. Due to limitations in the simulation, not all cuts applied to the real data can be replicated in the Monte Carlo analysis. Centrality selection in the Monte Carlo data is performed using both E_{PSD} (reconstructed MC) and E_{F} (pure MC). Both quantities are calculated using an internal numerical code named *Fast PSD Simulator*. The E_{PSD} calculated by this code is a simulated forward energy modified by PSD detector effects like measurement resolution, energy leakage, and energy smearing. Table 7 shows numerical values of E_{PSD} and E_{F} corresponding to the 10% most central events for each analysed beam momentum. The centrality cuts for MC data were determined by taking 10% most central events (having the smallest E_{PSD} or E_{F}). The E_{F} cut values were obtained from the generated minimum bias events, while the E_{PSD} cut values were determined from the generated and reconstructed minimum bias events after

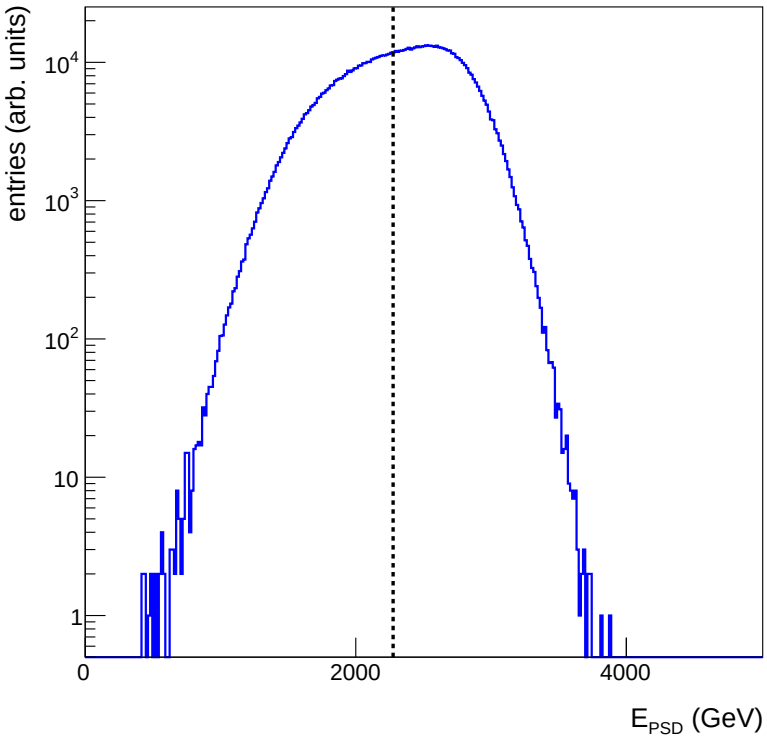

Figure 23: Distribution of energy deposited in selected PSD modules (see Fig. 22) for T2 events after all event cuts beside centrality selection in Ar+Sc collisions at beam momentum 150*A* GeV/*c*. The black dashed line represents cut value.

	Ar+Sc 40*A* GeV/*c*	Ar+Sc 75*A* GeV/*c*	Ar+Sc 150*A* GeV/*c*
T2 trigger (target inserted)	$6.54 \cdot 10^6$	$3.12 \cdot 10^6$	$1.16 \cdot 10^6$
WFA	$5.54 \cdot 10^6$	$2.63 \cdot 10^6$	$9.63 \cdot 10^5$
BPD cut	$5.36 \cdot 10^6$	$2.54 \cdot 10^6$	$9.47 \cdot 10^5$
Primary vertex, main vertex, and fit status	$4.93 \cdot 10^6$	$2.41 \cdot 10^6$	$9.37 \cdot 10^5$
Vertex z cut	$4.61 \cdot 10^6$	$2.35 \cdot 10^6$	$9.22 \cdot 10^5$
PSD energy	$4.57 \cdot 10^6$	$2.32 \cdot 10^6$	$9.18 \cdot 10^5$
Track ratio	$4.55 \cdot 10^6$	$2.32 \cdot 10^6$	$9.17 \cdot 10^5$
S5 cloud	$4.54 \cdot 10^6$	$2.31 \cdot 10^6$	$9.16 \cdot 10^5$
Centrality	$1.29 \cdot 10^6$	$1.16 \cdot 10^6$	$3.94 \cdot 10^5$

Table 6: Number of events after each event cut for Ar+Sc collisions at beam momenta 40*A*, 75*A*, and 150*A* GeV/*c* ($\sqrt{s_{\mathrm{NN}}}$ = 8.8, 11.9, and 16.8 GeV).

primary vertex, main vertex, and fit status cuts. The impact of event selection on reconstructed Monte Carlo data statistics is shown in Table 8. The pure (generated) Monte Carlo data are subjected only to centrality selection (based on E_F).

	E_{PSD} (GeV)	E_F (GeV)
Ar+Sc 150A GeV/c	≤ 2343.76	≤ 4161.72
Ar+Sc 75A GeV/c	≤ 1244.35	≤ 2122.40
Ar+Sc 40A GeV/c	≤ 690.13	≤ 1175.53

Table 7: Numerical values of centrality cut for the 10% most central events in Monte Carlo data.

	Ar+Sc 40A GeV/c	Ar+Sc 75A GeV/c	Ar+Sc 150A GeV/c
Simulated data	$1.92 \cdot 10^7$	$1.91 \cdot 10^7$	$1.85 \cdot 10^7$
Primary vertex, main vertex, and fit status	$1.87 \cdot 10^7$	$1.85 \cdot 10^7$	$1.77 \cdot 10^7$
Vertex z cut	$1.76 \cdot 10^7$	$1.73 \cdot 10^7$	$1.64 \cdot 10^7$
Centrality	$1.87 \cdot 10^6$	$1.85 \cdot 10^6$	$1.77 \cdot 10^6$

Table 8: Number of events after each event cut for reconstructed Monte Carlo data at beam momenta 40A, 75A, and 150A GeV/c ($\sqrt{s_{NN}}$ = 8.8, 11.9, and 16.8 GeV).

4.2 Track selection

Tracks in each accepted event were selected using the following criteria:

- **Track quality** – This selection removes tracks which were not correctly reconstructed or were not connected to the main interaction vertex.
- **Number of points in all TPC detectors** – This selection ensures good quality of reconstructed tracks. The cut removes tracks with a number of reconstructed points in all TPC detectors smaller than 30. The distribution of the number of points in the reconstructed track registered by all TPCs is presented in Fig. 24.
- **Number of points in VTPC detectors** – This selection ensures good quality of momentum reconstruction. The cut removes tracks with a number of reconstructed points in VTPC detectors smaller than 15. The distribution of the number of points in the reconstructed track registered by VTPCs is presented in Fig. 25.
- **Impact parameter** – This selection removes tracks if the distance between the extrapolated track (to the interaction plane) and the main interaction vertex in both x and y axes meets the

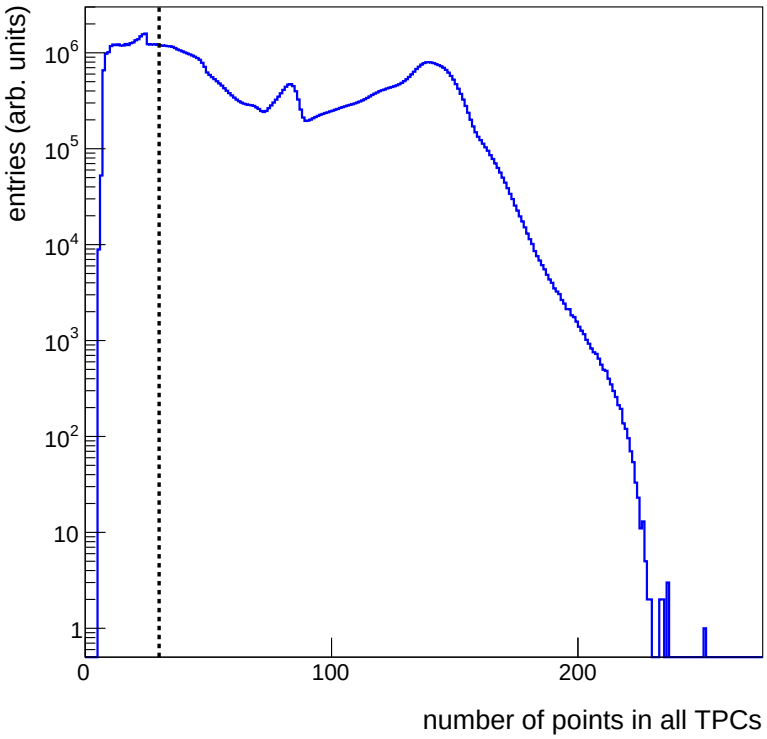

Figure 24: Distribution of number of points in reconstructed track measured by all TPC detectors in Ar+Sc collisions at beam momentum 150*A* GeV/*c* after event selection and track quality cut. The black dashed line represents cut value.

condition: $|b_x| > 4$ cm and $|b_y| > 2$ cm. The distribution of impact parameter in x and y plane is presented in Fig. 26.

- **Transverse momentum p_T** – This selection removes all tracks with transverse momentum (perpendicular to beam direction) higher than 1.5 GeV/*c*.
- **Total momentum p_{lab}** – This selection improves the quality of identification by removing particles close to the cross-over region of Bethe-Bloch curves (see Chapter 5). The cut removes all tracks with total momentum in the laboratory reference frame lower than 3 GeV/*c*.

Track selection performed on a pair of particles:

- **Opening angle** – angle between two momenta vectors from combination of two tracks $(K^+\pi^-)$ in laboratory reference frame has to be equal to or higher than $1°, 1.5°, 2°$ for Ar+Sc at 150*A*, 75*A*, and 40*A* GeV/*c*, respectively. This selection reduces background on the left tail of $K^*(892)^0$ distribution (see example in Fig. 27).

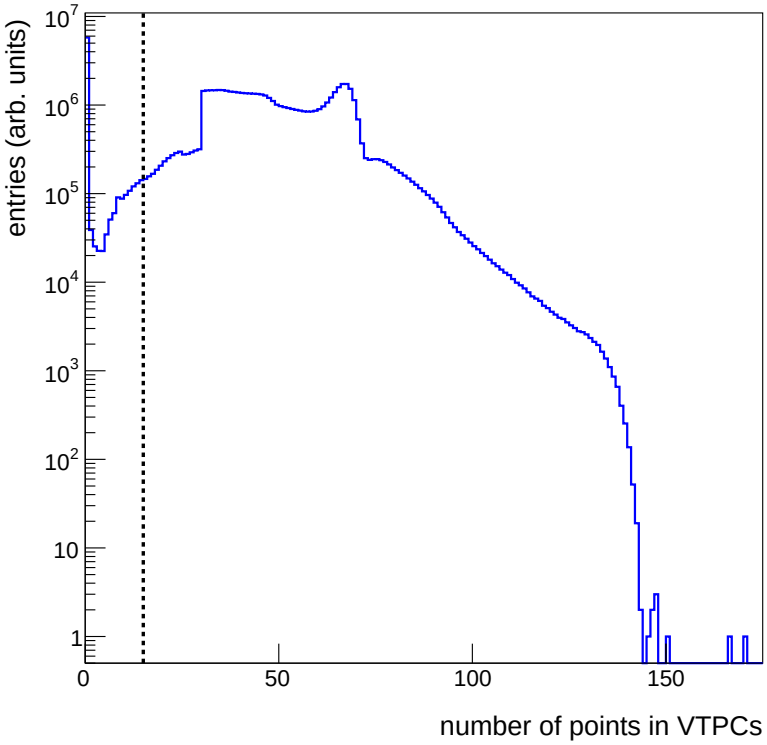

Figure 25: Distribution of number of points in reconstructed track measured by VTPC detectors in Ar+Sc collisions at beam momentum 150*A* GeV/*c* after event selection and track quality cut. The black dashed line represents cut value.

The numerical values of the impact of cuts on the statistics of tracks for each analysed beam momentum are presented in Table 9.

The reconstructed Monte Carlo data are subjected to the same track selection criteria as the experimental data. The impact of track cuts on statistics is shown in Table 10. No track selection cuts are applied to the pure Monte Carlo data.

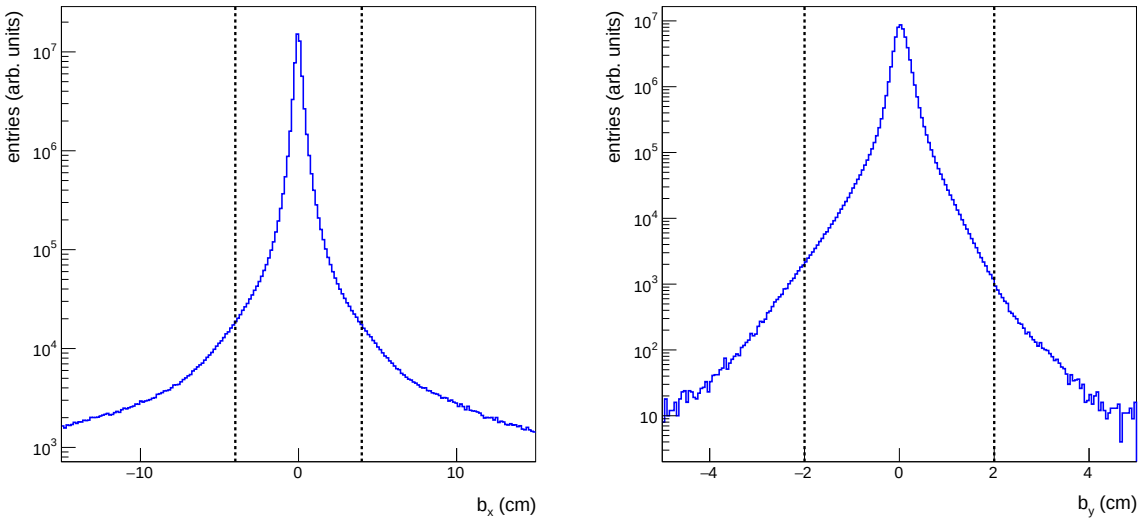

Figure 26: Distribution of distance between extrapolated track (to interaction plane) and main interaction vertex in x (left) and y (right) plane in Ar+Sc collisions at beam momentum 150A GeV/c after event selection and track quality cut. The black dashed lines represent cut values.

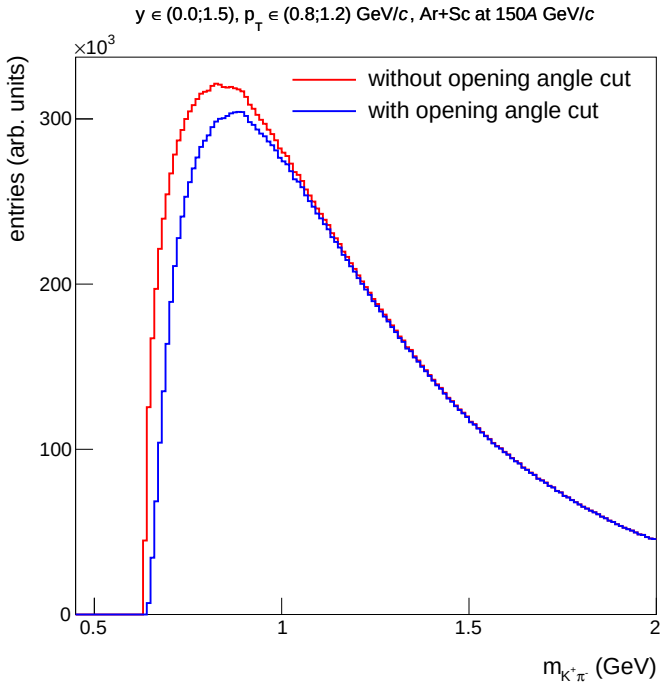

Figure 27: Invariant mass distribution of combination of $K^+\pi^-$ coming from the same event in Ar+Sc collisions at beam momentum 150A GeV/c. The red line represents the distribution without the opening angle cut, while the blue line with the angle cut applied. The spectra were created from data after applying all event and track cuts.

	Ar+Sc 40*A* GeV/*c*	Ar+Sc 75*A* GeV/*c*	Ar+Sc 150*A* GeV/*c*
Registered	$7.10 \cdot 10^8$	$7.40 \cdot 10^8$	$2.04 \cdot 10^9$
Track quality	$1.53 \cdot 10^8$	$1.92 \cdot 10^8$	$9.32 \cdot 10^7$
TPC points	$1.08 \cdot 10^8$	$1.37 \cdot 10^8$	$6.48 \cdot 10^7$
VTPC points	$9.92 \cdot 10^7$	$1.23 \cdot 10^8$	$5.80 \cdot 10^7$
Impact parameter	$9.64 \cdot 10^7$	$1.20 \cdot 10^8$	$5.69 \cdot 10^7$
p_{T}	$9.57 \cdot 10^7$	$1.19 \cdot 10^8$	$5.66 \cdot 10^7$
p_{lab}	$4.52 \cdot 10^7$	$7.23 \cdot 10^7$	$4.24 \cdot 10^7$

Table 9: Number of tracks after each track cut for Ar+Sc collisions at beam momenta 40*A*, 75*A*, and 150*A* GeV/*c* ($\sqrt{s_{\mathrm{NN}}}$ = 8.8, 11.9, and 16.8 GeV).

	Ar+Sc 40*A* GeV/*c*	Ar+Sc 75*A* GeV/*c*	Ar+Sc 150*A* GeV/*c*
Simulated	$1.06 \cdot 10^9$	$2.00 \cdot 10^9$	$4.06 \cdot 10^9$
Track quality, charge	$2.33 \cdot 10^8$	$3.10 \cdot 10^8$	$4.04 \cdot 10^8$
TPC points	$1.69 \cdot 10^8$	$2.27 \cdot 10^8$	$2.91 \cdot 10^8$
VTPC points	$1.54 \cdot 10^8$	$2.03 \cdot 10^8$	$2.64 \cdot 10^8$
Impact parameter	$1.50 \cdot 10^8$	$1.99 \cdot 10^8$	$2.59 \cdot 10^8$
p_{T}	$1.49 \cdot 10^8$	$1.99 \cdot 10^8$	$2.58 \cdot 10^8$
p_{lab}	$6.79 \cdot 10^7$	$1.21 \cdot 10^8$	$1.95 \cdot 10^8$

Table 10: Number of tracks after each track cut for reconstructed Monte Carlo data at beam momenta 40*A*, 75*A*, and 150*A* GeV/*c* ($\sqrt{s_{\mathrm{NN}}}$ = 8.8, 11.9, and 16.8 GeV).

5 Particle identification

Identification of particles used in this analysis was performed using information provided by TPC detectors. Namely, it was done using distributions of energy loss ($\mathrm{d}E/\mathrm{d}x$) and total momentum (p_{lab}) in the laboratory reference frame. The K^+ and π^- candidates used in the analysis were accepted if their $\mathrm{d}E/\mathrm{d}x$ values were located in a certain range around the nominal Bethe-Bloch values. The range is described as a multiple of σ, where σs are the standard deviations of Gaussian fits performed on $\mathrm{d}E/\mathrm{d}x$ distributions at chosen momentum ranges. The values of σ for K^+ and π^- were taken from Ref. [41] ($\sigma_{K^+} = 0.044$; $\sigma_{\pi^-} = 0.052$). The range when particles are accepted as K^+ or π^- are: $1.5\sigma_{K^+}$, $2\sigma_{\pi^-}$. Figures 28, 29, and 30 present $\mathrm{d}E/\mathrm{d}x$ versus $\log(p_{\mathrm{lab}}/(\mathrm{GeV}/c))$ distributions of positively and negatively charged particles before and after identification cut in Ar+Sc collisions at beam momenta 40A, 75A, and 150A GeV/c. In reconstructed Monte Carlo data, instead of cuts on $\mathrm{d}E/\mathrm{d}x$ versus $\log(p_{\mathrm{lab}}/(\mathrm{GeV}/c))$, a matching procedure is used (see Sec. 3.2).

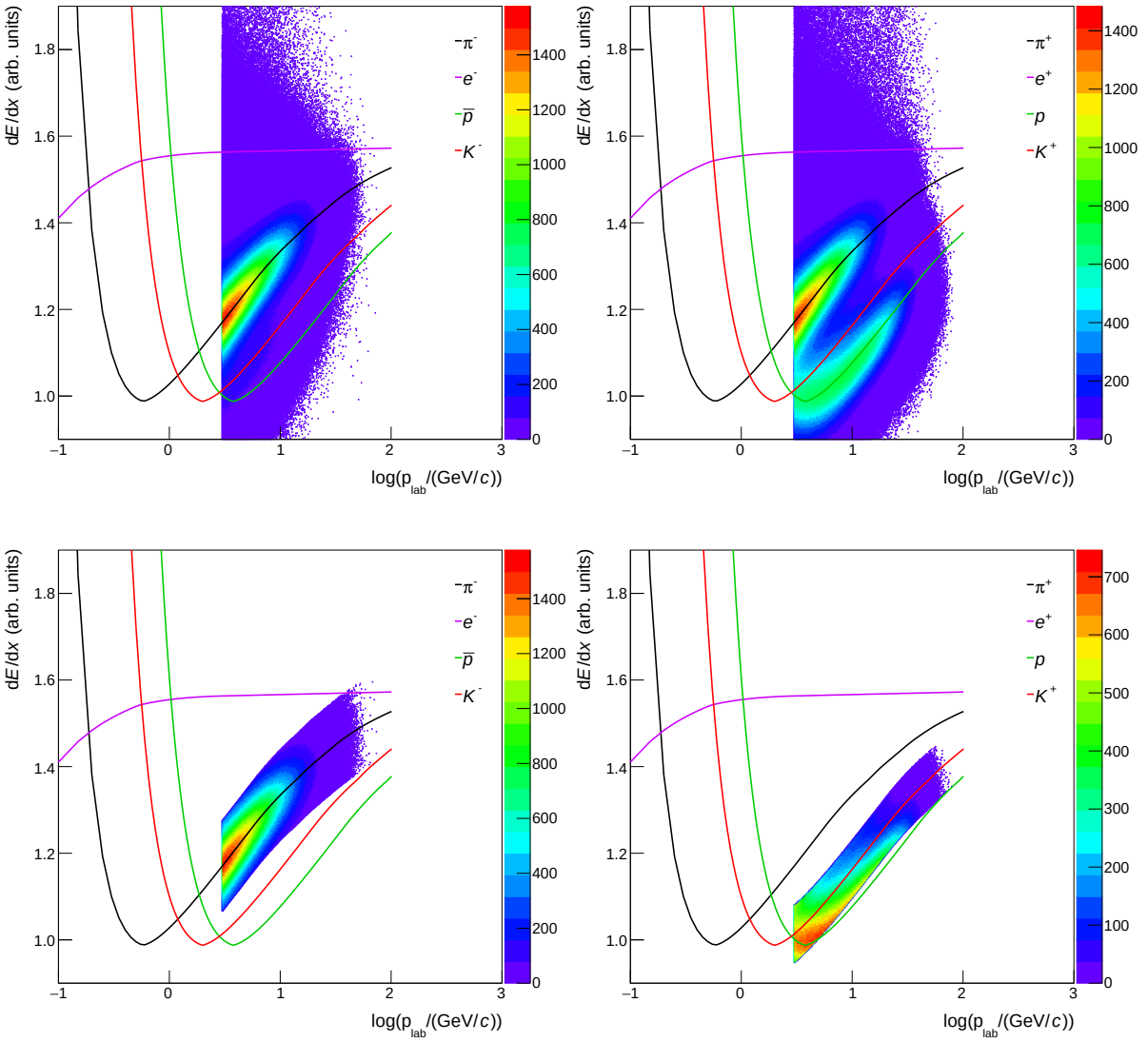

Figure 28: dE/dx distributions as a function of $\log(p_{\mathrm{lab}}/(\mathrm{GeV}/c))$ for positively (right plots) and negatively (left plots) charged particles after event and track selections (without opening angle cut) in Ar+Sc at 40A GeV/c. Colour lines represent Bethe-Bloch curves. The top plots show distributions before the identification cuts. The bottom plots present the distributions after the identification cuts.

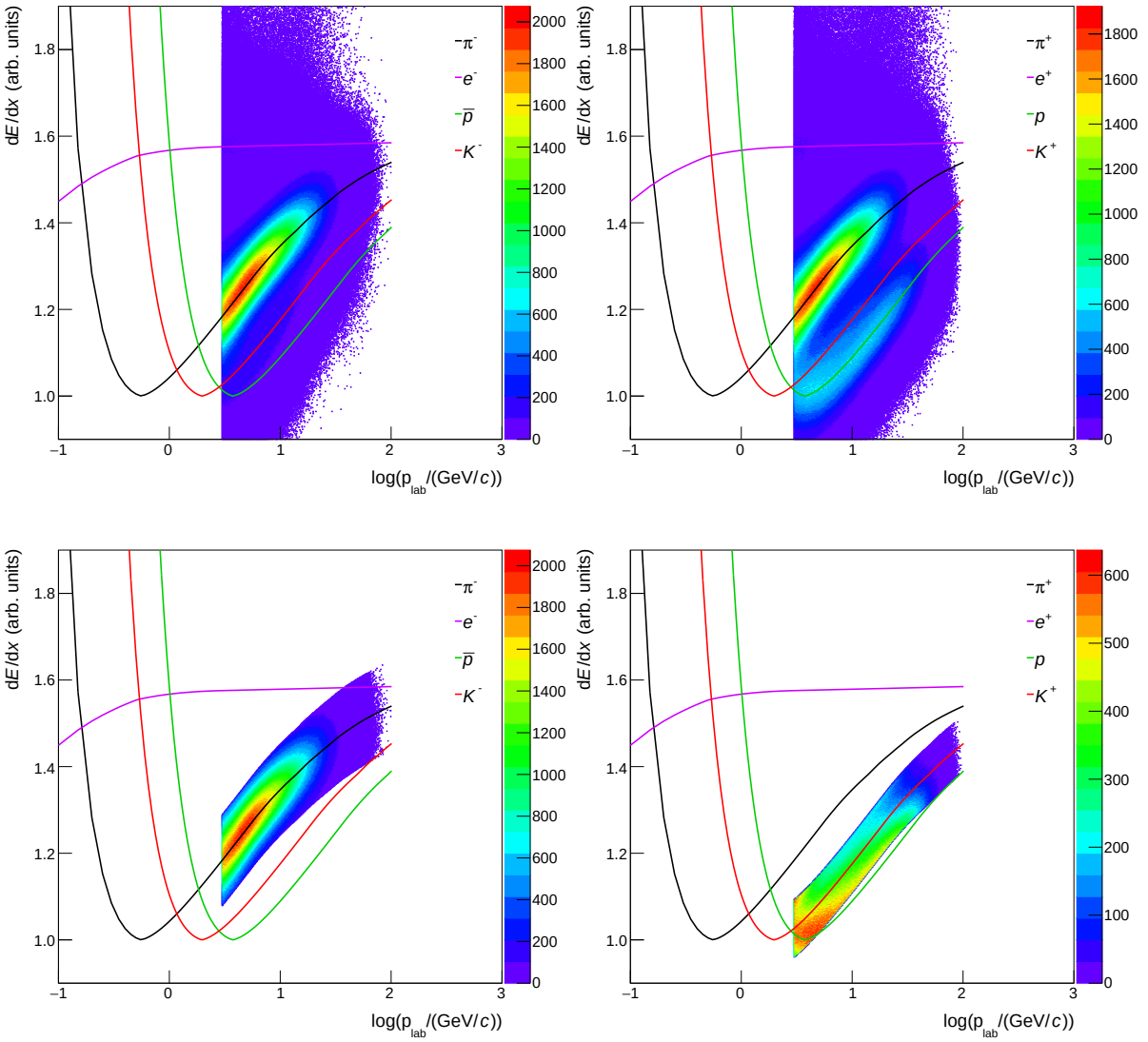

Figure 29: dE/dx distributions as a function of $\log(p_{\mathrm{lab}}/(\mathrm{GeV}/c))$ for positively (right plots) and negatively (left plots) charged particles after event and track selections (without opening angle cut) in Ar+Sc at 75A GeV/c. Colour lines represent Bethe-Bloch curves. The top plots show distributions before the identification cuts. The bottom plots present the distributions after the identification cuts.

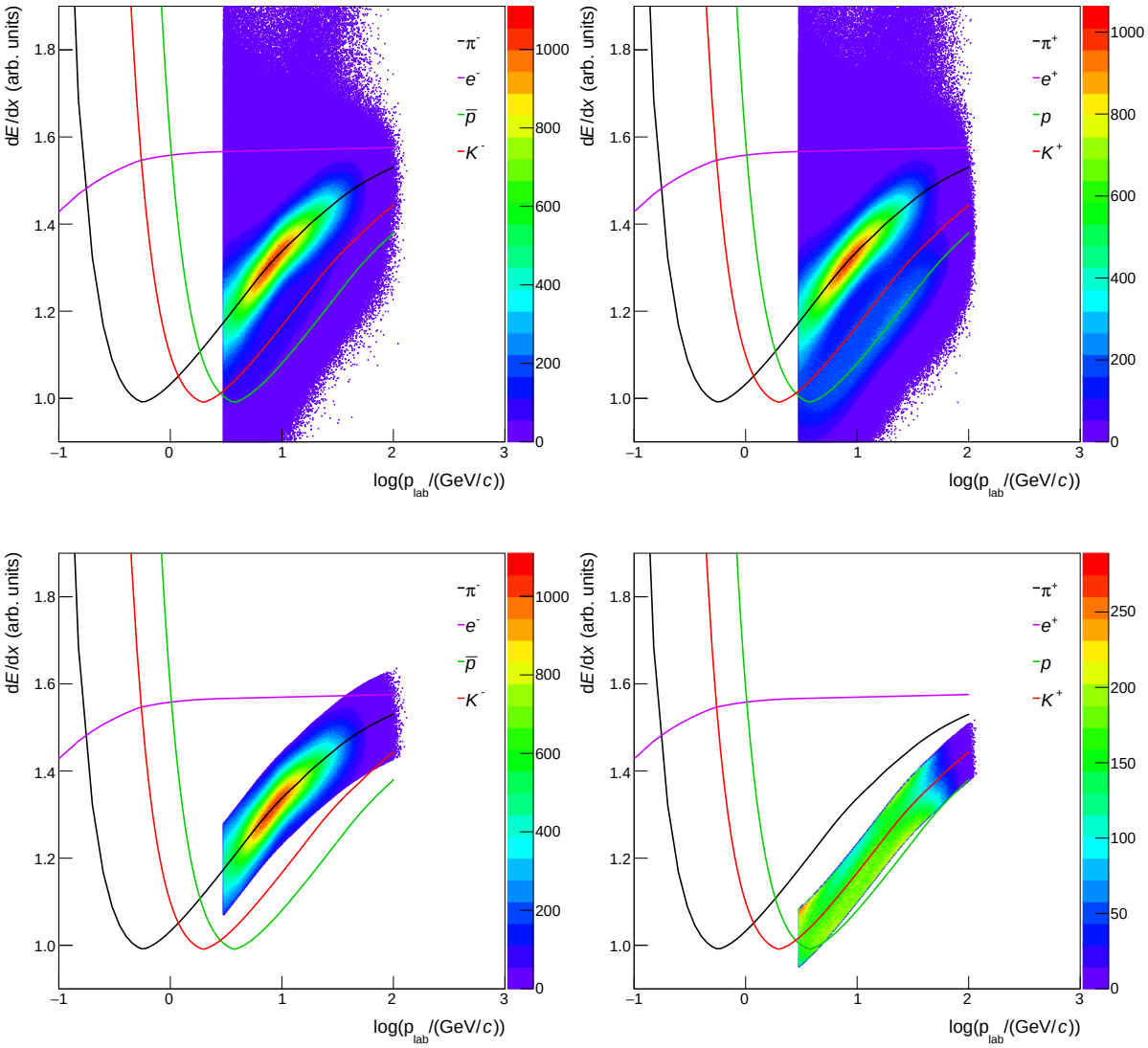

Figure 30: dE/dx distributions as a function of $\log(p_{\mathrm{lab}}/(\mathrm{GeV}/c))$ for positively (right plots) and negatively (left plots) charged particles after event and track selections (without opening angle cut) in Ar+Sc at 150A GeV/c. Colour lines represent Bethe-Bloch curves. The top plots show distributions before the identification cuts. The bottom plots present the distributions after the identification cuts.

6 $K^*(892)^0$ analysis

The $K^*(892)^0$ resonance analysis is a complex process with many stages. The $K^*(892)^0$ is a short-lived, neutral particle that cannot be registered directly by the detectors. The study of the $K^*(892)^0$ meson is only possible through the analysis of its decay products. The $K^*(892)^0$ resonance decays into $K^+\pi^-$ pair with branching ratio $BW = 2/3$ [80]. The primary method for studying resonances is the invariant mass method, which consist in preparing the distributions of invariant masses calculated based on the kinematic characteristics of the decay products. Pairs originating from the particle decay will cluster around the invariant mass value corresponding to the mass of the particle being studied, creating a signal peak in the invariant mass distribution. The centre of this signal corresponds to the mass of the particle, while the width is connected with the average lifetime of the particle. A fitting function is applied to the obtained distribution to separate the resonance signal from the background. The integral of the signal divided by the bin width corresponds to the uncorrected number of $K^*(892)^0$ mesons. The method of signal extraction from the invariant mass distribution is described in Sec. 6.2. Then, the obtained values are corrected for identification efficiency, detector efficiency, and reconstruction algorithm efficiency. The methods of calculating these corrections are presented in Sec. 6.3. Section 6.4 discusses the method of calculating and fitting transverse momentum distributions, while Sec. 6.5 covers the calculation of transverse mass distributions. Section 6.6 describes the method of obtaining rapidity distributions, from which the mean multiplicity of $K^*(892)^0$ resonance is extracted (presented in Sec. 6.7). Finally, Sec. 6.8 presents the method of calculating systematic uncertainties.

6.1 Binning

The analysis of the $K^*(892)^0$ resonance is done in rapidity and transverse momentum bins. Dividing the analysis into bins ensures that the applied corrections for detector and reconstruction inefficiencies are model-independent. The smaller the analysed bins, the more reliable the obtained corrections are. Due to insufficient statistics, the analysis was divided into two parts: one performed in four rapidity bins and a single transverse momentum bin, and the second with four transverse momentum bins and a single rapidity bin. Table 11 shows the division of the phase space into bins of rapidity and transverse momentum for all collision energies analysed in the Ar+Sc collisions. All rapidity values presented in this analysis are calculated in the collision centre-of-mass reference frame.

Rapidity analysis	
Ar+Sc 40A and 150A GeV/c	Ar+Sc 75A GeV/c
$y \in (0.2;0.6), p_T \in (0.0;1.5)$ GeV/c	$y \in (0.2;0.6), p_T \in (0.0;1.5)$ GeV/c
$y \in (0.6;1.0), p_T \in (0.0;1.5)$ GeV/c	$y \in (0.6;1.0), p_T \in (0.0;1.5)$ GeV/c
$y \in (1.0;1.4), p_T \in (0.0;1.5)$ GeV/c	$y \in (1.0;1.4), p_T \in (0.0;1.5)$ GeV/c
$y \in (1.4;1.8), p_T \in (0.0;1.5)$ GeV/c	$y \in (1.4;2.0), p_T \in (0.0;1.5)$ GeV/c

Transverse momentum analysis
Ar+Sc 40A–150A GeV/c
$y \in (0.0;1.5), p_T \in (0.0;0.4)$ GeV/c
$y \in (0.0;1.5), p_T \in (0.4;0.8)$ GeV/c
$y \in (0.0;1.5), p_T \in (0.8;1.2)$ GeV/c
$y \in (0.0;1.5), p_T \in (1.2;1.5)$ GeV/c

Table 11: Division on rapidity and transverse momentum bins.

6.2 Signal extraction

The raw number of $K^*(892)^0$ mesons in a given rapidity and transverse momentum bin is obtained using an invariant mass of its decay products. The mean lifetime of $K^*(892)^0$ resonance is 4.17 fm/c [5], which causes its decay vertex to be basically in the same place as the primary interaction vertex. Because of that, it is impossible to differentiate K^+ and π^- coming from $K^*(892)^0$ resonance decay from K^+ and π^- from the primary vertex. The raw number of $K^*(892)^0$ mesons is obtained by fitting the invariant mass distribution of $K^+\pi^-$ combinations calculated using the formula:

$$m_{K^+\pi^-} = \sqrt{(E_{K^+} + E_{\pi^-})^2 - (\overrightarrow{p_{K^+}} + \overrightarrow{p_{\pi^-}})^2}, \tag{5}$$

where the $K^*(892)^0$ signal is obtained by combining $K^+\pi^-$ pairs originating from the same collision, E_{K^+} and E_{π^-} are total energies of charged kaon and pion, and $\overrightarrow{p_{K^+}}$ and $\overrightarrow{p_{\pi^-}}$ are momentum vectors of kaon and pion.

In this analysis, the invariant mass background is described using the template method [41, 81]. This method was shown to be better at describing $K^*(892)^0$ background than the standard method (based on mixed-event distribution only) [41]. In this method, the invariant mass distribution is described by the formula:

$$f(m_{K^+\pi^-}) = a \cdot T_{\mathrm{res}}^{\mathrm{MC}}(m_{K^+\pi^-}) + b \cdot T_{\mathrm{mix}}^{\mathrm{DATA}}(m_{K^+\pi^-}) + c \cdot BW(m_{K^+\pi^-}), \tag{6}$$

where:

- a, b, c are normalisation parameters ($a+b+c=1$),
- $T_{\text{res}}^{\text{MC}}$ represents background originating from reconstructed Monte Carlo data (Monte Carlo templates); the first contribution comes from a combination of $K^+\pi^-$ pairs where particles come from resonance decays different than $K^*(892)^0$, the second contribution comes from a combination where one track comes from resonance decay and the other from direct production in primary interaction,
- $T_{\text{mix}}^{\text{DATA}}$ represents background obtained from the event mixing method on experimental data (combination of $K^+\pi^-$ tracks which come from different events),
- BW is the Breit-Wigner distribution describing the $K^*(892)^0$ signal:

$$BW(m_{K^+\pi^-}) = A \cdot \frac{\frac{1}{4}\cdot\Gamma_{K^*}^2}{(m_{K^+\pi^-} - m_{K^*})^2 + \frac{1}{4}\Gamma_{K^*}^2}, \tag{7}$$

where:

- A is the normalisation factor,
- $\Gamma_{K^*} = 0.0473$ GeV is $K^*(892)^0$ resonance width taken from PDG [5],
- $m_{K^*} = 0.89555$ GeV is $K^*(892)^0$ resonance rest mass taken from PDG [5].

Before the fit, $T_{\text{res}}^{\text{MC}}$ and $T_{\text{mix}}^{\text{DATA}}$ histograms were scaled to the same number of entries as experimental data invariant mass distribution in the range from 0.66 GeV to 1.26 GeV. Figure 31 presents an example of fitting Eq. (6) to selected invariant mass distribution. Parameters of mass m_{K^*} and width Γ_{K^*} were decided to be fixed to PDG values, because of instability of obtained m_{K^*} and Γ_{K^*} between rapidity and transverse momentum bins. In this analysis, invariant mass fitting range was set on $m_{K^+\pi^-} > 0.66$ GeV and $m_{K^+\pi^-} < 1.26$ GeV.

The next step of the template method is subtracting the fitted background using formula applied to each $m_{K^+\pi^-}$ bin:

$$N_{\text{bin}}(m_{K^+\pi^-}) = N_{\text{raw}}(m_{K^+\pi^-}) - a \cdot T_{\text{res}}^{\text{MC}}(m_{K^+\pi^-}) - b \cdot T_{\text{mix}}^{\text{DATA}}(m_{K^+\pi^-}), \tag{8}$$

where:

- $N_{\text{raw}}(m_{K^+\pi^-})$ is the number of entries in a given invariant mass bin, which comes from $K^+\pi^-$ combinations from experimental data,
- $T_{\text{res}}^{\text{MC}}$ and $T_{\text{mix}}^{\text{DATA}}$ represent background described by Eq. (6).

The statistical uncertainty of the bin content is calculated as:

$$\Delta N_{\text{bin}} = \sqrt{(\Delta N_{\text{raw}})^2 + a^2(\Delta T_{\text{res}}^{\text{MC}})^2 + b^2(\Delta T_{\text{mix}}^{\text{DATA}})^2}, \tag{9}$$

where ΔN_{raw}, $\Delta T_{\text{res}}^{\text{MC}}$ and $\Delta T_{\text{mix}}^{\text{DATA}}$ (the notation $(m_{K^+\pi^-})$ is omitted for clarity) are the standard

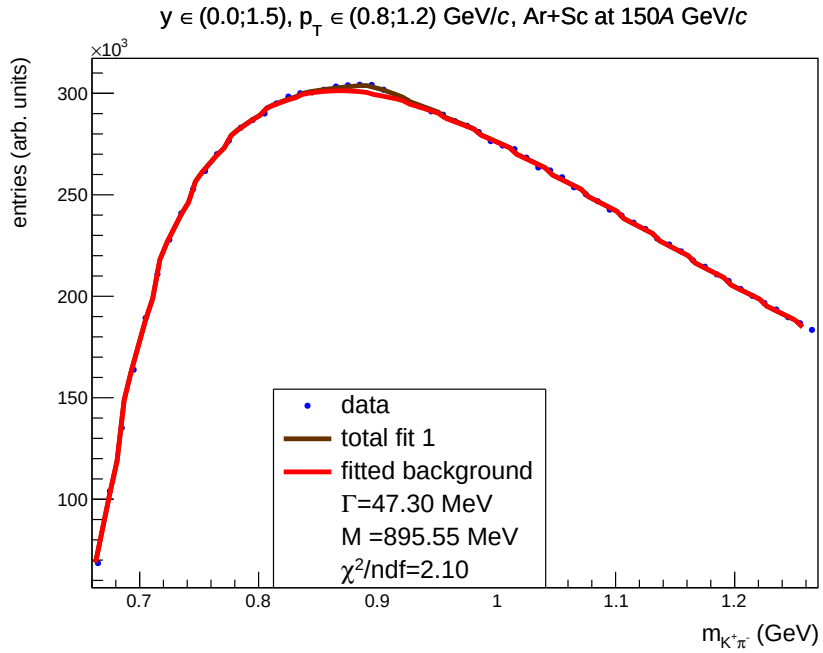

Figure 31: Example of invariant mass distribution of $K^+\pi^-$ combinations from the same event (blue points), from Ar+Sc collisions at 150A GeV/c in rapidity bin $y \in (0.0;1.5)$ and transverse momentum bin $p_T \in (0.8;1.2)$ GeV/c. The brown line (total fit) shows the fitted function described by Eq. (6). The red line (fitted background) shows the background described by $T_{\text{res}}^{\text{MC}}$ and $T_{\text{mix}}^{\text{DATA}}$ contributions to the total fit.

uncertainties, taken as the square root of the number of entries in a given invariant mass bin. In the $T_{\text{res}}^{\text{MC}}$ and $T_{\text{mix}}^{\text{DATA}}$ histograms, the number of entries was normalised to the experimental $m_{K^+\pi^-}$ distribution.

The N_{bin} uncertainty includes statistical uncertainties of data distribution, resonance Monte Carlo template and background obtained from the event mixing method. Due to high statistics of Monte Carlo and mixed events, the uncertainties of parameters a and b were neglected. The example of the obtained invariant mass distribution after background subtraction is presented as blue points in Fig. 32.

The obtained invariant mass distribution (blue points in Fig. 32) in a given kinematic bin is fitted by Eq. (10) to describe the residual background and obtain the final signal of $K^*(892)^0$ meson:

$$f(m_{K^+\pi^-}) = d \cdot (m_{K^+\pi^-})^2 + e \cdot (m_{K^+\pi^-}) + f + g \cdot BW(m_{K^+\pi^-}), \tag{10}$$

where the background is described by a second-order polynomial curve, the resonance signal is described by Breit-Wigner distribution (BW) with fixed parameters of mass and width, and

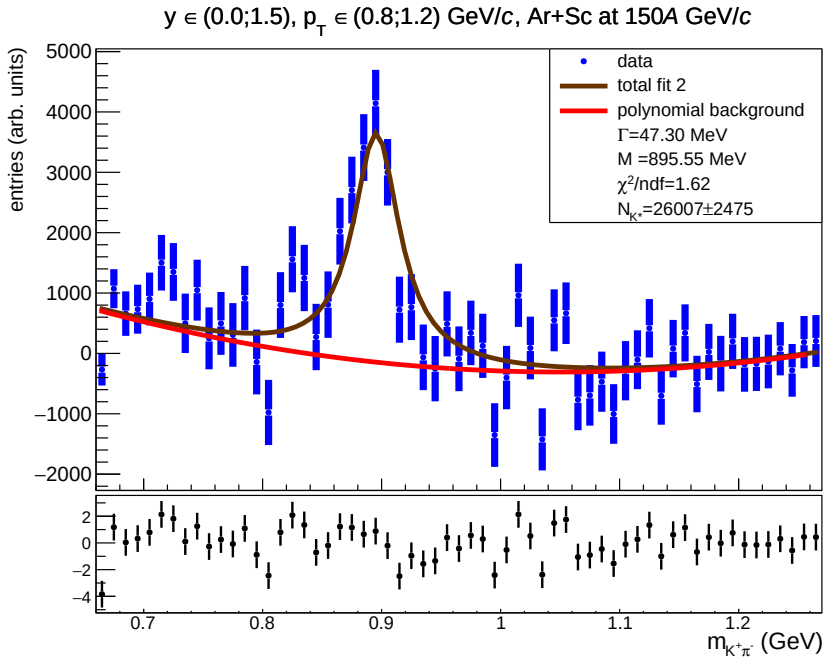

Figure 32: Example of invariant mass distribution of $K^+\pi^-$ after background subtraction (blue points), from Ar+Sc collisions at 150A GeV/c in rapidity bin $y \in (0.0; 1.5)$ and transverse momentum bin $p_T \in (0.8; 1.2)$ GeV/c. The brown line (total fit 2) shows the fitted function described by Eq. (10). The red line (polynomial background) shows the residual background described by a second-order polynomial curve. The bottom panel presents the differences between the total fit 2 and invariant mass distribution (N_{bin} points) divided by the uncertainties (ΔN_{bin} calculated using Eq. (9)).

d, e, f, g are free parameters of the fit.

The raw number of $K^*(892)^0$ mesons, $N_{K^*}(y, p_T)$, was obtained by integrating fitted Breit-Wigner part of Eq. (10) and dividing it by a bin width. The range of performed integral was set to $\pm 4\Gamma_{K^*}$ around m_{K^*} value taken from PDG. The uncertainty of the raw number of $K^*(892)^0$ mesons was estimated using the TF1::IntegralError function from the ROOT library [82], which calculates uncertainty using covariance matrix of fitted parameters. Tables 12 and 13 show the obtained uncorrected (raw) numbers of $K^*(892)^0$ mesons in Ar+Sc collisions at all analysed beam momenta.

6.3 Corrections

Obtained from the template method, the raw number of $K^*(892)^0$ mesons needs to be corrected for inefficiencies in the reconstruction algorithm, loss of data due to geometrical acceptance of the detector, signal extraction method, and identification method.

In order to estimate the correction for loss of particles due to identification method the

$N_{K^*}(y, p_T)$		
y and p_T bins	Ar+Sc at 40A GeV/c	Ar+Sc at 150A GeV/c
$y \in (0.2;0.6), p_T \in (0.0;1.5)$ GeV/c	11723 ± 2228	23338 ± 3006
$y \in (0.6;1.0), p_T \in (0.0;1.5)$ GeV/c	20713 ± 2549	28596 ± 3166
$y \in (1.0;1.4), p_T \in (0.0;1.5)$ GeV/c	16584 ± 2065	32008 ± 3089
$y \in (1.4;1.8), p_T \in (0.0;1.5)$ GeV/c	5449 ± 1414	16472 ± 2544
y and p_T bins	Ar+Sc at 75A GeV/c	
$y \in (0.2;0.6), p_T \in (0.0;1.5)$ GeV/c	31914 ± 3511	
$y \in (0.6;1.0), p_T \in (0.0;1.5)$ GeV/c	35131 ± 3445	
$y \in (1.0;1.4), p_T \in (0.0;1.5)$ GeV/c	21710 ± 3103	
$y \in (1.4;2.0), p_T \in (0.0;1.5)$ GeV/c	16056 ± 2607	

Table 12: Numerical results of uncorrected number of $K^*(892)^0$ resonances in rapidity analysis.

$N_{K^*}(y, p_T)$			
y and p_T bins	Ar+Sc at 40A GeV/c	Ar+Sc at 75A GeV/c	Ar+Sc at 150A GeV/c
$y \in (0.0;1.5)$, $p_T \in (0.0;0.4)$ GeV/c	12210 ± 2123	28991 ± 3718	24642 ± 3430
$y \in (0.0;1.5)$, $p_T \in (0.4;0.8)$ GeV/c	17116 ± 2667	56314 ± 4074	40873 ± 3892
$y \in (0.0;1.5)$, $p_T \in (0.8;1.2)$ GeV/c	18059 ± 2043	20176 ± 2640	26007 ± 2475
$y \in (0.0;1.5)$, $p_T \in (1.2;1.5)$ GeV/c	4282 ± 1209	7247 ± 1372	6218 ± 1181

Table 13: Numerical results of uncorrected number of $K^*(892)^0$ resonances in transverse momentum analysis.

following equation was used:

$$c\,\mathrm{d}E/\mathrm{d}x = \frac{1}{\varepsilon_{K^+} \cdot \varepsilon_{\pi^-}} \simeq 1.209, \tag{11}$$

where $\varepsilon_{K^+} = 0.866$ and $\varepsilon_{\pi^-} = 0.955$ are probabilities of finding K^+ or π^- in $1.5\sigma_{K^+}$ or $2\sigma_{\pi^-}$ around nominal Bethe-Bloch curve (based on the cumulative Gaussian distribution).

In order to estimate corrections for the loss of particles due to inefficiencies in the event and track reconstruction algorithm, geometrical acceptance of the detector, the method used to extract a raw number of $K^*(892)^0$ mesons, and quality of cuts on events and tracks, Monte Carlo simulated data were used. The EPOS1.99 model was used to generate approximately $20 \cdot 10^6$ inelastic ^{40}Ar + ^{45}Sc collisions at 40A, 75A, and 150A GeV/c beam momenta. Then, the generated data were processed by dedicated detector response simulation and reconstructed, obtaining data similar to real experimental data, what allowed for estimation of detector and

reconstruction algorithm influence on measured data. The reconstructed Monte Carlo data were subjected to the same event and track selection (if it was possible – see Chapter 4), allowing for estimation of their influence on data. Comparison of $K^*(892)^0$ numbers taken from reconstructed Monte Carlo data with those in generated data (pure Monte Carlo) allows for an estimation of the loss of particles due to inefficiencies in the reconstruction algorithm, loss of data due to geometrical acceptance of the detector, signal extraction method, and event and track cuts. Correction calculated by comparing normalised ratios of the number of generated $K^*(892)^0$ mesons to the number of selected ones from reconstructed Monte Carlo can be expressed as:

$$c_{\mathrm{MC}}(y,p_{\mathrm{T}}) = \frac{n_{\mathrm{gen}}(y,p_{\mathrm{T}})}{n_{\mathrm{sel}}(y,p_{\mathrm{T}})} \equiv \frac{N^{\mathrm{gen}}_{K^*}(y,p_{\mathrm{T}})}{N^{\mathrm{gen}}_{\mathrm{events}}} \Big/ \frac{N^{\mathrm{sel}}_{K^*}(y,p_{\mathrm{T}})}{N^{\mathrm{sel}}_{\mathrm{events}}} = \left(\frac{N^{\mathrm{sel}}_{K^*}(y,p_{\mathrm{T}})}{N^{\mathrm{gen}}_{K^*}(y,p_{\mathrm{T}})}\right)^{-1} \cdot \frac{N^{\mathrm{sel}}_{\mathrm{events}}}{N^{\mathrm{gen}}_{\mathrm{events}}}, \tag{12}$$

where:

- $N^{\mathrm{gen}}_{K^*}(y,p_{\mathrm{T}})$ represents the number of $K^*(892)^0$ mesons which decay into $K^+\pi^-$, obtained from pure Monte Carlo in a given (y,p_{T}) bin,
- $N^{\mathrm{sel}}_{K^*}(y,p_{\mathrm{T}})$ represents the number of $K^*(892)^0$ mesons which decay into $K^+\pi^-$, obtained from reconstructed Monte Carlo in a given (y,p_{T}) bin; the number of K^{*0}s was obtained by repeating the same analysis procedures as for experimental data (the only exception was the identification method, which was replaced by a matching procedure – see Sec. 3.2),
- $N^{\mathrm{gen}}_{\mathrm{events}}$ represents the number of generated events,
- $N^{\mathrm{sel}}_{\mathrm{events}}$ represents the number of reconstructed and accepted events.

The statistical uncertainty of Monte Carlo correction is estimated using the equation [81]:

$$\Delta c_{\mathrm{MC}}(y,p_{\mathrm{T}}) = c_{\mathrm{MC}}(y,p_{\mathrm{T}}) \sqrt{\frac{N^{\mathrm{gen}}_{K^*}(y,p_{\mathrm{T}}) - N^{\mathrm{sel}}_{K^*}(y,p_{\mathrm{T}})}{N^{\mathrm{gen}}_{K^*}(y,p_{\mathrm{T}}) \cdot N^{\mathrm{sel}}_{K^*}(y,p_{\mathrm{T}})}}. \tag{13}$$

The values of MC corrections for loss of particles due to inefficiencies in event and track reconstruction algorithm, event and track cuts, geometrical acceptance of the detector, and signal extraction method with uncertainties for all measured beam momenta are presented in Tables 14 and 15.

$c_{\mathrm{MC}}(y, p_{\mathrm{T}})$		
y and p_{T} bins	Ar+Sc at 40A GeV/c	Ar+Sc at 150A GeV/c
$y \in (0.2;0.6), p_{\mathrm{T}} \in (0.0;1.5)$ GeV/c	14.444 ± 0.076	2.725 ± 0.005
$y \in (0.6;1.0), p_{\mathrm{T}} \in (0.0;1.5)$ GeV/c	6.241 ± 0.023	1.979 ± 0.003
$y \in (1.0;1.4), p_{\mathrm{T}} \in (0.0;1.5)$ GeV/c	5.157 ± 0.024	1.777 ± 0.002
$y \in (1.4;1.8), p_{\mathrm{T}} \in (0.0;1.5)$ GeV/c	5.831 ± 0.047	2.200 ± 0.004
y and p_{T} bins	Ar+Sc at 75A GeV/c	
$y \in (0.2;0.6), p_{\mathrm{T}} \in (0.0;1.5)$ GeV/c	5.592 ± 0.017	
$y \in (0.6;1.0), p_{\mathrm{T}} \in (0.0;1.5)$ GeV/c	3.437 ± 0.008	
$y \in (1.0;1.4), p_{\mathrm{T}} \in (0.0;1.5)$ GeV/c	2.732 ± 0.006	
$y \in (1.4;2.0), p_{\mathrm{T}} \in (0.0;1.5)$ GeV/c	3.868 ± 0.014	

Table 14: Numerical results of Monte Carlo corrections in rapidity analysis.

$c_{\mathrm{MC}}(y, p_{\mathrm{T}})$			
y and p_{T} bins	Ar+Sc at 40A GeV/c	Ar+Sc at 75A GeV/c	Ar+Sc at 150A GeV/c
$y \in (0.0;1.5)$, $p_{\mathrm{T}} \in (0.0;0.4)$ GeV	11.396 ± 0.044	3.598 ± 0.007	2.162 ± 0.003
$y \in (0.0;1.5)$, $p_{\mathrm{T}} \in (0.4;0.8)$ GeV	8.902 ± 0.035	4.703 ± 0.011	2.220 ± 0.003
$y \in (0.0;1.5)$, $p_{\mathrm{T}} \in (0.8;1.2)$ GeV	8.384 ± 0.061	5.688 ± 0.027	2.622 ± 0.007
$y \in (0.0;1.5)$, $p_{\mathrm{T}} \in (1.2;1.5)$ GeV	4.736 ± 0.055	5.371 ± 0.051	3.198 ± 0.019

Table 15: Numerical results of Monte Carlo corrections in transverse momentum analysis.

6.4 Transverse momentum spectra

The double-differential yield of $K^*(892)^0$ resonances per event in rapidity and transverse momentum bin was calculated using equation:

$$\frac{\mathrm{d}^2 n}{\mathrm{d}y\,\mathrm{d}p_\mathrm{T}}(y,p_\mathrm{T}) = \frac{1}{BR}\cdot\frac{N_{K^*}(y,p_\mathrm{T})}{N_\mathrm{events}}\cdot\frac{c_{\mathrm{d}E/\mathrm{d}x}\cdot c_\mathrm{MC}(y,p_\mathrm{T})}{\Delta y\,\Delta p_\mathrm{T}}, \tag{14}$$

where:

- $BR = 2/3$ represents the branching ratio of $K^*(892)^0$ resonance decay into pair of $K^+\pi^-$ [80],
- $N_{K^*}(y,p_\mathrm{T})$ represents the raw number of $K^*(892)^0$ mesons obtained from the template method, from experimental data,
- N_events represents the number of accepted events from experimental data,
- $c_{\mathrm{d}E/\mathrm{d}x}$ represents correction factor for particle identification,
- $c_\mathrm{MC}(y,p_\mathrm{T})$ represents Monte Carlo correction factor for loss of particles due to inefficiencies in event and track reconstruction algorithm, event and track cuts, geometrical acceptance of the detector, and signal extraction method,
- $\Delta y = 1.5$ represents the width of the rapidity bin,
- Δp_T represents the width of the transverse momentum bin.

The corrected $K^*(892)^0$ yields were estimated in one rapidity bin $y \in (0.0;1.5)$ only, because of insufficient statistics (see Sec. 6.1).

The statistical uncertainties of corrected $K^*(892)^0$ yields were estimated using equation:

$$\Delta\frac{\mathrm{d}^2 n}{\mathrm{d}y\,\mathrm{d}p_\mathrm{T}}(y,p_\mathrm{T}) = \frac{1}{BR}\cdot\sqrt{\left(\frac{c_{\mathrm{d}E/\mathrm{d}x}\cdot c_\mathrm{MC}(y,p_\mathrm{T})}{N_\mathrm{events}\,\Delta y\,\Delta p_\mathrm{T}}\right)^2(\Delta N_{K^*}(y,p_\mathrm{T}))^2 + \left(\frac{N_{K^*}(y,p_\mathrm{T})\cdot c_{\mathrm{d}E/\mathrm{d}x}}{N_\mathrm{events}\,\Delta y\,\Delta p_\mathrm{T}}\right)^2(\Delta c_\mathrm{MC}(y,p_\mathrm{T}))^2}. \tag{15}$$

The obtained transverse momentum spectra (see example result in Fig. 33) were fitted with the function described by formula:

$$f(p_\mathrm{T}) = A\cdot p_\mathrm{T}\exp\left(-\frac{\sqrt{p_\mathrm{T}^2+m_0^2}}{T}\right), \tag{16}$$

where:

- A is normalisation factor,
- $m_0 \equiv m_{K^*}$ is $K^*(892)^0$ mass taken from PDG [5],
- T represents the inverse slope parameter.

The result of the following fit for $K^*(892)^0$ yields in Ar+Sc collisions at beam momentum

150A GeV/c is presented in Fig. 33.

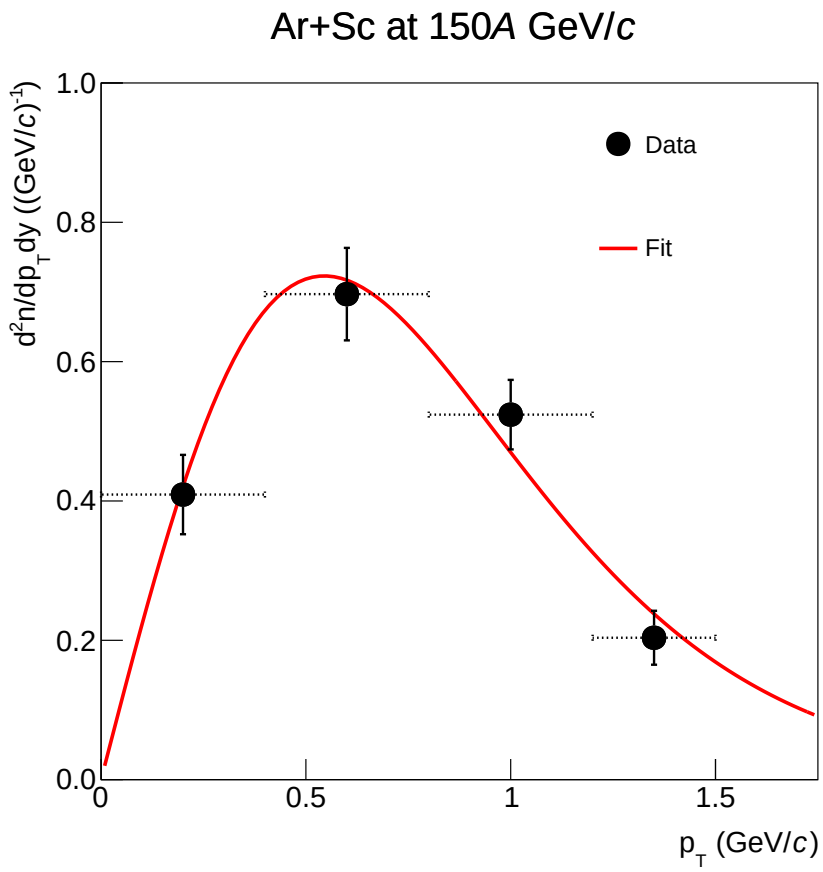

Figure 33: Example of transverse momentum distribution of $K^*(892)^0$ resonances from Ar+Sc collisions at beam momentum 150A GeV/c in rapidity bin $y \in (0.0;1.5)$. The red line shows the function described by Eq. (16), fitted in the range $p_T \in (0.0;1.5)$ GeV/c. Horizontal bars represent transverse momentum bin widths (not included in the fitting procedure).

6.5 Transverse mass spectra

The transverse mass spectra of $K^*(892)^0$ resonances $\frac{1}{m_T}\frac{d^2n}{dm_T dy}$ were calculated by transforming transverse momentum spectra using definition $m_T \equiv \sqrt{p_T^2 + m_0^2}$, and relation:

$$\frac{1}{m_T}\frac{d^2n}{dm_T dy} = \frac{1}{p_T}\frac{d^2n}{dy dp_T}, \tag{17}$$

where statistical uncertainties were propagated from transverse momentum spectra.

The result of the transformation of transverse momentum spectrum to transverse mass distribution of $K^*(892)^0$ resonances in Ar+Sc collisions at beam momentum 150A GeV/c is

presented in Fig. 34.

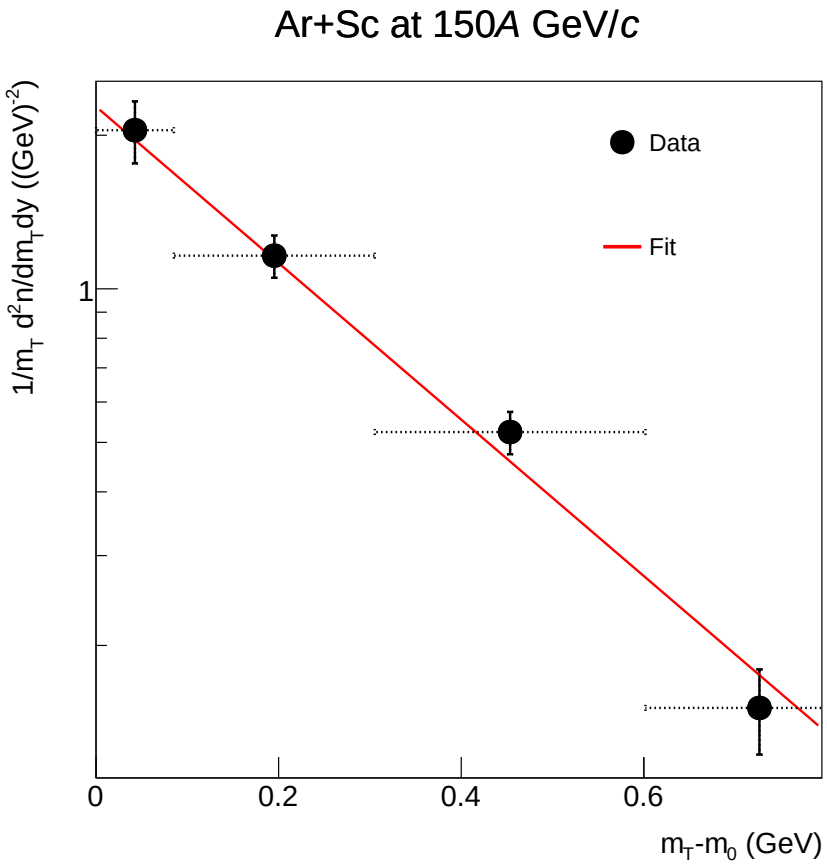

Figure 34: Example of transverse mass distribution of $K^*(892)^0$ resonances from Ar+Sc collisions at beam momentum 150*A* GeV/*c* in rapidity bin $y \in (0.0; 1.5)$. The red line shows the function described by Eq. (16) fitted to transverse momentum distribution and then transformed according to Eq. (17).

6.6 Rapidity spectra

The rapidity spectra of $K^*(892)^0$ resonances were calculated using uncorrected numbers of $K^*(892)^0$ mesons in one transverse momentum bin, $p_T \in (0.0; 1.5)$ GeV/*c*, because of insufficient statistics (see Sec. 6.1). The $K^*(892)^0$ yields were obtained using the formula:

$$\frac{dn}{dy}(y) = \frac{d^2n}{dy\,dp_T}(y, p_T) \cdot \Delta p_T, \tag{18}$$

where $\Delta p_T = 1.5$ GeV/*c* represents the width of the transverse momentum bin.

The statistical uncertainties of the values of rapidity distributions were estimated using the formula:

$$\Delta\frac{\mathrm{d}n}{\mathrm{d}y}(y) = \Delta\frac{\mathrm{d}^2n}{\mathrm{d}y\,\mathrm{d}p_\mathrm{T}}(y, p_\mathrm{T}) \cdot \Delta p_\mathrm{T}. \tag{19}$$

The example of the obtained rapidity distribution for Ar+Sc collisions at beam momentum 150A GeV/c is presented in Fig. 35.

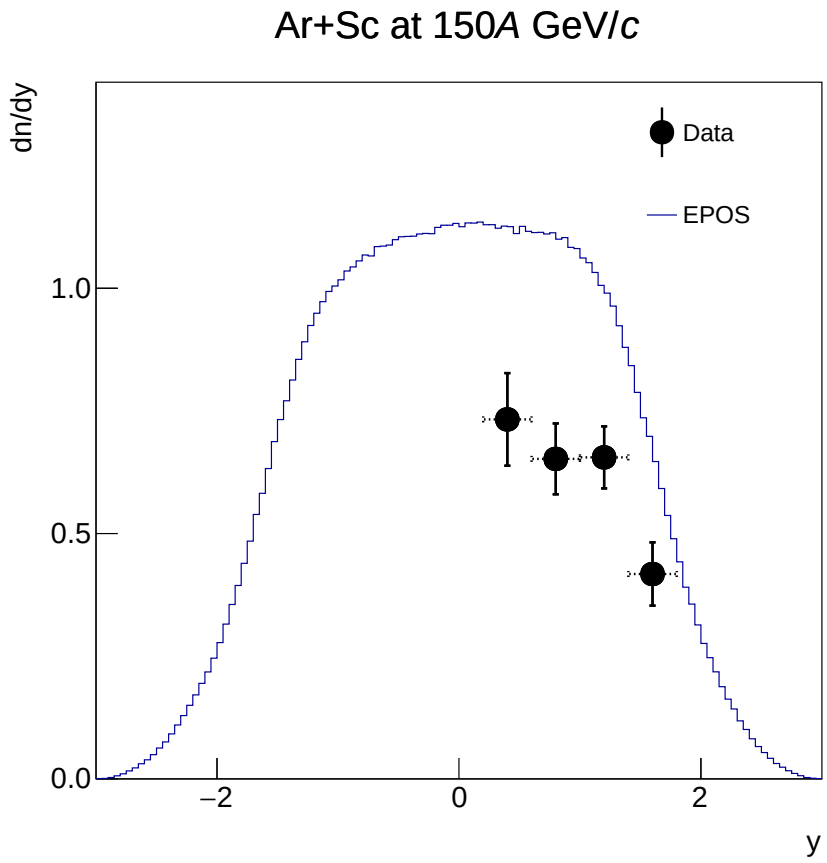

Figure 35: Example of rapidity distribution of $K^*(892)^0$ resonances from Ar+Sc collisions at beam momentum 150A GeV/c in transverse momentum bin $p_\mathrm{T} \in (0.0; 1.5)$ GeV/c. The black points represent measured data, and the blue line shows EPOS1.99 prediction. Horizontal bars represent rapidity bin width.

6.7 Mean multiplicities

The mean multiplicity of $K^*(892)^0$ resonances was obtained using results from rapidity distribution corrected by the EPOS model using following equations [83]:

$$\langle K^*(892)^0 \rangle = \frac{1}{B} \cdot \sum_i \left(\frac{\mathrm{d}n}{\mathrm{d}y}\Delta y\right)_i, \tag{20}$$

$$B = \frac{\int_{y_{\min}}^{y_{\max}} \frac{\mathrm{d}n}{\mathrm{d}y}_{\mathrm{EPOS}} \mathrm{d}y}{\int_{-\infty}^{\infty} \frac{\mathrm{d}n}{\mathrm{d}y}_{\mathrm{EPOS}} \mathrm{d}y}, \tag{21}$$

what means that multiplicity was calculated as scaled by a factor $\frac{1}{B}$ sum of points from the rapidity spectrum multiplied by rapidity bin width Δy. Factor B was estimated from Monte Carlo rapidity spectrum as a contribution of rapidity distribution in the measured region to the full rapidity distribution. Rapidity spectra used in this estimation were taken from the 10% most central Ar+Sc collisions generated by the EPOS1.99 model in the same transverse momentum range as measured data ($p_{\mathrm{T}} \in (0.0; 1.5)$ GeV/c). The $y_{\min} = 0.2$ represents the lower limit of the first measured rapidity bin. The $y_{\max} = 1.8$ (for Ar+Sc at 40A and 150A GeV/c) or $y_{\max} = 2.0$ (for Ar+Sc at 75A GeV/c) represents the upper limit of the last measured rapidity bin.

The statistical uncertainty of the mean multiplicity of $K^*(892)^0$ mesons was calculated using equation:

$$\Delta\langle K^*(892)^0\rangle = \frac{1}{B} \cdot \sqrt{\sum_i \left((\Delta y)^2 \cdot \left(\Delta \frac{\mathrm{d}n}{\mathrm{d}y} \right)^2 \right)_i}. \tag{22}$$

6.8 Systematic uncertainties

The systematic uncertainties were estimated for all analysed Ar+Sc data sets. Uncertainties were calculated for rapidity and transverse momentum and mass distributions, mean $K^*(892)^0$ multiplicities, and inverse slope parameters of transverse momentum spectra. The potential impact of biases on the results was assessed by comparing results from different selection criteria with nominal results. Systematic uncertainties are divided into two groups, connected with event and track selections, particle identification and matching, and related to parameters and data used in signal extraction, corrections, and multiplicity calculation.

Systematic uncertainty contributions connected with event and track selections, particle identification and matching:

1. event cut on the z position of the main vertex was modified from [-582;-578] cm to [-581;-579] cm and [-585;-575] cm,
2. event cut on beam off-time particles (WFA) was changed from ±4 μs to ±5 μs and ±3.5 μs,
3. total number of points required to be registered in all TPCs was changed from ≥ 30 to ≥ 15 and ≥ 35,

4. total number of points required to be registered in VPTCs was changed from ≥ 15 to ≥ 10 and ≥ 18,

5. impact parameter range where particles are accepted was changed from $|b_x| \leq 4$ cm, $|b_y| \leq 2$ cm to no cut on impact parameter and $|b_x| \leq 2$ cm, $|b_y| \leq 1$ cm,

6. particle identification cut was modified from $1.5\sigma_{K^+}$, $2.0\sigma_{\pi^-}$ to $1.0\sigma_{K^+}$, $1.5\sigma_{\pi^-}$ and $2.0\sigma_{K^+}$, $2.5\sigma_{\pi^-}$,

7. during the matching procedure, the minimum ratio of common points between the generated and reconstructed track to the number of clusters in the reconstructed track was changed from 50% to 60% and 40%.

Systematic uncertainty contributions connected with parameters and data used in signal extraction, corrections, and multiplicity calculation:

1. the invariant mass range used to obtain the raw number of $K^*(892)^0$ resonances was changed from $\pm 4.0\Gamma_{K^*}$ to $\pm 3.5\Gamma_{K^*}$ and $\pm 4.5\Gamma_{K^*}$,

2. during fitting invariant mass distribution, the m_{K^*} parameter was modified from being fixed to PDG value to being a free parameter,

3. during the analysis of invariant mass distribution, the lower limit of the fitting and scaling range was changed from 0.66 GeV to 0.69 GeV,

4. during analysis, the model used to generate Monte Carlo data was changed from EPOS1.99 to FTFP-BERT [78]; the change includes the Monte Carlo templates used for invariant mass background description, the distributions used for correction calculations, and the scaling factor B (see Eq. (21)) used in the mean multiplicity determination.

The total systematic uncertainty was calculated using equation:

$$\Delta_{\text{sys}} = \sqrt{\sum_i \Delta^2_{\text{sys},i}}, \tag{23}$$

where $\Delta_{\text{sys},i}$ is the value of partial systematic uncertainty from one source, calculated as half of the difference between the minimum and maximum value resulting from the variation of a given cut or analysis procedure (e.g. $\Delta_{\text{sys},i}$ calculations for source varying TPC points cut will take into account results from analysis with cut ≥ 15, ≥ 35, and ≥ 30).

The contributions to systematic uncertainty of the mean multiplicity of $K^*(892)^0$ and the inverse slope parameter are presented in Figs. 36 and 37 for Ar+Sc at 40*A* GeV/*c*, Figs. 38 and 39 for Ar+Sc at 75*A* GeV/*c*, and Figs. 40 and 41 for Ar+Sc at 150*A* GeV/*c*.

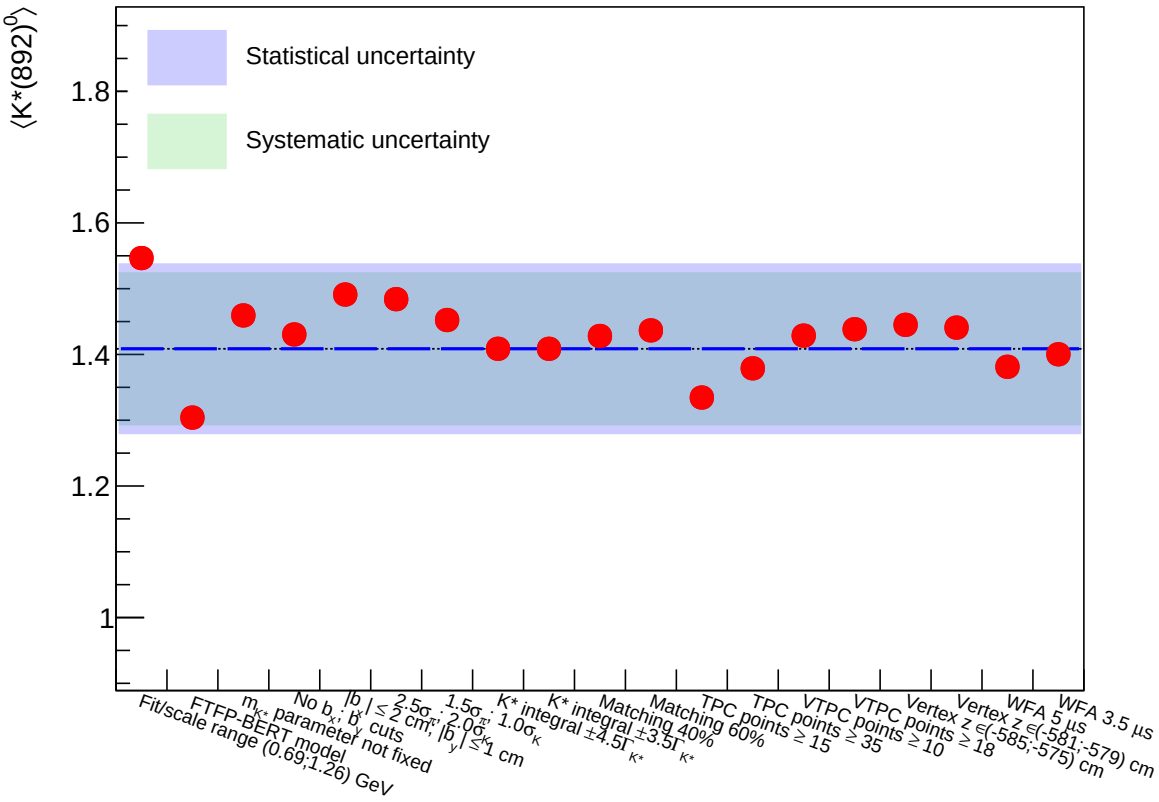

Figure 36: Contributions of all sources to systematic uncertainty of the mean multiplicity of $K^*(892)^0$ in Ar+Sc collisions at beam momentum 40*A* GeV/*c*. Blue dashed line represents nominal value (with standard list of cuts).

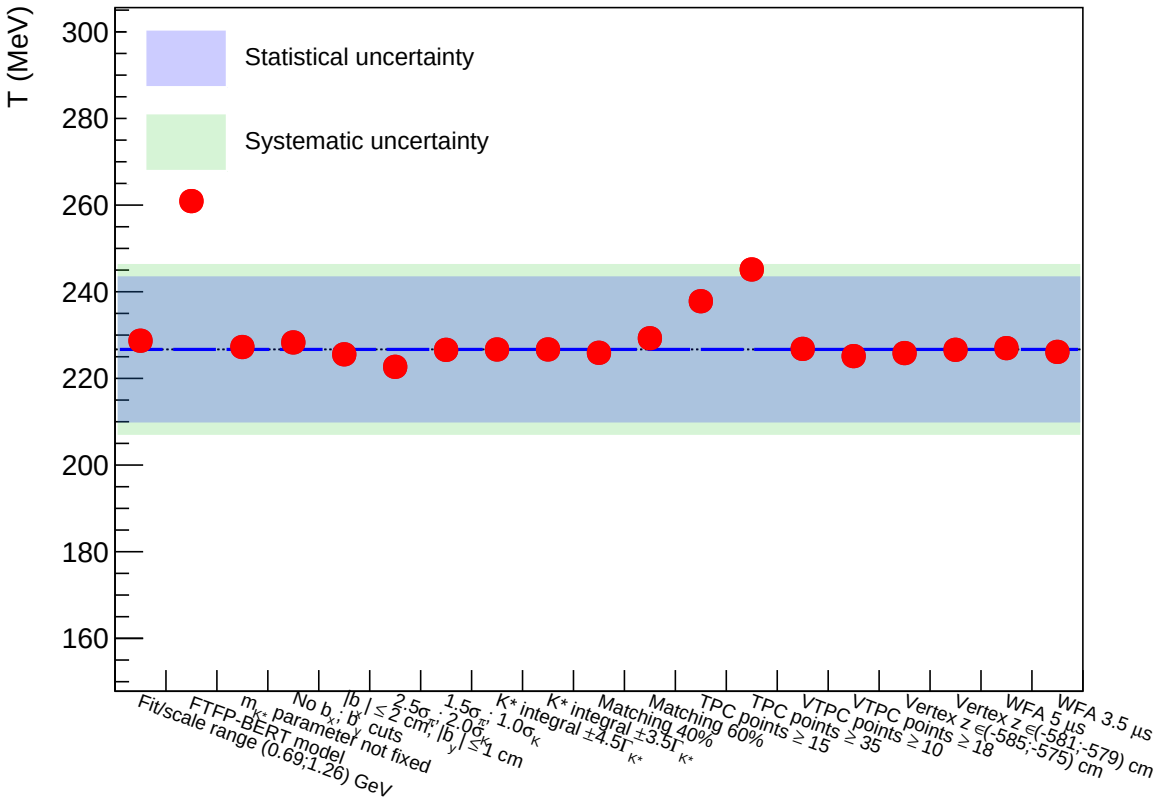

Figure 37: Contributions of all sources to systematic uncertainty of the inverse slope parameter in Ar+Sc collisions at beam momentum 40*A* GeV/*c*. Blue dashed line represents nominal value (with standard list of cuts).

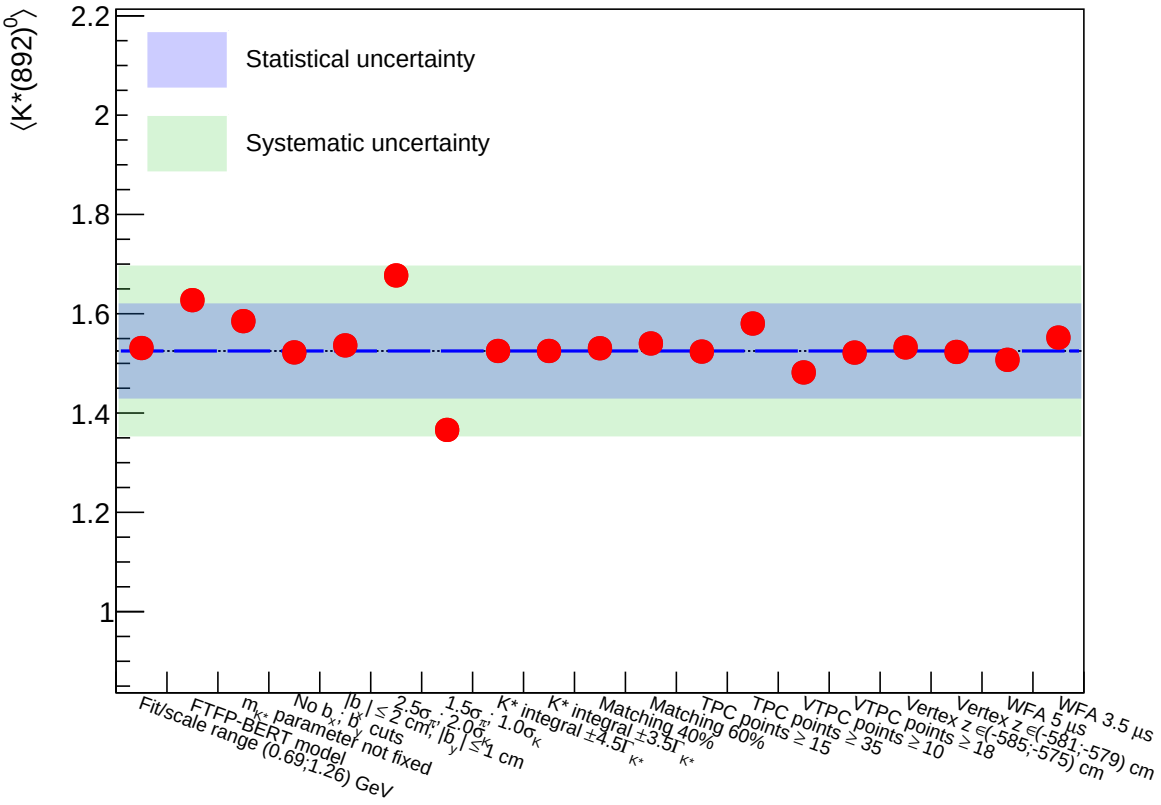

Figure 38: Contributions of all sources to systematic uncertainty of the mean multiplicity of $K^*(892)^0$ in Ar+Sc collisions at beam momentum 75A GeV/c. Blue dashed line represents nominal value (with standard list of cuts).

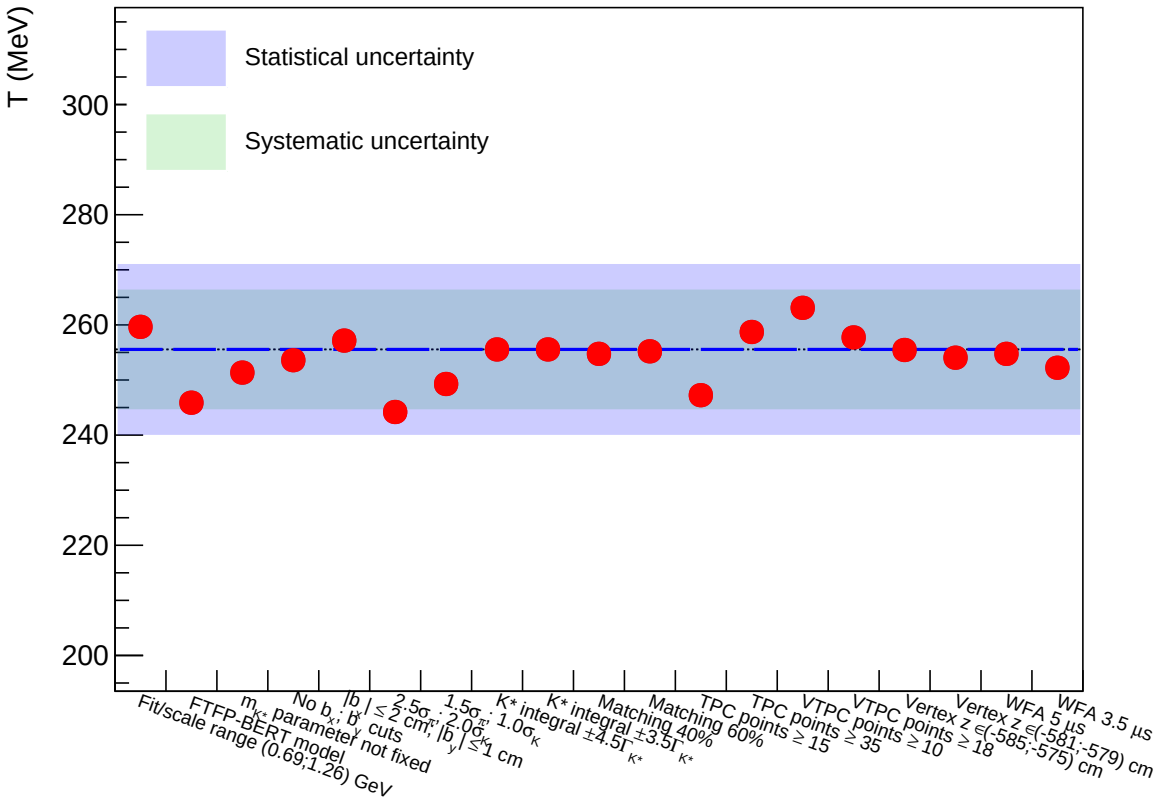

Figure 39: Contributions of all sources to systematic uncertainty of the inverse slope parameter in Ar+Sc collisions at beam momentum 75*A* GeV/*c*. Blue dashed line represents nominal value (with standard list of cuts).

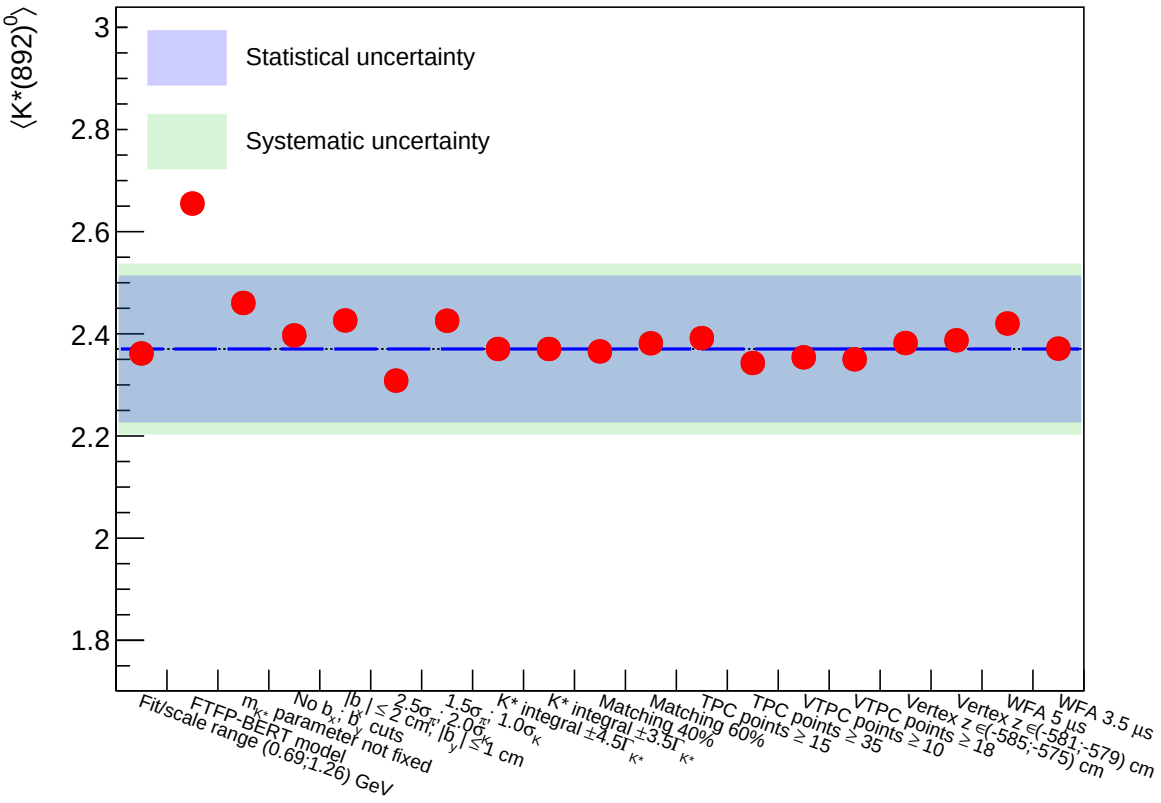

Figure 40: Contributions of all sources to systematic uncertainty of the mean multiplicity of $K^*(892)^0$ in Ar+Sc collisions at beam momentum 150A GeV/c. Blue dashed line represents nominal value (with standard list of cuts).

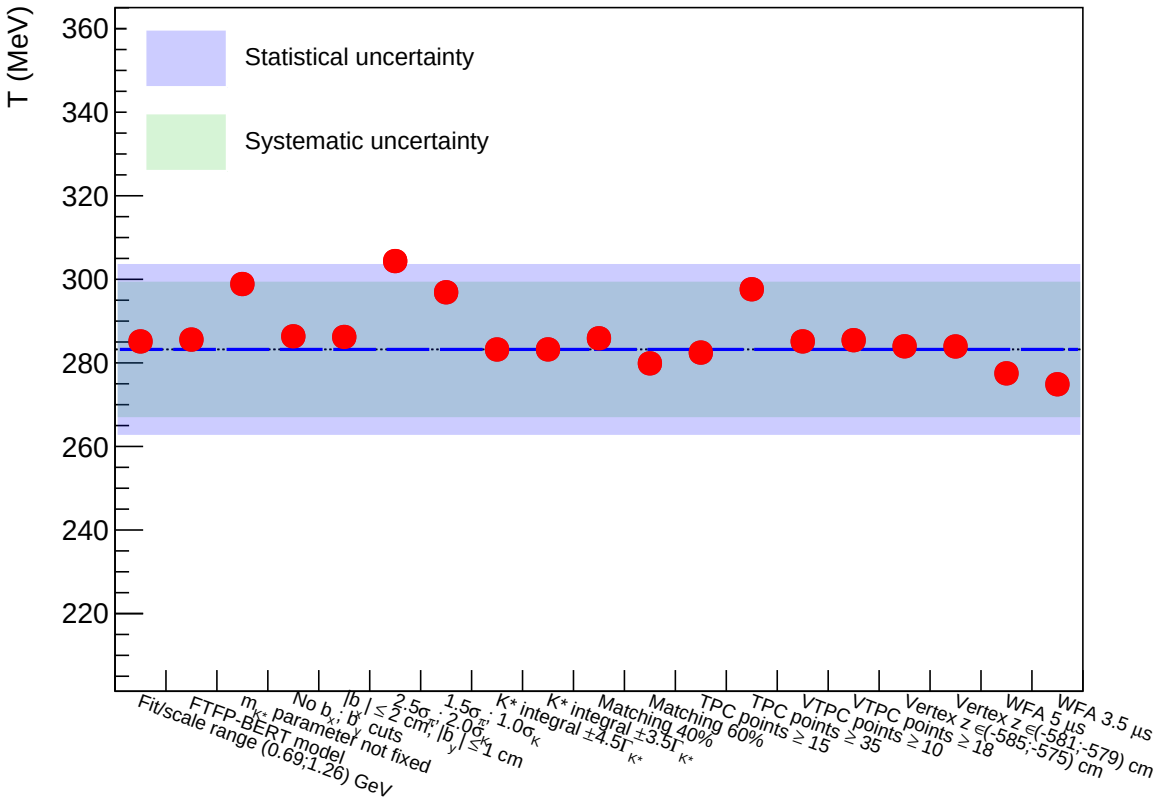

Figure 41: Contributions of all sources to systematic uncertainty of the inverse slope parameter in Ar+Sc collisions at beam momentum 150*A* GeV/*c*. Blue dashed line represents nominal value (with standard list of cuts).

6.9 Time between freeze-outs

The time between chemical and kinetic freeze-outs in Ar+Sc collisions was estimated by studying the ratios of $K^*(892)^0$ to charged kaon yields in Ar+Sc and p+p collisions. Assuming that there are no regeneration processes, the time between freeze-outs in $K^*(892)^0$ rest frame can be described using the following relation [15, 30]:

$$\frac{K^*}{K}\Big|_{\text{kinetic}} = \frac{K^*}{K}\Big|_{\text{chemical}} \cdot e^{-\frac{\Delta t}{\tau}}, \tag{24}$$

where:

- $K^* = \langle K^*(892)^0 \rangle$ represents mean multiplicity of $K^*(892)^0$,
- $K = \langle K^{\pm} \rangle$ represents mean multiplicity of charged kaons (K^+ or K^-),
- $\frac{K^*}{K}|_{\text{chemical}}$ represents ratio in inelastic p+p collisions and can be treated as ratio obtained at chemical freeze-out,
- $\frac{K^*}{K}|_{\text{kinetic}}$ represents ratio in central Ar+Sc collisions and can be treated as ratio obtained at kinetic freeze-out,
- $\tau = 4.17$ fm/c is the mean lifetime of $K^*(892)^0$ calculated based on PDG [5],
- Δt represents the estimated time between chemical and kinetic freeze-outs in the $K^*(892)^0$ rest frame.

The time between freeze-outs calculated using Eq. (24) should be multiplied by a Lorentz factor [39]:

$$\gamma \approx \sqrt{1 + (\langle p_{\text{T}} \rangle / m_0 c)^2}, \tag{25}$$

where

$$\langle p_{\text{T}} \rangle = \int_0^{\infty} A \cdot p_{\text{T}}^2 \exp\left(-\frac{\sqrt{p_{\text{T}}^2 + m_0^2}}{T} \right) \tag{26}$$

is the mean value of $K^*(892)^0$ transverse momentum calculated as the mean value[10] of p_{T} from the fitted function described by Eq. (16). The $\langle p_{\text{T}} \rangle$ value is used as an approximation for $K^*(892)^0$ meson total momentum for the measurements at mid-rapidity [39].

The total uncertainty of the Lorentz factor can be estimated using the following formula:

$$\Delta_{\text{total}}\gamma = \frac{\langle p_{\text{T}} \rangle}{(m_0 c)^2 \sqrt{1 + \left(\frac{\langle p_{\text{T}} \rangle}{m_0 c}\right)^2}} \cdot \Delta_{\text{total}} \langle p_{\text{T}} \rangle, \tag{27}$$

[10] The integral in Eq. (26) was calculated in range $p_{\text{T}} \in (0.0; 100)$ GeV/c.

where $\Delta_{\text{total}}\langle p_{\text{T}}\rangle$ is the total uncertainty ($\sqrt{\text{stat}^2+\text{sys}^2}$) of the mean value of transverse momentum. The statistical and systematic uncertainties of mean value of transverse momentum were obtained based on statistical and systematic uncertainties of inverse slope parameter obtained from fitting Eq. (16) to transverse momentum spectra of $K^*(892)^0$ mesons.

The total uncertainty of time between freeze-outs in the $K^*(892)^0$ rest frame was calculated using equation:

$$\Delta_{\text{total}}(\Delta t) = \tau\sqrt{\left(\frac{K^*}{K}\,|_{\text{chemical}}\right)^{-2}\cdot\left(\Delta_{\text{total}}\frac{K^*}{K}\,|_{\text{chemical}}\right)^2+\left(\frac{K^*}{K}\,|_{\text{kinetic}}\right)^{-2}\cdot\left(\Delta_{\text{total}}\frac{K^*}{K}\,|_{\text{kinetic}}\right)^2}, \tag{28}$$

where total uncertainty of $K^*(892)^0$ to K ratio ($\Delta_{\text{total}}\frac{K^*}{K}$) was calculated by propagating total uncertainties of multiplicities of $K^*(892)^0$ mesons and charged kaons.

The total uncertainty of Lorentz boosted time between freeze-outs was estimated using formula:

$$\Delta_{\text{total}}(\gamma\Delta t) = \sqrt{(\gamma\Delta_{\text{total}}(\Delta t))^2+(\Delta t\Delta_{\text{total}}\gamma)^2}. \tag{29}$$

7 Results

In this chapter the results on $K^*(892)^0$ meson production in Ar+Sc collisions at beam momenta 40A, 75A, and 150A GeV/c ($\sqrt{s_{\mathrm{NN}}}$ = 8.8, 11.9, and 16.8 GeV) are presented. In Sec. 7.1 transverse momentum and transverse mass spectra, obtained values of inverse slope parameters T, and mean transverse momenta $\langle p_{\mathrm{T}} \rangle$ are shown. Results on measured rapidity distributions are presented in Sec. 7.2. At the end of the chapter, in Sec. 7.3, the mean multiplicities of $K^*(892)^0$ mesons are discussed.

7.1 Transverse momentum and transverse mass spectra of $K^*(892)^0$

Transverse momentum spectra of $K^*(892)^0$ mesons in Ar+Sc collisions at beam momenta 40A, 75A, and 150A GeV/c were obtained by analysis of invariant mass distributions of $K^*(892)^0$ mesons in transverse momentum bins and one rapidity bin $y \in (0.0;1.5)$ (division of kinematic space on rapidity and transverse momentum bins was described in Sec. 6.1). Figure 42 shows transverse momentum distributions for all measured beam momenta. The numerical values with statistical and systematic uncertainties are presented in Table 16. Values of inverse slope parameters T and mean transverse momenta $\langle p_{\mathrm{T}} \rangle$ with statistical and systematic uncertainties are shown in Table 17.

Transverse mass spectra of $K^*(892)^0$ mesons in Ar+Sc collisions at all measured beam momenta are presented in Fig. 43. Distributions were obtained by transforming transverse momentum spectra according to Eq. (17). The numerical values of transverse mass spectra with statistical and systematic uncertainties are shown in Table 18.

$\frac{\mathrm{d}^2n}{\mathrm{d}y\mathrm{d}p_{\mathrm{T}}}$ ((GeV/c)$^{-1}$)			
y and p_{T} bins	Ar+Sc at 40A GeV/c	Ar+Sc at 75A GeV/c	Ar+Sc at 150A GeV/c
$y \in (0.0;1.5)$, $p_{\mathrm{T}} \in (0.0;0.4)$ GeV/c	$0.326 \pm 0.057 \pm 0.059$	$0.273 \pm 0.035 \pm 0.043$	$0.409 \pm 0.057 \pm 0.045$
$y \in (0.0;1.5)$, $p_{\mathrm{T}} \in (0.4;0.8)$ GeV/c	$0.357 \pm 0.056 \pm 0.045$	$0.693 \pm 0.050 \pm 0.066$	$0.697 \pm 0.066 \pm 0.036$
$y \in (0.0;1.5)$, $p_{\mathrm{T}} \in (0.8;1.2)$ GeV/c	$0.355 \pm 0.040 \pm 0.048$	$0.300 \pm 0.039 \pm 0.044$	$0.524 \pm 0.050 \pm 0.049$
$y \in (0.0;1.5)$, $p_{\mathrm{T}} \in (1.2;1.5)$ GeV/c	$0.063 \pm 0.018 \pm 0.017$	$0.136 \pm 0.026 \pm 0.014$	$0.204 \pm 0.039 \pm 0.036$

Table 16: Numerical results of $\frac{\mathrm{d}^2n}{\mathrm{d}y\mathrm{d}p_{\mathrm{T}}}$ spectra in 0-10% central Ar+Sc collisions at 40A, 75A, and 150A GeV/c. The first uncertainty is the statistical one, the second – systematic.

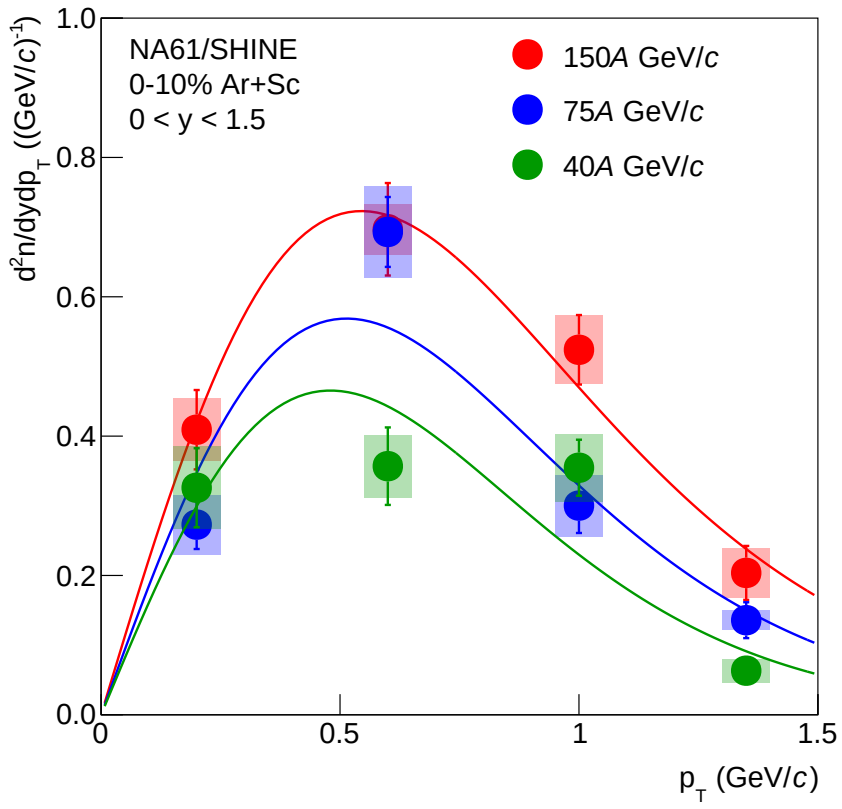

Figure 42: Transverse momentum distributions of $K^*(892)^0$ resonances in central Ar+Sc collisions at beam momenta 40*A*, 75*A*, 150*A* GeV/*c*. Spectra were obtained for rapidity range $y \in (0.0; 1.5)$. Vertical bars represent statistical uncertainties whereas colour bands – systematic ones. The function given by Eq. (16) was fitted to each transverse momentum distribution (solid lines), allowing to obtain inverse slope parameter T and mean transverse momentum $\langle p_T \rangle$ of $K^*(892)^0$ mesons.

	Ar+Sc at 40*A* GeV/*c*	Ar+Sc at 75*A* GeV/*c*	Ar+Sc at 150*A* GeV/*c*
T (MeV)	$227 \pm 17 \pm 20$	$256 \pm 16 \pm 11$	$283 \pm 20 \pm 16$
$\langle p_T \rangle$ (GeV/*c*)	$686 \pm 34 \pm 40$	$745 \pm 31 \pm 22$	$800 \pm 40 \pm 32$

Table 17: Values of inverse slope parameters and mean transverse momenta obtained from transverse momentum spectra in 0-10% central Ar+Sc collisions at 40*A*, 75*A*, and 150*A* GeV/*c*. The first uncertainty is the statistical one, the second – systematic.

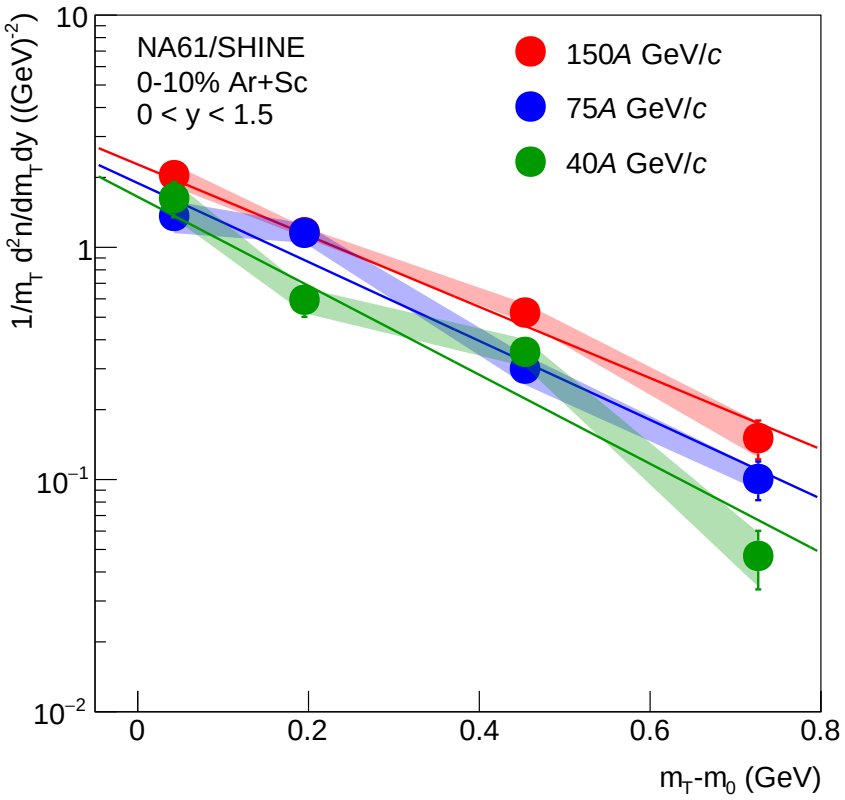

Figure 43: Transverse mass distributions of $K^*(892)^0$ resonances in central Ar+Sc collisions at beam momenta 40*A*, 75*A*, 150*A* GeV/*c*. Spectra were obtained for rapidity range $y \in (0.0; 1.5)$. Vertical bars represent statistical uncertainties whereas colour bands – systematic ones. Function given by Eq. (16) fitted to transverse momentum distributions (Fig. 42), was transformed according to Eq. (17) and resulting curves are presented as the solid lines. Parameter m_0 is the mass of $K^*(892)^0$ resonance taken from PDG [5].

$\frac{1}{m_T}\frac{d^2n}{dm_T dy}$ ($(GeV)^{-2}$)				
y, p_T, and m_T bins	m_T- m_0 (GeV) (bin centre)	Ar+Sc at 40A GeV/c	Ar+Sc at 75A GeV/c	Ar+Sc at 150A GeV/c
$y \in (0.0; 1.5)$, $p_T \in (0.0; 0.4)$ GeV/c, $m_T \in (0.000; 0.085)$ GeV	0.043	$1.63 \pm 0.28 \pm 0.30$	$1.36 \pm 0.18 \pm 0.21$	$2.05 \pm 0.28 \pm 0.23$
$y \in (0.0; 1.5)$, $p_T \in (0.4; 0.8)$ GeV/c, $m_T \in (0.085; 0.305)$ GeV	0.195	$0.595 \pm 0.093 \pm 0.074$	$1.155 \pm 0.084 \pm 0.11$	$1.162 \pm 0.11 \pm 0.060$
$y \in (0.0; 1.5)$, $p_T \in (0.8; 1.2)$ GeV/c, $m_T \in (0.305; 0.602)$ GeV	0.454	$0.355 \pm 0.040 \pm 0.048$	$0.300 \pm 0.039 \pm 0.044$	$0.524 \pm 0.050 \pm 0.049$
$y \in (0.0; 1.5)$, $p_T \in (1.2; 1.5)$ GeV/c, $m_T \in (0.602; 0.851)$ GeV	0.727	$0.047 \pm 0.013 \pm 0.012$	$0.101 \pm 0.019 \pm 0.010$	$0.151 \pm 0.029 \pm 0.026$

Table 18: Numerical results of $\frac{d^2n}{m_T dm_T dy}$ spectra in 0-10% central Ar+Sc collisions at 40A, 75A, and 150A GeV/c. The m_T values are calculated for transverse momentum bin centres. The first uncertainty is the statistical one, the second – systematic.

7.2 Rapidity spectra of $K^*(892)^0$

Rapidity spectra of $K^*(892)^0$ resonances in Ar+Sc collisions at beam momenta 40*A*, 75*A*, and 150*A* GeV/*c* were obtained by analysis of invariant mass distributions of $K^*(892)^0$ mesons in rapidity bins and one transverse momentum bin $p_T \in (0.0; 1.5)$ GeV/*c* (division of kinematic space on rapidity and transverse momentum bins was described in Sec. 6.1). Rapidity distributions for all measured beam momenta are presented in Fig. 44. Numerical values of measured rapidity spectra with statistical and systematic uncertainties are presented in Table 19.

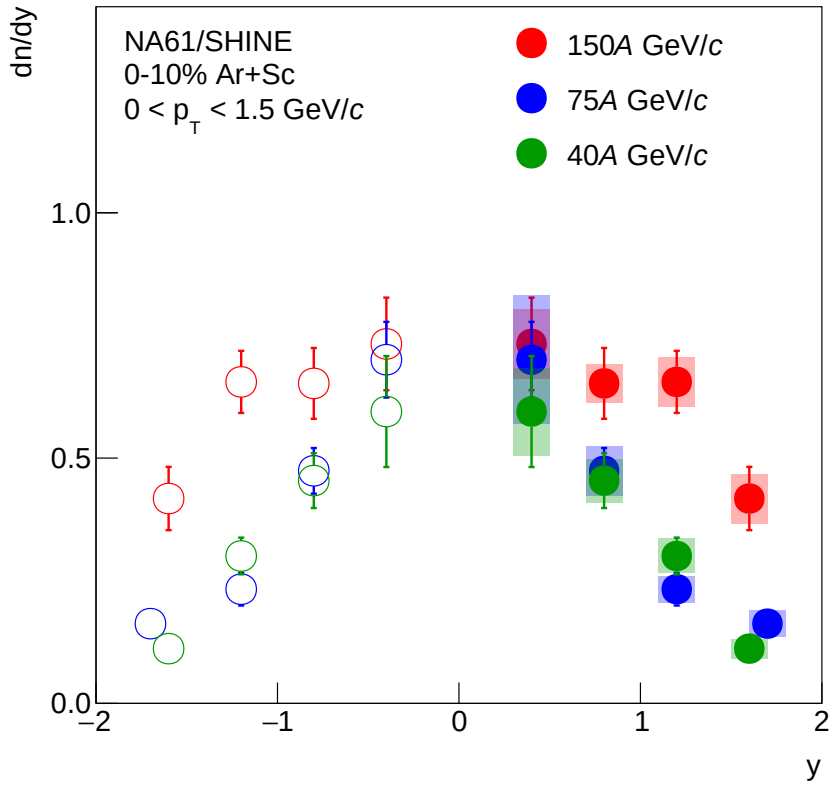

Figure 44: Rapidity distributions of $K^*(892)^0$ resonances in central Ar+Sc collisions at beam momenta 40*A*, 75*A*, 150*A* GeV/*c*. Spectra were obtained for transverse momentum range $y \in (0.0; 1.5)$ GeV/*c*. Full points represent results obtained from measured data. Empty points are reflections of measured points around mid-rapidity. Vertical bars represent statistical uncertainties whereas colour bands – systematic ones.

7.3 Mean multiplicities of $K^*(892)^0$

The mean multiplicities of $K^*(892)^0$ mesons were calculated using measured rapidity spectra presented in Fig. 44 and rapidity distributions taken from Monte Carlo simulation

$\frac{dn}{dy}$		
y and p_T bins	Ar+Sc at 40A GeV/c	Ar+Sc at 150A GeV/c
$y \in (0.2;0.6), p_T \in (0.0;1.5)$ GeV/c	$0.595 \pm 0.11 \pm 0.089$	$0.733 \pm 0.094 \pm 0.071$
$y \in (0.6;1.0), p_T \in (0.0;1.5)$ GeV/c	$0.454 \pm 0.056 \pm 0.044$	$0.652 \pm 0.072 \pm 0.039$
$y \in (1.0;1.4), p_T \in (0.0;1.5)$ GeV/c	$0.300 \pm 0.037 \pm 0.036$	$0.655 \pm 0.063 \pm 0.050$
$y \in (1.4;1.8), p_T \in (0.0;1.5)$ GeV/c	$0.112 \pm 0.029 \pm 0.020$	$0.418 \pm 0.064 \pm 0.050$
y and p_T bins	Ar+Sc at 75A GeV/c	
$y \in (0.2;0.6), p_T \in (0.0;1.5)$ GeV/c	$0.701 \pm 0.077 \pm 0.13$	
$y \in (0.6;1.0), p_T \in (0.0;1.5)$ GeV/c	$0.474 \pm 0.046 \pm 0.051$	
$y \in (1.0;1.4), p_T \in (0.0;1.5)$ GeV/c	$0.233 \pm 0.033 \pm 0.027$	
$y \in (1.4;2.0), p_T \in (0.0;1.5)$ GeV/c	$0.163 \pm 0.026 \pm 0.027$	

Table 19: Numerical results of $\frac{dn}{dy}$ spectra in 0-10% central Ar+Sc collisions at 40A, 75A, and 150A GeV/c. The first uncertainty is the statistical one, the second – systematic.

(mean multiplicity calculation method is presented in Sec. 6.7). Results of these calculations are presented in Fig. 45. Mean multiplicity numerical values with statistical and systematic uncertainties are shown in Table 20.

	Ar+Sc at 40A GeV/c	Ar+Sc at 75A GeV/c	Ar+Sc at 150A GeV/c
$\langle K^*(892)^0 \rangle$	$1.41 \pm 0.13 \pm 0.12$	$1.525 \pm 0.096 \pm 0.17$	$2.37 \pm 0.14 \pm 0.17$

Table 20: Mean multiplicities of $K^*(892)^0$ resonances in 0-10% central Ar+Sc collisions at 40A, 75A, and 150A GeV/c. The first uncertainty is the statistical one, the second – systematic.

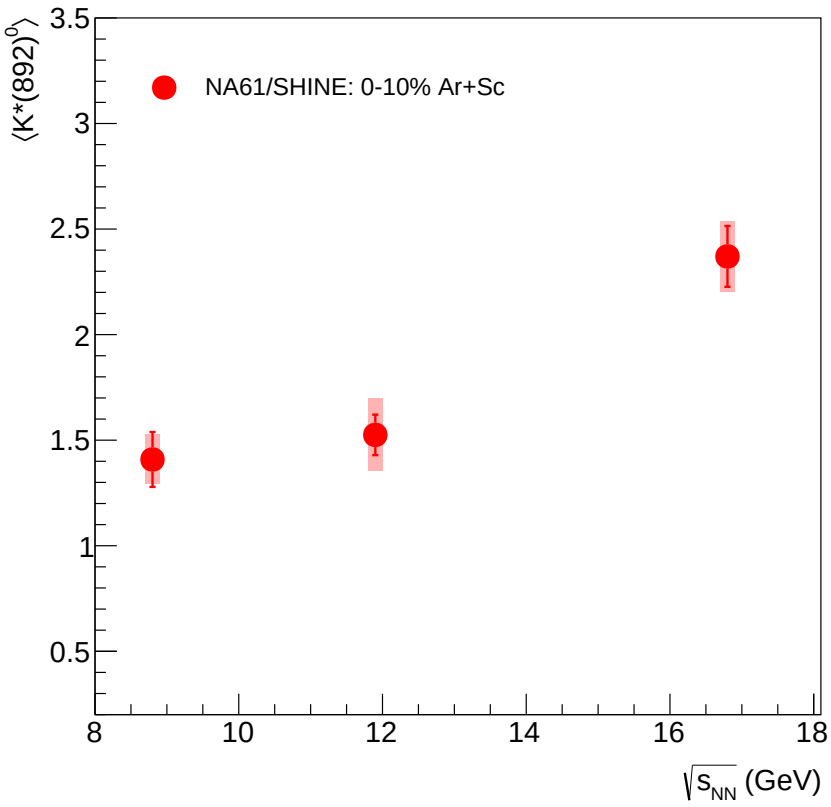

Figure 45: Energy dependence of mean multiplicity of $K^*(892)^0$ resonances in central Ar+Sc collisions at beam momenta 40*A*, 75*A*, 150*A* GeV/*c* ($\sqrt{s_{\mathrm{NN}}}$ = 8.8, 11.9, and 16.8 GeV). Vertical bars represent statistical uncertainties whereas colour bands – systematic ones.

8 Comparison with model predictions and world data

This chapter presents comparisons of results from Ar+Sc collisions at 40*A*, 75*A*, and 150*A* GeV/*c* beam momenta ($\sqrt{s_{\mathrm{NN}}}$ = 8.8, 11.9, and 16.8 GeV) to model predictions and results from the NA61/SHINE and NA49 experiments. In Sec. 8.1, the measured rapidity spectra are compared with predictions from the EPOS1.99 and FTFP-BERT models. In Sec. 8.2 the obtained results of mean multiplicities of $K^*(892)^0$ mesons and inverse slope parameters T are compared with results from NA61/SHINE and NA49. In Sec. 8.3 the K^*/K ratios are presented and the time between freeze-outs is estimated for Ar+Sc and Pb+Pb collisions at the SPS energies.

8.1 Comparison of rapidity spectra with EPOS1.99 and FTFP-BERT

The measured rapidity spectra of $K^*(892)^0$ resonances in Ar+Sc collisions at beam momenta 40*A*, 75*A*, and 150*A* GeV/*c* were compared with rapidity distributions predicted by the EPOS1.99 and FTFP-BERT models. Comparison between measurements and model predictions are presented in Figs. 46, 47, and 48. Results of this comparison showed that the EPOS model overestimates $K^*(892)^0$ production at all analysed beam momenta. In contrast, the FTFP-BERT model underestimates the $K^*(892)^0$ production in central Ar+Sc collisions at SPS energies.

8.2 Comparison of results with NA49 and NA61/SHINE

The measured mean multiplicities $\langle K^*(892)^0 \rangle$ and inverse slope parameters T of $K^*(892)^0$ transverse momentum spectra in Ar+Sc collisions at the three SPS energies were compared with results of NA61/SHINE and NA49 for other collision systems. In Fig. 49, the energy dependence of mean multiplicity of $K^*(892)^0$ mesons from Ar+Sc collisions is compared with results from *p*+*p* collisions from Refs. [41] and [81]. Unlike in Ar+Sc, in $K^*(892)^0$ analysis in *p*+*p* collisions, the rapidity spectra were fitted with the Gaussian function. Then, the mean multiplicity of $K^*(892)^0$ was calculated as the sum of measured points and integral over the Gaussian function in the unmeasured regions. Both systems show a monotonic increase of mean multiplicity with collision energy.

Figure 50 shows a comparison of the mean multiplicity of $K^*(892)^0$ mesons measured in central Ar+Sc collisions at beam momentum 150*A* GeV/*c* with results from other collision systems at similar energy. All compared results from the NA61/SHINE [41] and NA49 [29] experiments were measured at beam momentum 158*A* GeV/*c*. The mean multiplicity of $K^*(892)^0$ in *p*+*p* and Pb+Pb collisions in the NA49 experiment were calculated as integral over the fitted Gaussian function. Due to small statistics, results from C+C and Si+Si collisions were

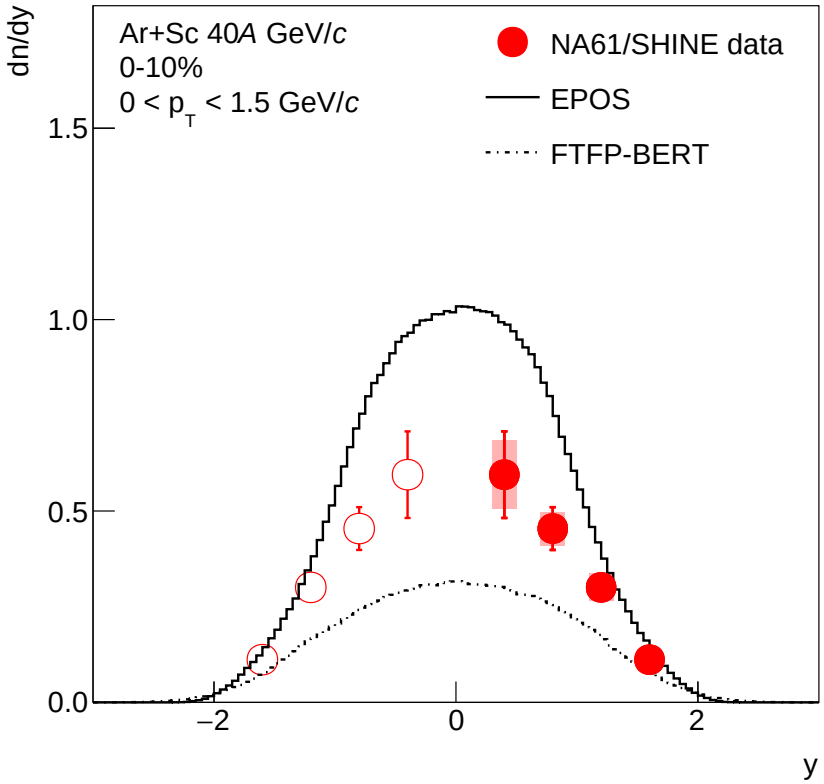

Figure 46: Comparison of rapidity distribution of $K^*(892)^0$ resonances in central Ar+Sc collisions at beam momentum 40*A* GeV/*c* with predictions from the EPOS1.99 and FTFP-BERT models. As in the data, model predictions were obtained for 0-10% central Ar+Sc collisions in transverse momentum range $p_T \in (0.0; 1.5)$ GeV/*c*. For NA61/SHINE data, vertical bars represent statistical uncertainties whereas colour bands – systematic ones.

estimated from a single $K^*(892)^0$ yield extracted from invariant mass distribution in a wide bin of rapidity $y \in (0.2; 1.8)$ and transverse momentum $p_T \in (0.0; 1.5)$ GeV/*c*. The value of mean multiplicity of $K^*(892)^0$ mesons in *p*+*p* collision taken from the NA61/SHINE experiment was calculated as the sum of measured points and integral over the Gaussian function in the unmeasured regions. The comparison shows that the value of the mean multiplicity of $K^*(892)^0$ resonances increases linearly with the number of wounded nucleons.

The comparison of the inverse slope parameter of transverse momentum spectra in Ar+Sc collisions with results from *p*+*p* collisions from the NA61/SHINE experiment is shown in Fig. 51. The values of inverse slope parameters in *p*+*p* collisions at 40 and 80 GeV/*c* were measured in the same rapidity and transverse momentum range as in Ar+Sc analysis. Due to high statistics, in *p*+*p* collisions at beam momentum 158 GeV/*c*, the values of inverse slope parameters were obtained in few rapidity bins. For this comparison the result in rapidity range

8 COMPARISON WITH MODEL PREDICTIONS AND WORLD DATA

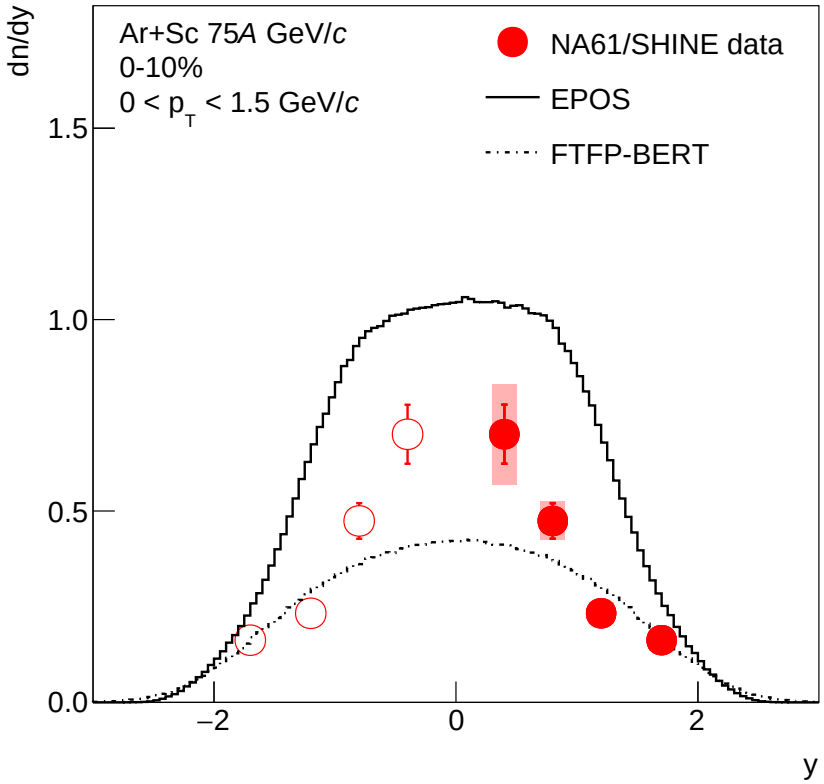

Figure 47: Comparison of rapidity distribution of $K^*(892)^0$ resonances in central Ar+Sc collisions at beam momentum 75*A* GeV/*c* with predictions from the EPOS1.99 and FTFP-BERT models. As in the data, model predictions were obtained for 0-10% central Ar+Sc collisions in transverse momentum range $p_T \in (0.0; 1.5)$ GeV/*c*. For NA61/SHINE data, vertical bars represent statistical uncertainties whereas colour bands – systematic ones.

$y \in (0.0; 0.5)$ was taken [41]. All compared values were obtained using the same function (Eq. (16)) fitted to transverse momentum spectra. The results show a small increase of inverse slope parameter with collision energy. This effect looks stronger in Ar+Sc (heavier system) than in *p*+*p* (lighter system). Moreover, the larger values of T in Ar+Sc than in *p*+*p* can be attributed to the radial flow present in heavier nucleus-nucleus systems.

Finally, in Fig. 52, the inverse slope parameter measured in Ar+Sc collisions at beam momentum 150*A* GeV/*c* is compared with results from *p*+*p* and Pb+Pb collisions at beam momentum 158*A* GeV/*c* [29, 41]. The result of the NA61/SHINE experiment in *p*+*p* collisions was obtained in rapidity range $y \in (0.0; 0.5)$ using an exponential function (Eq. (16)) fitted to transverse momentum distribution. Results from the NA49 experiment in *p*+*p* and Pb+Pb were obtained in rapidity ranges $y \in (0.2; 0.7)$ and $y \in (0.43; 1.78)$, respectively, using exponential function fitted to transverse mass spectra. The comparison shows a logarithmic increase of

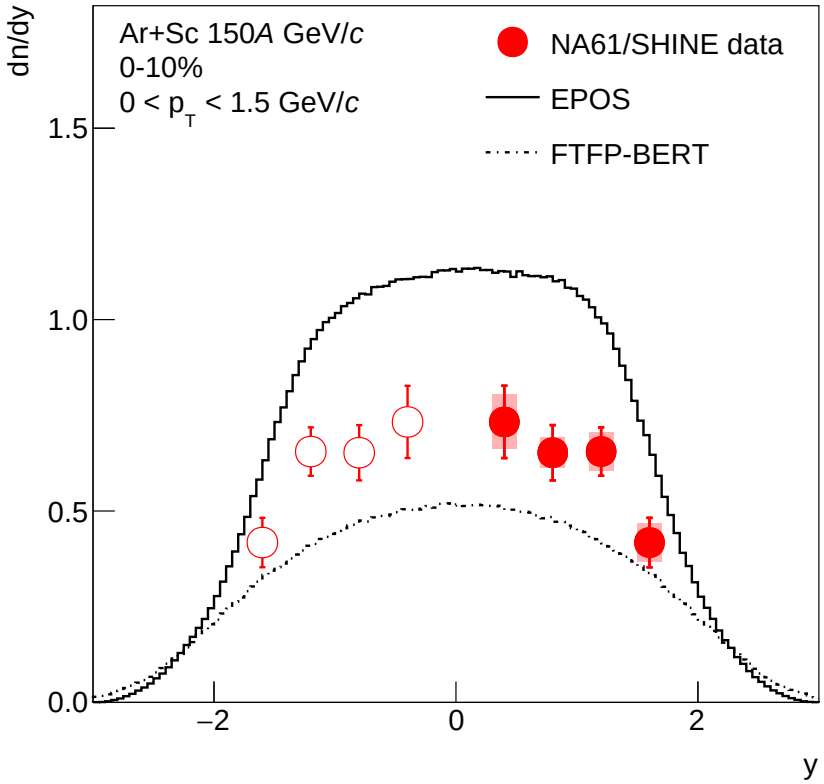

Figure 48: Comparison of rapidity distribution of $K^*(892)^0$ resonances in central Ar+Sc collisions at beam momentum 150*A* GeV/*c* with predictions from the EPOS1.99 and FTFP-BERT models. As in the data, model predictions were obtained for 0-10% central Ar+Sc collisions in transverse momentum range $p_T \in (0.0; 1.5)$ GeV/*c*. For NA61/SHINE data, vertical bars represent statistical uncertainties whereas colour bands – systematic ones.

the inverse slope parameter with a number of wounded nucleons. The difference between the Ar+Sc and Pb+Pb results can be attributed to differences in radial flow. The radial flow in Pb+Pb collisions is larger than in Ar+Sc, resulting in a higher value of inverse slope parameter of transverse momentum spectra of $K^*(892)^0$ resonances.

8 COMPARISON WITH MODEL PREDICTIONS AND WORLD DATA

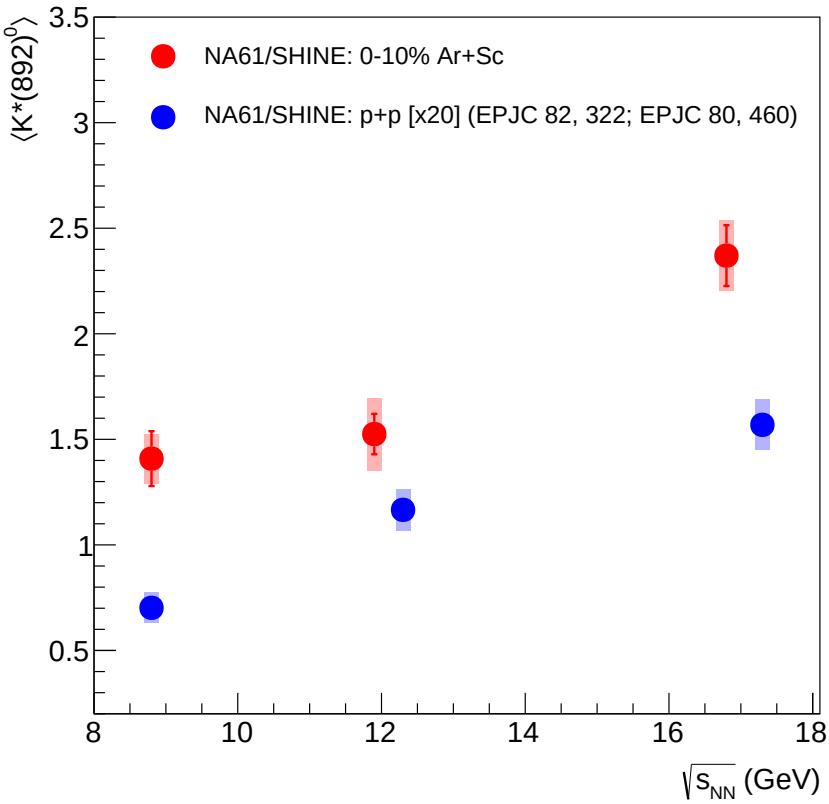

Figure 49: Comparison of mean multiplicity of $K^*(892)^0$ resonances in central Ar+Sc collisions at beam momenta 40*A*, 75*A*, and 150*A* GeV/*c* ($\sqrt{s_{\mathrm{NN}}}$ = 8.8, 11.9, and 16.8 GeV) with results of measurements in *p*+*p* collisions at beam momenta 40, 80, 158 GeV/*c* ($\sqrt{s_{\mathrm{NN}}}$ = 8.8, 12.3, and 17.3 GeV) [41, 81]. Values of mean multiplicities of $K^*(892)^0$ in *p*+*p* collisions were scaled by factor 20 to be comparable to results measured in Ar+Sc collisions. Vertical bars represent statistical uncertainties whereas colour bands – systematic ones.

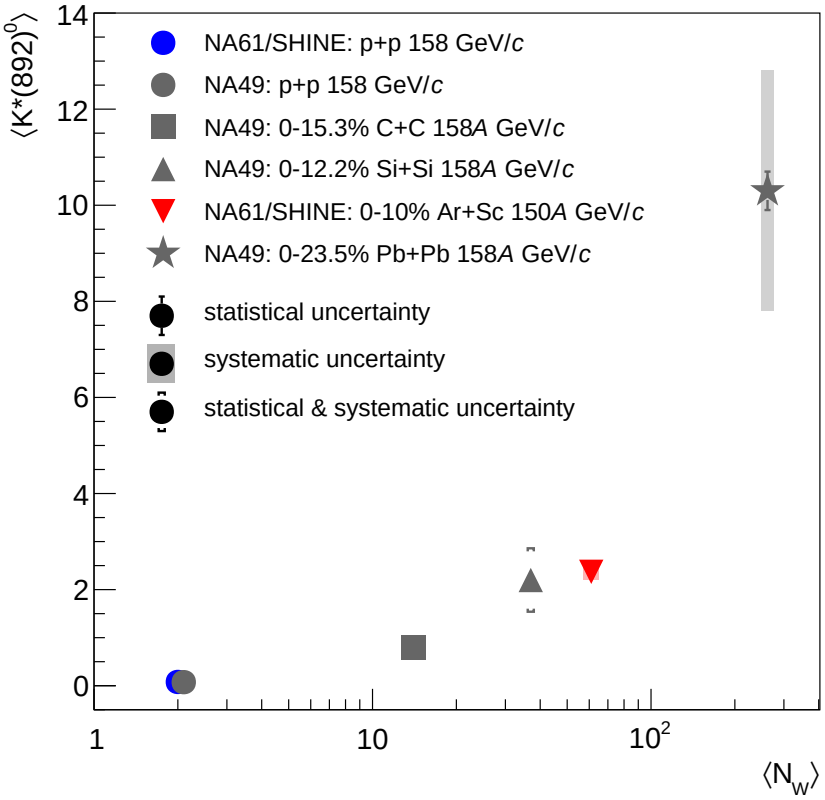

Figure 50: Comparison of mean multiplicity of $K^*(892)^0$ resonances in central Ar+Sc collisions at beam momentum 150*A* GeV/*c* with results of measurements in other collision systems [29, 41]. Results of measurements from *p*+*p*, Ar+Sc, and Pb+Pb collisions are presented with statistical and systematic uncertainties. Results from C+C and Si+Si collisions are presented with combined statistical and systematic uncertainty only (assigned as 30% of the multiplicity value [29]).

8 COMPARISON WITH MODEL PREDICTIONS AND WORLD DATA

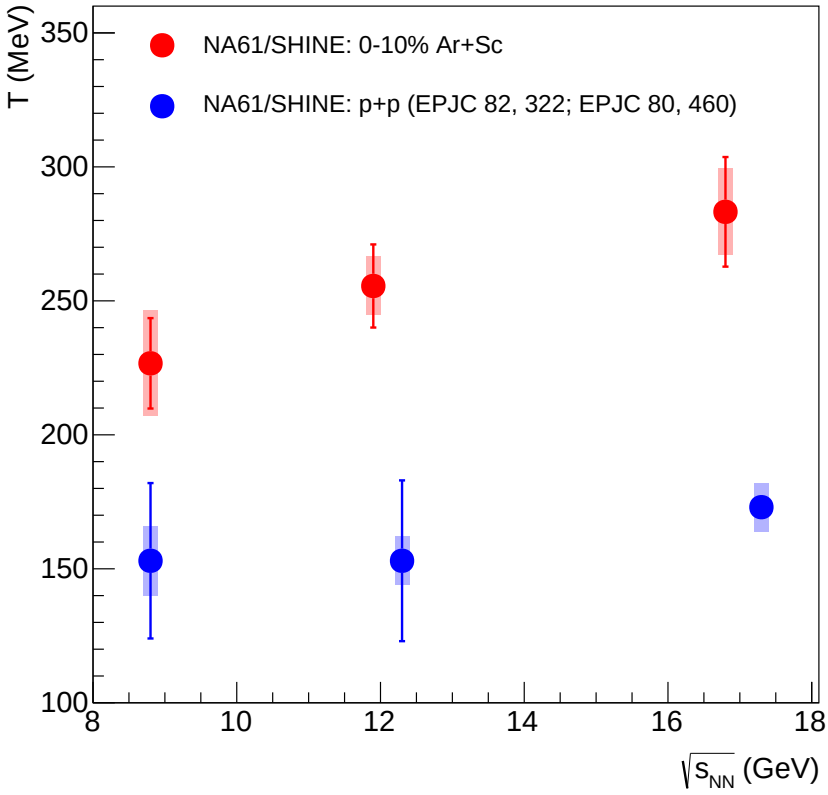

Figure 51: Comparison of inverse slope parameter of transverse momentum spectra of $K^*(892)^0$ resonances in central Ar+Sc collisions at beam momenta 40*A*, 75*A*, and 150*A* GeV/*c* ($\sqrt{s_{\mathrm{NN}}}$ = 8.8, 11.9, and 16.8 GeV) with results of measurements in *p*+*p* collisions at beam momenta 40, 80, 158 GeV/*c* ($\sqrt{s_{\mathrm{NN}}}$ = 8.8, 12.3, and 17.3 GeV) [41, 81]. Value of inverse slope parameter in *p*+*p* at beam momentum 158 GeV/*c* was measured in rapidity range $y \in (0.0; 0.5)$, and for the rest of points, rapidity range $y \in (0.0; 1.5)$ was used. Vertical bars represent statistical uncertainties whereas colour bands – systematic ones.

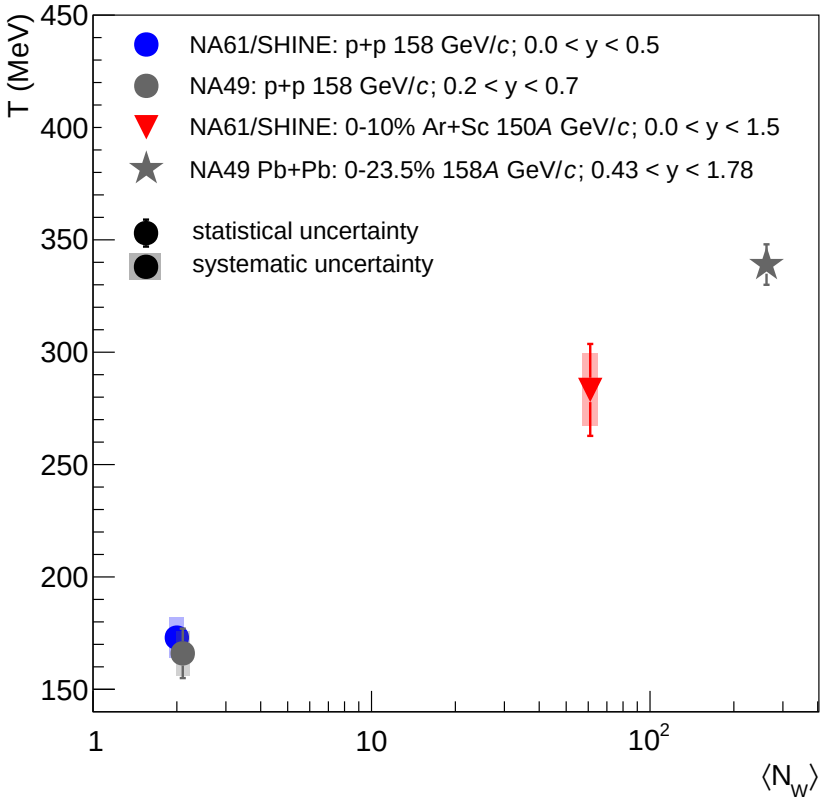

Figure 52: Comparison of inverse slope parameter of transverse momentum spectra of $K^*(892)^0$ resonances in central Ar+Sc collisions at beam momentum 150*A* GeV/*c* with results of measurements in *p*+*p* and Pb+Pb collisions at beam momentum 158*A* GeV/*c* [29, 41]. Results from *p*+*p* and Ar+Sc collisions are presented with statistical (vertical bars) and systematic (colour bands) uncertainties. Systematic uncertainty of inverse slope parameter of transverse momentum spectra of $K^*(892)^0$ in Pb+Pb collisions was not estimated.

8 COMPARISON WITH MODEL PREDICTIONS AND WORLD DATA

8.3 $\langle K^*(892)^0\rangle/\langle K^{\pm}\rangle$ ratio and time between-freeze-outs

The ratio of $K^*(892)^0$ resonance to charged kaon production can be used to estimate the time interval between chemical and kinetic freeze-outs in nucleus-nucleus collisions. One of the advantages of analysing the relation between $K^*(892)^0$ and $K^{\pm}$ is that $K^*(892)^0$ resonance shares the same quark (antiquark) content as $K^{\pm}$ meson but differs in mass and the relative orientations of their quark spins. Consequently, the $\langle K^*(892)^0\rangle/\langle K^{\pm}\rangle$ ratios are considered among the most model-independent metrics for investigating $K^*(892)^0$ production properties and freeze-out conditions [41]. Figures 53, 54, 55 present $K^*(892)^0$ resonance to charged kaon ratios as a function of system size (represented as a number of wounded nucleons) obtained from results of the NA49 and NA61/SHINE experiments as well as from the analysis presented in this thesis (the numerical values are presented in Table 21).

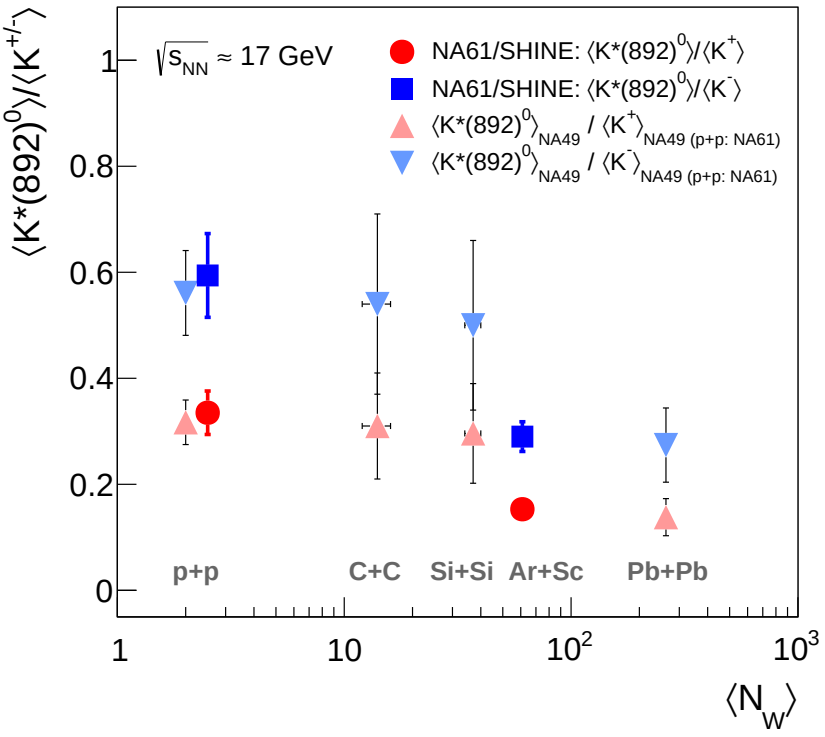

Figure 53: $\langle K^*(892)^0\rangle/\langle K^{\pm}\rangle$ ratio in *p+p*, C+C, Si+Si, Ar+Sc, Pb+Pb collisions at beam momentum 150/158*A* GeV/*c*. Points representing results of *p+p* analysis from NA61/SHINE experiment are shifted to the right for better visibility [41]. The plot was created using numerical data presented in Table 21. Vertical error bars represent total uncertainties.

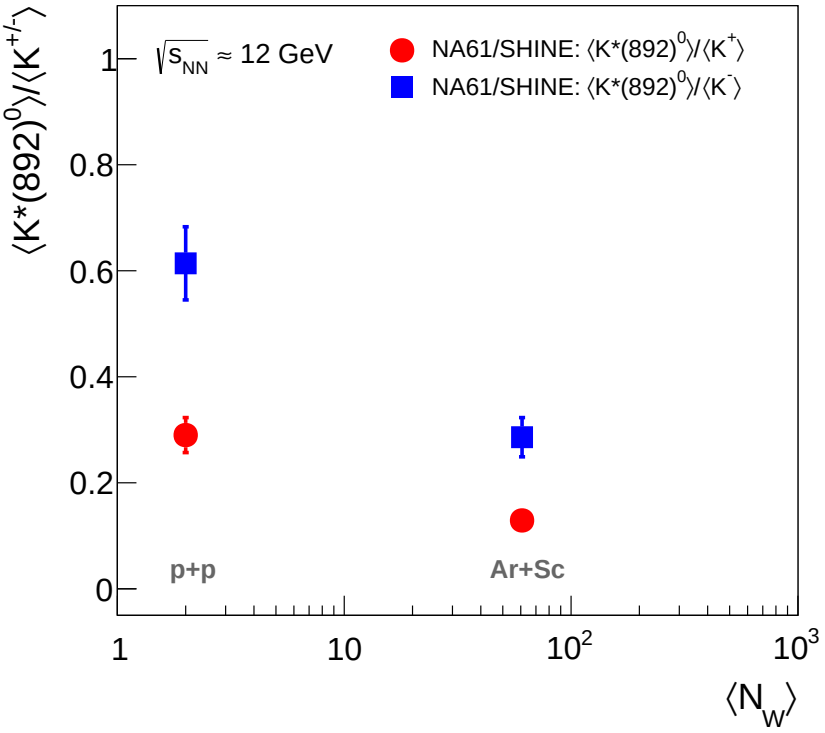

Figure 54: $\langle K^*(892)^0\rangle/\langle K^\pm\rangle$ ratio in p+p and Ar+Sc collisions at beam momentum 75/80A GeV/c. The plot was created using numerical data presented in Table 21. Vertical error bars represent total uncertainties.

The $\langle K^*(892)^0\rangle/\langle K^\pm\rangle$ ratio taken from p+p and nucleus-nucleus collisions can be used to estimate time between freeze-outs in these nucleus-nucleus collisions. Using Eq. (24) and data presented in Table 21, the time intervals between chemical and kinetic freeze-outs in the $K^*(892)^0$ rest frame were estimated. The results were then multiplied by the Lorentz factor given by Eq. (25). Figure 56 presents estimated values of time between freeze-outs ($t_{\mathrm{kin}} - t_{\mathrm{chem}} = \gamma\Delta t$) for Ar+Sc collisions at beam momenta 40A, 75A, and 150A GeV/c and compares them with the value obtained for Pb+Pb collisions at beam momentum 158A GeV/c. The numerical values are shown in Table 22.

The results show that the time between freeze-outs is similar in Ar+Sc collisions at beam momenta 75A and 150A GeV/c. Within uncertainties, the results for Pb+Pb and Ar+Sc collisions at the highest energy are also comparable.

The calculation of the time between freeze-outs assumes that no regeneration processes of $K^*(892)^0$ resonances occur during collision evolution. In reality, $K^*(892)^0$ regeneration can take place for all collision energies. This means that the estimated time interval is, in fact, a lower limit for the duration of the hadronic phase between chemical and kinetic freeze-outs.

8 COMPARISON WITH MODEL PREDICTIONS AND WORLD DATA

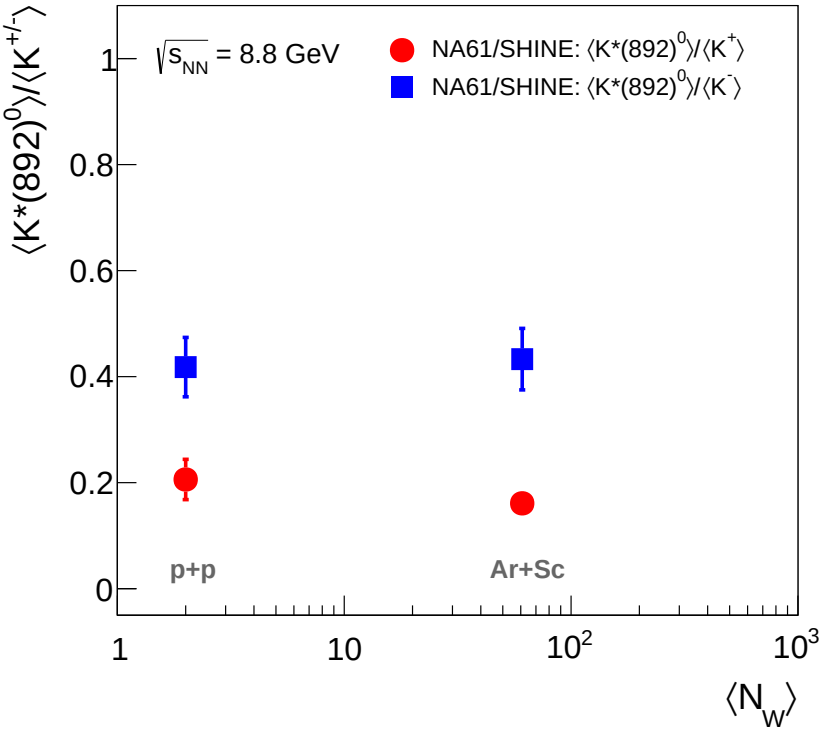

Figure 55: $\langle K^*(892)^0\rangle/\langle K^\pm\rangle$ ratio in p+p and Ar+Sc collisions at beam momentum 40A GeV/c. The plot was created using numerical data presented in Table 21. Vertical error bars represent total uncertainties.

8 COMPARISON WITH MODEL PREDICTIONS AND WORLD DATA

	$\langle K^*(892)^0 \rangle$	$\langle K^+ \rangle$	$\langle K^- \rangle$	$\langle K^*(892)^0 \rangle / \langle K^+ \rangle$	$\langle K^*(892)^0 \rangle / \langle K^- \rangle$
NA61/SHINE *p+p* 158 GeV/*c* N_W =2	0.0784±0.0060 [41]	0.234±0.022 [84]	0.132±0.014 [84]	0.335±0.041	0.594±0.079
NA61/SHINE *p+p* 80 GeV/*c* N_W =2	0.0583±0.0053 [81]	0.201±0.014 [84]	0.0950±0.0064 [84]	0.290±0.033	0.614±0.069
NA61/SHINE *p+p* 40 GeV/*c* N_W =2	0.0351±0.0038 [81]	0.170±0.025 [84]	0.0840±0.0067 [84]	0.206±0.038	0.418±0.056
NA49 *p+p* 158 GeV/*c* N_W =2	0.0741±0.0069 [29]	from NA61/SHINE	from NA61/SHINE	0.317±0.042	0.561±0.080
NA49 15.3% C+C 158*A* GeV/*c* $\langle N_W \rangle$=14±2 [29]	0.80±0.24 [29]	2.54±0.25 [85]	1.49±0.16 [85]	0.31±0.10	0.54±0.17
NA49 12.2% Si+Si 158*A* GeV/*c* $\langle N_W \rangle$=37±3 [29]	2.20±0.66 [29]	7.44±0.74 [85]	4.42±0.44 [85]	0.296±0.094	0.50±0.16
NA61/SHINE 10% Ar+Sc 150*A* GeV/*c* $\langle N_W \rangle$=61.0 [71]	2.37±0.22	15.53±0.53 [71]	8.16±0.25 [71]	0.153±0.015	0.290±0.028
NA61/SHINE 10% Ar+Sc 75*A* GeV/*c* $\langle N_W \rangle$=60.8 [71]	1.53±0.20	11.84±0.40 [71]	5.33±0.14 [71]	0.129±0.017	0.286±0.037
NA61/SHINE 10% Ar+Sc 40*A* GeV/*c* $\langle N_W \rangle$=60.9 [71]	1.41±0.18	8.76±0.42 [71]	3.26±0.15 [71]	0.161±0.022	0.433±0.058
NA49 23.5% Pb+Pb 158*A* GeV/*c* $\langle N_W \rangle$=262±6 [29]	10.3±2.5 [29]	74.5±5.1 (from scaling)	37.6±2.6 (from scaling)	0.138±0.035	0.274±0.070
NA49 5% Pb+Pb 158*A* GeV/*c* $\langle N_W \rangle$=362±5 [86]	–	103.0±7.1 [86]	51.9±3.6 [86]	–	–

Table 21: Mean multiplicities of $K^*(892)^0$, K^+, K^-, and K^*/K ratios measured in nucleus-nucleus collisions by NA49 and NA61/SHINE. The total uncertainties of $\langle K^*(892)^0 \rangle$, $\langle K^+ \rangle$, and $\langle K^- \rangle$ were taken as the square roots of the sums of squares of statistical and systematic uncertainties. In NA49 *p+p* data, the $\langle K^+ \rangle$ and $\langle K^- \rangle$ values include statistical uncertainties only ($\langle K^+ \rangle = 0.2267 \pm 0.0006$ and $\langle K^- \rangle = 0.1303 \pm 0.0004$), because systematic uncertainties for total yields were not reported [87]. Because of that, $\langle K^+ \rangle$ and $\langle K^- \rangle$ values reported by NA61/SHINE were used when calculating the $\langle K^*(892)^0 \rangle / \langle K^+ \rangle$ and $\langle K^*(892)^0 \rangle / \langle K^- \rangle$ ratios. The charged kaon multiplicities in the 23.5% most central Pb+Pb collisions were obtained by multiplying by a factor 262/362 values of $\langle K^+ \rangle$ and $\langle K^- \rangle$ and their uncertainties obtained in the 5% most central Pb+Pb collisions. Table was taken from Ref. [41] and modified by adding results for other energies.

8 COMPARISON WITH MODEL PREDICTIONS AND WORLD DATA

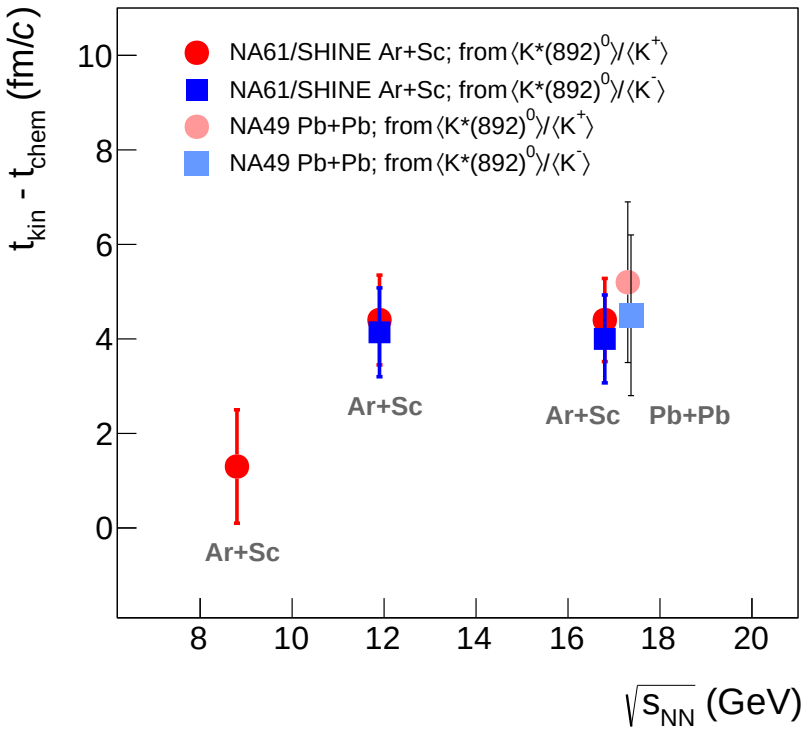

Figure 56: Time between freeze-outs in Ar+Sc ($\sqrt{s_{\mathrm{NN}}}$ = 8.8, 11.9, and 16.8 GeV) and Pb+Pb ($\sqrt{s_{\mathrm{NN}}}$ = 17.3 GeV) collisions. The plot was created using numerical data presented in Table 22. Vertical error bars represent total uncertainties.

	$\langle p_T \rangle$ (GeV/c)	$\Delta t(K^*/K^+)$ (fm/c)	$\Delta t(K^*/K^-)$ (fm/c)	$\gamma\Delta t(K^*/K^+)$ (fm/c)	$\gamma\Delta t(K^*/K^-)$ (fm/c)
NA61/SHINE 10% Ar+Sc 150A GeV/c $\langle N_W \rangle$=61.0 [71]	0.800±0.051	3.28±0.65	2.99±0.69	4.40±0.88	4.00±0.93
NA61/SHINE 10% Ar+Sc 75A GeV/c $\langle N_W \rangle$=60.8 [71]	0.745±0.038	3.39±0.73	3.18±0.72	4.40±0.95	4.14±0.94
NA61/SHINE 10% Ar+Sc 40A GeV/c $\langle N_W \rangle$=60.9 [71]	0.686±0.052	1.04±0.94	-0.14±0.79	1.3±1.2	-0.2±1.0
NA49 23.5% Pb+Pb 158A GeV/c $\langle N_W \rangle$=262±6 [29]	0.877±0.050	3.7±1.2	3.2±1.2	5.2±1.7	4.5±1.7

Table 22: Mean transverse momentum and time between chemical and kinetic freeze-outs in Ar+Sc collisions at beam momenta 40A, 75A, and 150A GeV/c and in Pb+Pb collisions at beam momentum 158A GeV/c. Results were calculated using data on multiplicity ratios presented in Table 21 and values of mean transverse momentum taken from Table 17. Mean transverse momentum in Pb+Pb collisions was estimated by fitting Eq. (16) to transverse momentum spectrum of $K^*(892)^0$ taken from Ref. [29]. During this fitting procedure, uncertainties were taken as the square root of the sums of squares of statistical and systematic uncertainties. Uncertainty of mean transverse momentum was propagated from the uncertainty of inverse slope parameter obtained from the fit.

9 Summary

This thesis presents the results on $K^*(892)^0$ resonance production in the 10% most central Ar+Sc collisions at beam momenta 40*A*, 75*A*, and 150*A* GeV/*c* measured by the NA61/SHINE experiment at the SPS accelerator at CERN. In this analysis, for the first time, the template method was used in ion-ion collisions. This method describes the background in the $K^+\pi^-$ invariant mass spectra using two components. The first is the spectrum of uncorrelated $K^+\pi^-$ pairs generated through the event-mixing method. The second is the distribution obtained from Monte Carlo data, which consists of contribution from $K^+\pi^-$ pairs from resonance decays excluding $K^*(892)^0$ and combination of $K^+\pi^-$ pairs with one particle from a resonance decay and the second one from the direct production in the primary interaction.

The rapidity spectra presented in this thesis were compared with model predictions. Both EPOS1.99 and FTFP-BERT models do not predict the obtained analysis results. The EPOS1.99 model overestimates the $K^*(892)^0$ production, whereas the FTFP-BERT model underestimates the $K^*(892)^0$ production. The obtained mean multiplicities of $K^*(892)^0$ resonances were compared with results from *p*+*p* analysis at all measured energies, and the results from Ar+Sc at 150*A* GeV/*c* were compared with NA49 and NA61/SHINE results for other collision systems.

The values of inverse slope parameters obtained from transverse momentum spectra analysis were compared with results from *p*+*p* collisions at all measured energies, and the result for the highest beam momentum was compared with NA49 and NA61/SHINE results for other collision systems.

The $\langle K^*(892)^0\rangle/\langle K^\pm\rangle$ ratios in Ar+Sc collisions were calculated and compared with other measurements of the NA49 and NA61/SHINE experiments. The results show almost no suppression of $K^*(892)^0$ production in Ar+Sc collisions at beam momentum 40*A* GeV/*c*. The results for Ar+Sc 75*A* and 150*A* GeV/*c* are similar. The suppression of $K^*(892)^0$ resonance in Ar+Sc collisions at 150*A* GeV/*c* is similar to the suppression estimated for Pb+Pb collisions at similar energy.

Using the $\langle K^*(892)^0\rangle/\langle K^\pm\rangle$ ratios obtained in this analysis and the ratios calculated in *p*+*p* collisions, the lower limits of the time between chemical and kinetic freeze-outs in Ar+Sc collisions at beam momenta 40*A*, 75*A*, and 150*A* GeV/*c* were estimated and compared with results from Pb+Pb collisions.

References

[1] D. H. Perkins, "Introduction to High Energy Physics". Cambridge University Press, 4 ed. (2000).

[2] S. Weinberg, "The making of the Standard Model," *Eur. Phys. J. C* **34** no. 1, (2004) 5–13.

[3] D. J. Griffiths, "Introduction to elementary particles; 2nd rev. version". Wiley, New York (2008). https://cds.cern.ch/record/111880.

[4] Standard Model of Elementary Particles – https://en.wikipedia.org/wiki/Standard_Model – accesed 07.01.2025.

[5] S. Navas *et al.*, [Particle Data Group Collab.], "Review of Particle Physics," *Phys. Rev. D* **110** (2024) 030001.

[6] M. K. Gaillard, P. D. Grannis, and F. J. Sciulli, "The Standard model of particle physics," *Rev. Mod. Phys.* **71** (1999) S96–S111, arXiv:hep-ph/9812285.

[7] G. Fantini, A. Gallo Rosso, F. Vissani, and V. Zema, "Introduction to the Formalism of Neutrino Oscillations," *Adv. Ser. Direct. High Energy Phys.* **28** (2018) 37–119, arXiv:1802.05781 [hep-ph].

[8] S. Bilenky, "Neutrino oscillations: From a historical perspective to the present status," *Nucl. Phys. B* **908** (2016) 2–13, arXiv:1602.00170 [hep-ph].

[9] P. Braun-Munzinger, V. Koch, T. Schäfer, and J. Stachel, "Properties of hot and dense matter from relativistic heavy ion collisions," *Phys. Rept.* **621** (2016) 76–126, arXiv:1510.00442 [nucl-th].

[10] R. Kara *et al.*, "Finite volume effects near the chiral crossover," *EPJ Web Conf.* **296** (2024) 14004, arXiv:2401.01169 [hep-lat].

[11] P. Braun-Munzinger and J. Wambach, "Phase diagram of strongly interacting matter," *Rev. Mod. Phys.* **81** (2009) 1031–1050, arXiv:0801.4256 [hep-ph].

[12] F. Becattini, J. Manninen, and M. Gazdzicki, "Energy and system size dependence of chemical freeze-out in relativistic nuclear collisions," *Phys. Rev. C* **73** (2006) 044905, arXiv:hep-ph/0511092 [hep-ph].

[13] T. Schuster *et al.*, [NA49 Collab.], "Event-by-Event Fluctuations and the Search for the Critical Point within the NA49 Experiment," *PoS* **CPOD2009** (2009) 029, arXiv:0910.0558 [nucl-ex].

[14] R. Singh, L. Kumar, P. K. Netrakanti, and B. Mohanty, "Selected Experimental Results from Heavy-Ion Collisions at LHC," *Adv. High Energy Phys.* **2013** (2013) 761474, arXiv:1304.2969 [nucl-ex].

[15] C. Markert, G. Torrieri, and J. Rafelski, "Strange Hadron Resonances: Freeze-Out Probes in Heavy-Ion Collisions," *AIP Conf. Proc.* **631** no. 1, (2002) 533, arXiv:hep-ph/0206260.

[16] C. Blume, "Is there Life after Hadronization? An Experimental Overview," *Acta Phys. Polon. B* **43** (2012) 577–586, arXiv:1111.7140 [nucl-ex].

[17] M. Abdallah *et al.*, [STAR Collab.], "K^{*0} production in Au+Au collisions at $\sqrt{s_{\rm NN}}$ = 7.7, 11.5, 14.5, 19.6, 27, and 39 GeV from the RHIC beam energy scan," *Phys. Rev. C* **107** no. 3, (2023) 034907, arXiv:2210.02909 [nucl-ex].

[18] S. Acharya *et al.*, [ALICE Collab.], "System-size dependence of the hadronic rescattering effect at energies available at the CERN Large Hadron Collider," *Phys. Rev. C* **109** no. 1, (2024) 014911, arXiv:2308.16115 [nucl-ex].

[19] B. Betz, "Jet Propagation and Mach-Cone Formation in (3+1)-dimensional Ideal Hydrodynamics,". Ph.D. Thesis, Goethe University Frankfurt, 2009. arXiv:0910.4114 [nucl-th].

[20] M. Gaździcki and M. I. Gorenstein, "On the Early Stage of Nucleus-Nucleus Collisions," *Acta Phys. Polon. B* **30** (1999) 2705, arXiv:hep-ph/9803462.

[21] M. Gazdzicki, M. Gorenstein, and P. Seyboth, "Onset of deconfinement in nucleus-nucleus collisions: Review for pedestrians and experts," *Acta Phys. Polon. B* **42** (2011) 307–351, arXiv:1006.1765 [hep-ph].

[22] A. Acharya *et al.*, [NA61/SHINE Collab.], "Spectra and mean multiplicities of π^- in *central* ^{40}Ar+^{45}Sc collisions at 13*A*, 19*A*, 30*A*, 40*A*, 75A and 150*A* GeV/*c* beam momenta measured by the NA61/SHINE spectrometer at the CERN SPS," *Eur. Phys. J. C* **81** no. 5, (2021) 397, arXiv:2101.08494 [hep-ex].

[23] K. Grebieszkow, [NA61/SHINE Collab.], "News from NA61/SHINE," in *XXXI International Conference on Ultra-relativistic Nucleus-Nucleus Collisions (Quark Matter 2025)*. 2025. https://indico.cern.ch/event/1334113/contributions/6209724.

[24] D. H. Perkins, "Particle Astrophysics". Oxford University Press, 2 ed. (2009).

[25] R. D. Pisarski, "Phenomenology of the chiral phase transition," *Phys. Lett. B* **110** (1982) 155–158.

[26] G. E. Brown and M. Rho, "Scaling Effective Lagrangians in a Dense Medium," *Phys. Rev. Lett.* **66** (1991) 2720–2723.

[27] G. E. Brown and M. Rho, "Chiral restoration in hot and/or dense matter," *Phys. Rept.* **269** (1996) 333–380, arXiv:hep-ph/9504250.

[28] A. Milov, "Light vector mesons," *Eur. Phys. J. C* **61** (2009) 721–728, arXiv:0809.3880 [nucl-ex].

[29] T. Anticic *et al.*, [NA49 Collab.], "$K^*(892)^0$ and $\bar{K}^*(892)^0$ production in central Pb+Pb, Si+Si, C+C and inelastic p+p collisions at 158*A* GeV," *Phys. Rev. C* **84** (2011) 064909, arXiv:1105.3109 [nucl-ex].

[30] J. Adams *et al.*, [STAR Collab.], "$K(892)^*$ resonance production in Au+Au and *p+p* collisions at $\sqrt{s_{\mathrm{NN}}}$ = 200 GeV at RHIC," *Phys. Rev. C* **71** (2005) 064902, arXiv:nucl-ex/0412019.

[31] B. I. Abelev *et al.*, [STAR Collab.], "Hadronic resonance production in d+Au collisions at $\sqrt{s_{\mathrm{NN}}}$ = 200 GeV measured at the BNL Relativistic Heavy Ion Collider," *Phys. Rev. C* **78** (2008) 044906, arXiv:0801.0450 [nucl-ex].

[32] M. M. Aggarwal *et al.*, [STAR Collab.], "K^{*0} production in Cu+Cu and Au+Au collisions at $\sqrt{s_{\mathrm{NN}}}$ = 62.4 GeV and 200 GeV," *Phys. Rev. C* **84** (2011) 034909, arXiv:1006.1961 [nucl-ex].

[33] M. Nasim, [STAR Collab.], "Probing QCD Matter via $K^{*0}(892)$ and $\phi(1020)$ Resonance Production at RHIC," *Springer Proc. Phys.* **250** (2020) 325–328, arXiv:1911.02270 [nucl-ex].

[34] A. K. Sahoo, [STAR Collab.], "Production Yield and Azimuthal Anisotropy Measurements of Strange Hadrons from BES at STAR," *Acta Phys. Polon. Supp.* **16** no. 1, (2023) 1–A132, arXiv:2209.04863 [hep-ex].

[35] S. K. Das *et al.*, "Dynamics of hot QCD matter – Current status and developments," *Int. J. Mod. Phys. E* **31** (2022) 12, arXiv:2208.13440 [nucl-th].

[36] B. B. Abelev *et al.*, [ALICE Collab.], "$K^*(892)^0$ and $\phi(1020)$ production in Pb-Pb collisions at $\sqrt{s_{\rm NN}}$ = 2.76 TeV," *Phys. Rev. C* **91** (2015) 024609, arXiv:1404.0495 [nucl-ex].

[37] J. Adam *et al.*, [ALICE Collab.], "$\mathrm{K}^*(892)^0$ and $\phi(1020)$ meson production at high transverse momentum in pp and Pb-Pb collisions at $\sqrt{s_{\rm NN}}$ = 2.76 TeV," *Phys. Rev. C* **95** no. 6, (2017) 064606, arXiv:1702.00555 [nucl-ex].

[38] D. S. D. Albuquerque, [ALICE Collab.], "Hadronic resonances, strange and multi-strange particle production in Xe-Xe and Pb-Pb collisions with ALICE at the LHC," *Nucl. Phys. A* **982** (2019) 823–826, arXiv:1807.08727 [hep-ex].

[39] S. Acharya *et al.*, [ALICE Collab.], "Evidence of rescattering effect in Pb-Pb collisions at the LHC through production of $\mathrm{K}^*(892)^0$ and $\phi(1020)$ mesons," *Phys. Lett. B* **802** (2020) 135225, arXiv:1910.14419 [nucl-ex].

[40] S. Acharya *et al.*, [ALICE Collab.], "Production of $\mathrm{K}^*(892)^0$ and $\phi(1020)$ in pp and Pb-Pb collisions at $\sqrt{s_{\rm NN}}$ = 5.02 TeV," *Phys. Rev. C* **106** no. 3, (2022) 034907, arXiv:2106.13113 [nucl-ex].

[41] A. Aduszkiewicz *et al.*, [NA61/SHINE Collab.], "$K^*(892)^0$ meson production in inelastic p+p interactions at 158 GeV/c beam momentum measured by NA61/SHINE at the CERN SPS," *Eur. Phys. J. C* **80** no. 5, (2020) 460, arXiv:2001.05370 [nucl-ex].

[42] S. Acharya *et al.*, [ALICE Collab.], "$K^*(892)^{\pm}$ resonance production in Pb-Pb collisions at $\sqrt{s_{\rm NN}}$ = 5.02 TeV," *Phys. Rev. C* **109** no. 4, (2024) 044902, arXiv:2308.16119 [nucl-ex].

[43] B. Kozłowski, [NA61/SHINE Collab.], "K^*/K ratio and the time between freeze-outs for intermediate-mass Ar+Sc system at the SPS energy range," *PoS* **ICHEP2024** (2025) 609, arXiv:2409.20229 [nucl-ex].

[44] H. Adhikary *et al.*, [NA61/SHINE Collab.], "Report from the NA61/SHINE experiment at the CERN SPS," Tech. Rep. CERN-SPSC-2024-030, SPSC-SR-353, CERN, Geneva, 2024. https://cds.cern.ch/record/2916893.

[45] N. Antoniou *et al.*, [NA49-Future Collab.], "Study of Hadron Production in Collisions of Protons and Nuclei at the CERN SPS," Tech. Rep. CERN-SPSC-2006-001, CERN-SPSC-P-329, CERN, Geneva, 2006. https://cds.cern.ch/record/919966.

[46] The CERN accelerator complex layout in 2022 – http://cds.cern.ch/record/2813716.

[47] NA61/SHINE library of images.

[48] K. Abe *et al.*, [T2K Collab.], "The T2K experiment," *Nucl. Instrum. Meth. A* **659** (2011) 106–135, arXiv:1106.1238 [physics.ins-det].

[49] K. Anderson *et al.*, "The NuMI Facility Technical Design Report," Tech. Rep. FERMILAB-DESIGN-1998-01, FERMILAB-TM-2406, FNAL, 1998. https://lss.fnal.gov/archive/test-tm/2000/fermilab-tm-2406.pdf.

[50] S. Johnson *et al.*, [NA61/SHINE Collab.], "Hadron Production Measurements for Fermilab Neutrino Beams," Tech. Rep. CERN-SPSC-2014-032, SPSC-P-330-ADD-7, CERN, Geneva, 2014. https://cds.cern.ch/record/1955140.

[51] P. Adamson *et al.*, [MINOS Collab.], "The MINOS Detectors Technical Design Report," Tech. Rep. NUMI-L-337, FERMILAB-DESIGN-1998-02, 1998. https://lss.fnal.gov/archive/design/fermilab-design-1998-02.pdf.

[52] J. Evans, [MINOS Collab.], "The MINOS Experiment: Results and Prospects," *Adv. High Energy Phys.* **2013** (2013) 182537, arXiv:1307.0721 [hep-ex].

[53] D. S. Ayres *et al.*, [NOvA Collab.], "NOvA: Proposal to Build a 30 Kiloton Off-Axis Detector to Study $\nu_\mu \to \nu_e$ Oscillations in the NuMI Beamline," arXiv:hep-ex/0503053.

[54] D. Drakoulakos *et al.*, [MINERvA Collab.], "Proposal to Perform a High-Statistics Neutrino Scattering Experiment using a Fine-grained Detector in the NuMI Beam," arXiv:hep-ex/0405002.

[55] H. Ray, [MINERvA Collab.], "MINERvA," *Acta Phys. Polon. B* **40** (2009) 2647–2652.

[56] R. Acciarri *et al.*, [DUNE Collab.], "Long-Baseline Neutrino Facility (LBNF) and Deep Underground Neutrino Experiment (DUNE): Conceptual Design Report, Volume 1: The LBNF and DUNE Projects," arXiv:1601.05471 [physics.ins-det].

[57] E. D. Zimmerman, "Results and future prospects of the NA61/SHINE neutrino program," in *CERN EP Seminar*. 2020. https://indico.cern.ch/event/958712.

[58] A. D. Marino, "Introduction to hadron production measurements for neutrino experiments," in *SHINE Autumn School @ CERN: Physics and Facility*. 2020. https://indico.cern.ch/event/963826/contributions/4060521.

[59] J. Abraham *et al.*, [Pierre Auger Collab.], "Properties and performance of the prototype instrument for the Pierre Auger Observatory," *Nucl. Instrum. Meth. A* **523** (2004) 50–95.

[60] G. Schatz, [KASCADE Collab.], "The KASCADE Cosmic Ray Experiment," *Nucl. Phys. B Proc. Suppl.* **43** (1995) 261–264.

[61] G. Navarra *et al.*, [KASCADE-Grande Collab.], "KASCADE-Grande: a large acceptance, high-resolution cosmic-ray detector up to 10^{18} eV," *Nucl. Instrum. Meth. A* **518** (2004) 207–209.

[62] T. Abu-Zayyad *et al.*, [Telescope Array Collab.], "The surface detector array of the Telescope Array experiment," *Nucl. Instrum. Meth. A* **689** (2013) 87–97, arXiv:1201.4964 [astro-ph.IM].

[63] R. Abbasi *et al.*, [IceCube Collab.], "IceTop: The surface component of IceCube," *Nucl. Instrum. Meth. A* **700** (2013) 188–220, arXiv:1207.6326 [astro-ph.IM].

[64] O. Adriani *et al.*, [PAMELA Collab.], "Measurement of boron and carbon fluxes in cosmic rays with the PAMELA experiment," *Astrophys. J.* **791** no. 2, (2014) 93, arXiv:1407.1657 [astro-ph.HE].

[65] M. Aguilar *et al.*, [AMS Collab.], "Precision Measurement of the Boron to Carbon Flux Ratio in Cosmic Rays from 1.9 GV to 2.6 TV with the Alpha Magnetic Spectrometer on the International Space Station," *Phys. Rev. Lett.* **117** no. 23, (2016) 231102.

[66] O. Adriani *et al.*, [CALET Collab.], "Cosmic-Ray Boron Flux Measured from 8.4 GeV/n to 3.8 TeV/n with the Calorimetric Electron Telescope on the International Space Station," *Phys. Rev. Lett.* **129** no. 25, (2022) 251103, arXiv:2212.07873 [astro-ph.HE].

[67] F. Alemanno *et al.*, [DAMPE Collab.], "Detection of spectral hardenings in cosmic-ray boron-to-carbon and boron-to-oxygen flux ratios with DAMPE," *Sci. Bull.* **67** (2022) 2162–2166, arXiv:2210.08833 [astro-ph.HE].

[68] A. Aduszkiewicz *et al.*, [NA61/SHINE Collab.], "Feasibility Study for the Measurement of Nuclear Fragmentation Cross Sections with NA61/SHINE at the CERN SPS," Tech. Rep. CERN-SPSC-2017-035, SPSC-P-330-ADD-9, CERN, Geneva, 2017. https://cds.cern.ch/record/2287004.

[69] M. Gaździcki, "NA61/SHINE Physics," in *NA61++/SHINE: Physics opportunities from ions to pions*. 2022. https://indico.cern.ch/event/1174830/contributions/5174343.

[70] N. Abgrall *et al.*, [NA61/SHINE Collab.], "NA61/SHINE facility at the CERN SPS: beams and detector system," *JINST* **9** (2014) P06005, arXiv:1401.4699 [physics.ins-det].

[71] H. Adhikary *et al.*, [NA61/SHINE Collab.], "Measurements of $\pi^{\pm}$, $K^{\pm}$, p and $\bar{p}$ spectra in ^{40}Ar+^{45}Sc collisions at 13A to 150A GeV/c," *Eur. Phys. J. C* **84** no. 4, (2024) 416, arXiv:2308.16683 [nucl-ex].

[72] A. Seryakov and E. Andronov, "Centrality selection for Ar+Sc analysis," in *NA61/SHINE and NA49 Collaboration Meeting in Baku (internal conference)*. 2016. https://indico.cern.ch/event/492269/contributions/2144869.

[73] K. Werner, "The hadronic interaction model EPOS," *Nucl. Phys. B Proc. Suppl.* **175-176** (2008) 81–87.

[74] T. Pierog and K. Werner, "EPOS Model and Ultra High Energy Cosmic Rays," *Nucl. Phys. B Proc. Suppl.* **196** (2009) 102–105, arXiv:0905.1198 [hep-ph].

[75] R. Ulrich, T. Pierog, and C. Baus, "The Cosmic Ray Monte Carlo Package, CRMC," 2021. https://doi.org/10.5281/zenodo.5270381.

[76] S. Agostinelli *et al.*, [GEANT4 Collab.], "GEANT4 – A Simulation Toolkit," *Nucl. Instrum. Meth. A* **506** (2003) 250–303.

[77] J. Allison *et al.*, "Geant4 Developments and Applications," *IEEE Trans. Nucl. Sci.* **53** (2006) 270.

[78] J. Allison *et al.*, "Recent developments in GEANT4," *Nucl. Instrum. Meth. A* **835** (2016) 186–225.

[79] A. Seryakov, "PSD acceptance maps for event selection." https://edms.cern.ch/document/1867336/1.

REFERENCES

[80] C. Höhne, "System-Size Dependence of Strangeness Production in Heavy-Ion Collisions at 158 *A*GeV,". PhD thesis, University of Marburg, 2003. https://doi.org/10.17192/z2003.0627.

[81] A. Acharya *et al.*, [NA61/SHINE Collab.], "$K^*(892)^0$ meson production in inelastic *p*+*p* interactions at 40 and 80 GeV/*c* beam momenta measured by NA61/SHINE at the CERN SPS," *Eur. Phys. J. C* **82** no. 4, (2022) 322, arXiv:2112.09506 [nucl-ex].

[82] Web page of ROOT package, https://root.cern.ch.

[83] A. Acharya *et al.*, [NA61/SHINE Collab.], "Measurements of $\Xi(1530)^0$ and $\overline{\Xi}(1530)^0$ production in proton–proton interactions at $\sqrt{s_{NN}}$ = 17.3 GeV in the NA61/SHINE experiment," *Eur. Phys. J. C* **81** no. 10, (2021) 911, arXiv:2105.09144 [nucl-ex].

[84] A. Aduszkiewicz *et al.*, [NA61/SHINE Collab.], "Measurements of $\pi^{\pm}$, $K^{\pm}$, p and $\bar{p}$ spectra in proton-proton interactions at 20, 31, 40, 80 and 158 GeV/*c* with the NA61/SHINE spectrometer at the CERN SPS," *Eur. Phys. J. C* **77** no. 10, (2017) 671, arXiv:1705.02467 [nucl-ex].

[85] C. Alt *et al.*, [NA49 Collab.], "System-Size Dependence of Strangeness Production in Nucleus-Nucleus Collisions at $\sqrt{s_{\rm NN}}$ = 17.3 GeV," *Phys. Rev. Lett.* **94** (2005) 052301, arXiv:nucl-ex/0406031.

[86] S. V. Afanasiev *et al.*, [NA49 Collab.], "Energy dependence of pion and kaon production in central Pb+Pb collisions," *Phys. Rev. C* **66** (2002) 054902, arXiv:nucl-ex/0205002.

[87] T. Anticic *et al.*, [NA49 Collab.], "Inclusive production of charged kaons in p+p collisions at 158 GeV/c beam momentum and a new evaluation of the energy dependence of kaon production up to collider energies," *Eur. Phys. J. C* **68** (2010) 1–73, arXiv:1004.1889 [hep-ex].

A Invariant mass distributions

Figures 57–68 show invariant mass distributions in rapidity and transverse momentum bins used in the analysis presented in this thesis.

A INVARIANT MASS DISTRIBUTIONS

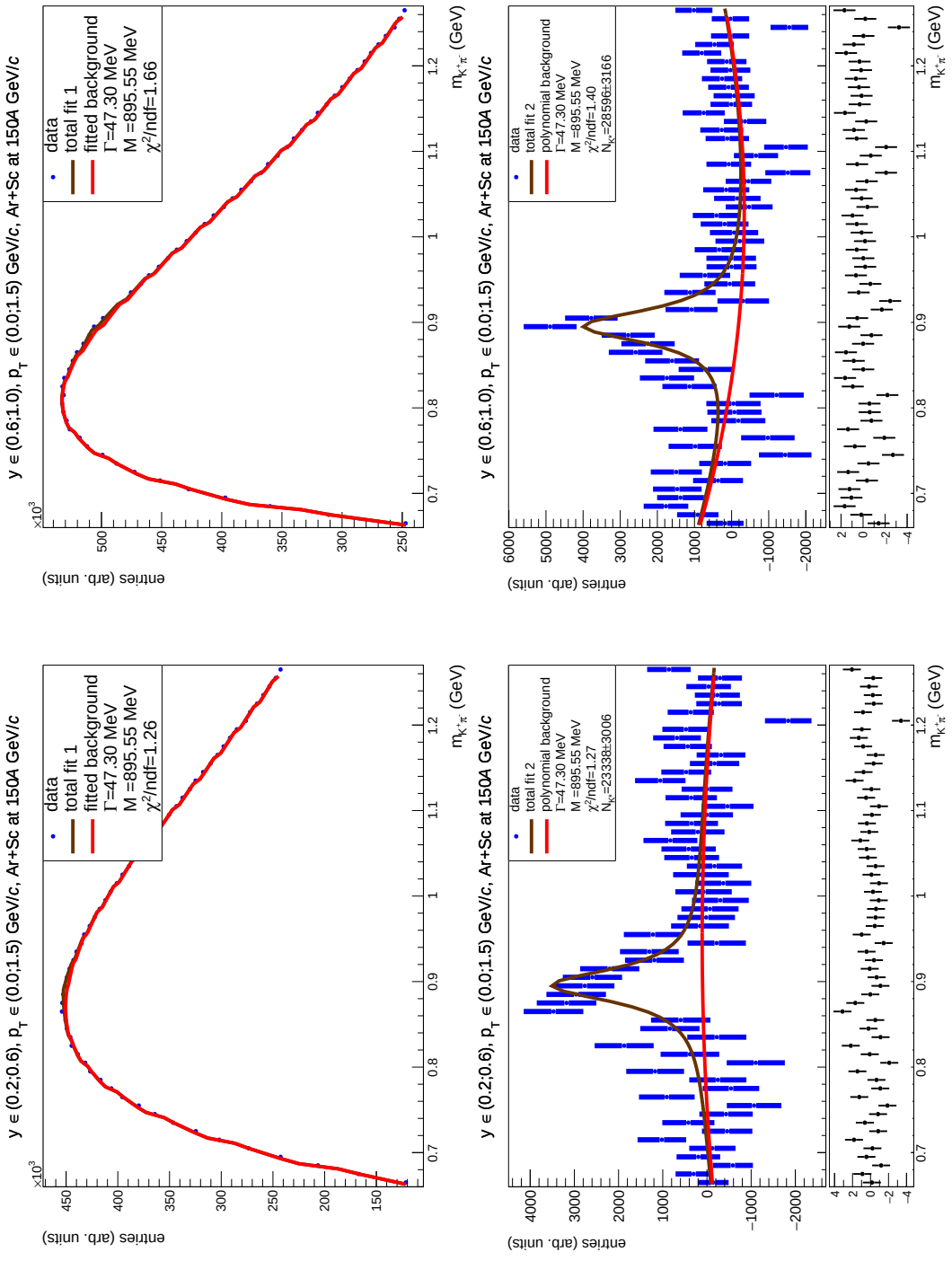

Figure 57: Invariant mass distributions in Ar+Sc collisions at beam momentum 150*A* GeV/*c*.

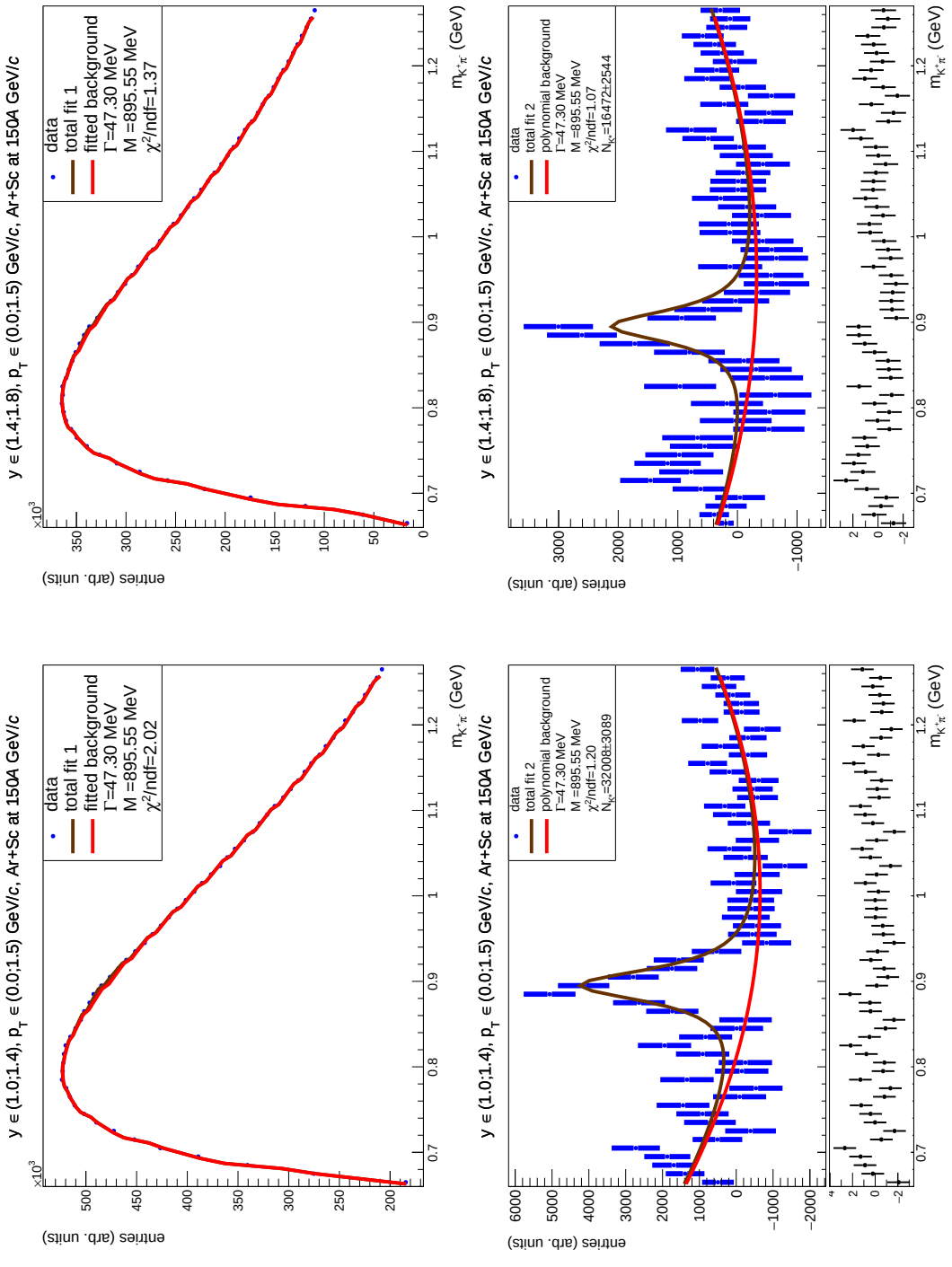

Figure 58: Invariant mass distributions in Ar+Sc collisions at beam momentum 150*A* GeV/*c*.

A INVARIANT MASS DISTRIBUTIONS

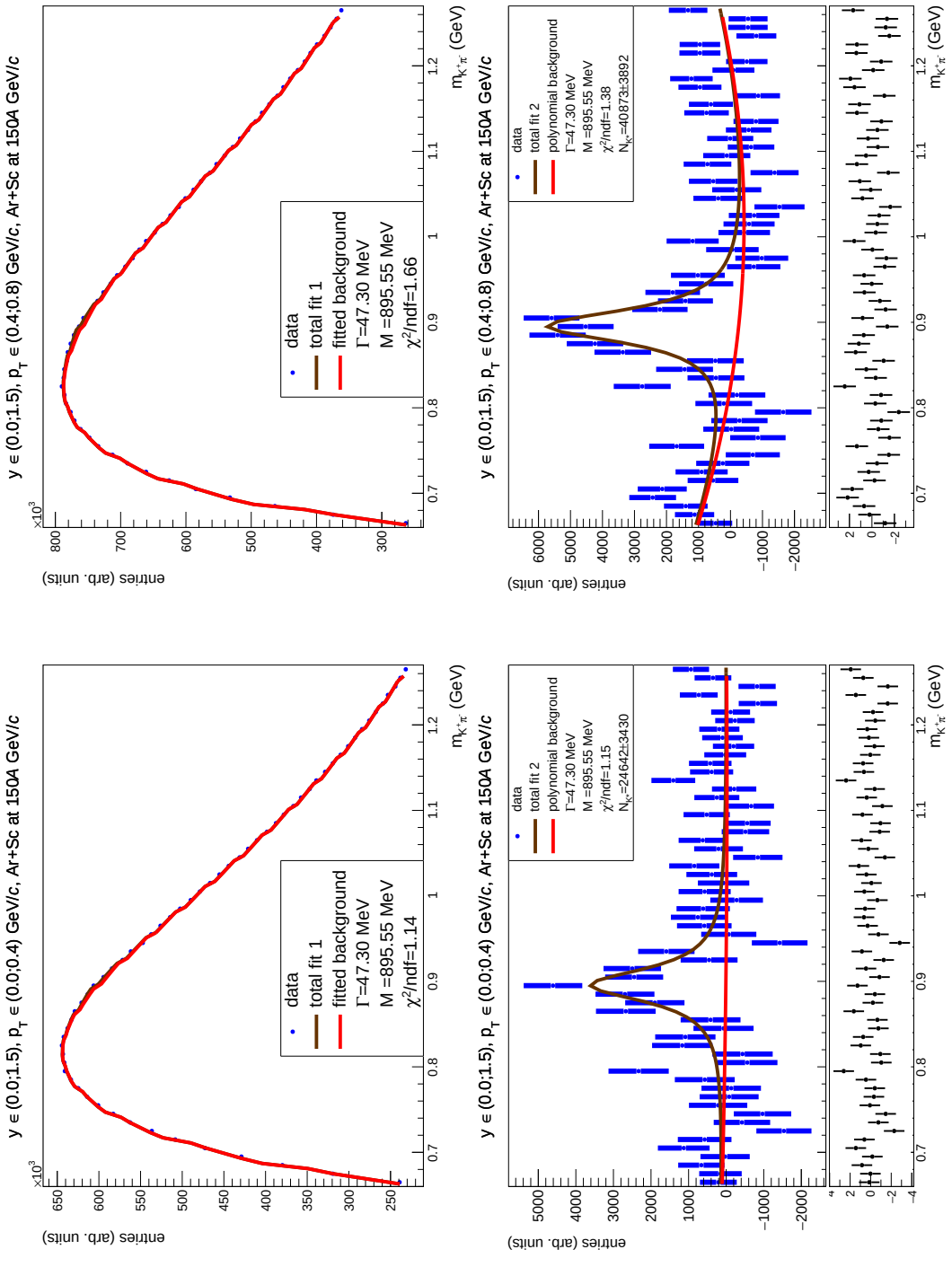

Figure 59: Invariant mass distributions in Ar+Sc collisions at beam momentum 150*A* GeV/*c*.

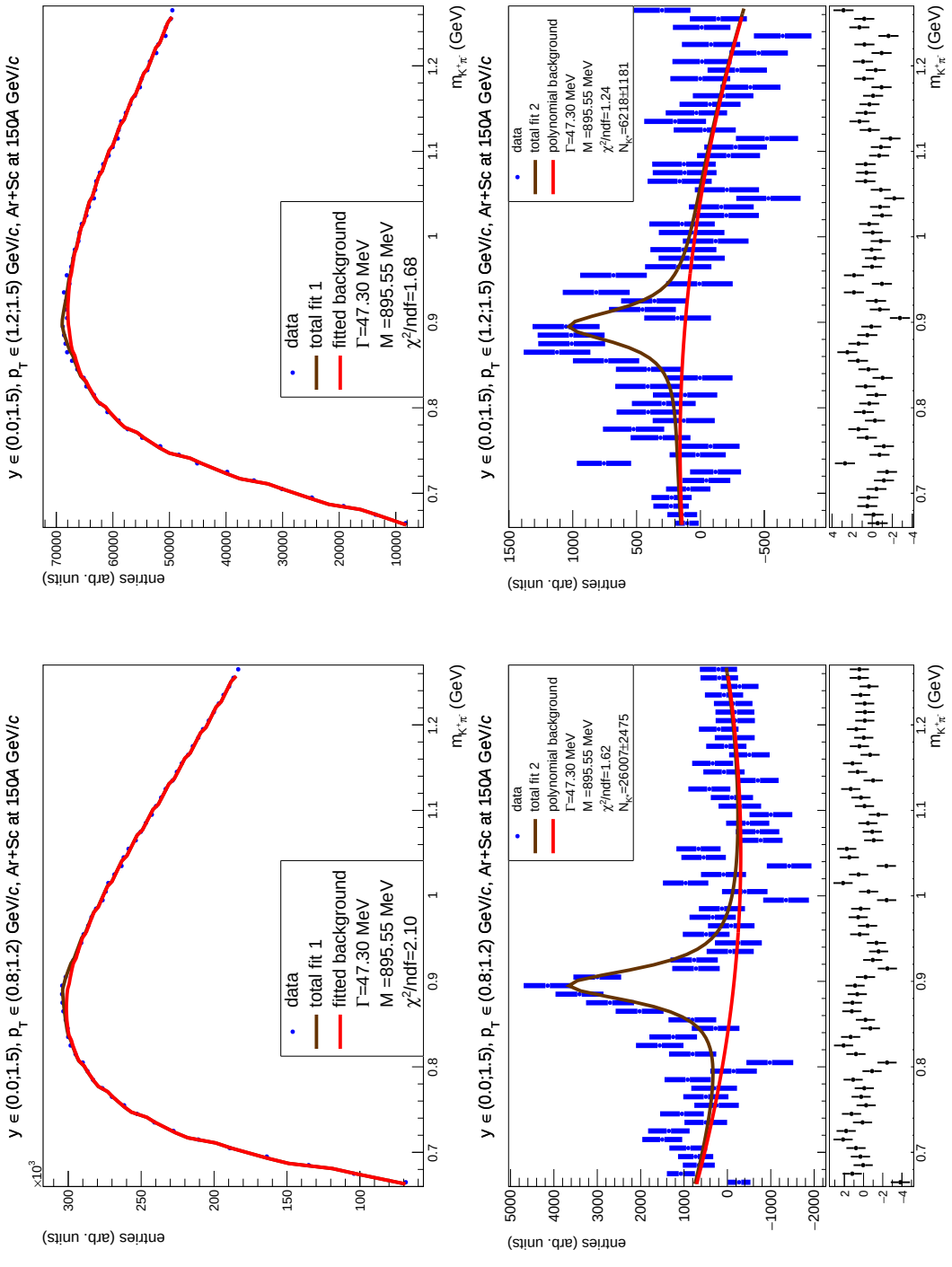

Figure 60: Invariant mass distributions in Ar+Sc collisions at beam momentum 150*A* GeV/*c*.

A INVARIANT MASS DISTRIBUTIONS

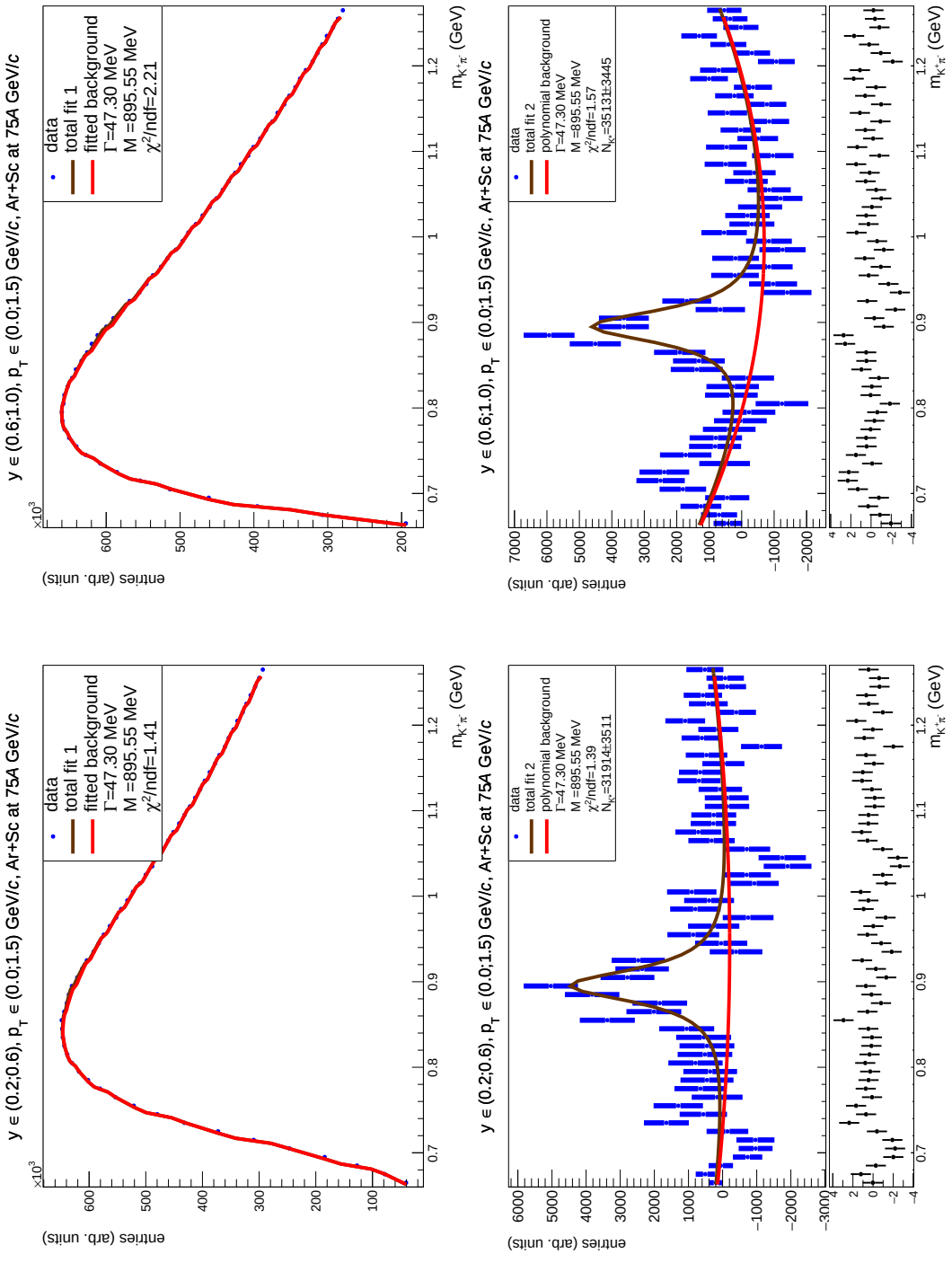

Figure 61: Invariant mass distributions in Ar+Sc collisions at beam momentum 75*A* GeV/*c*.

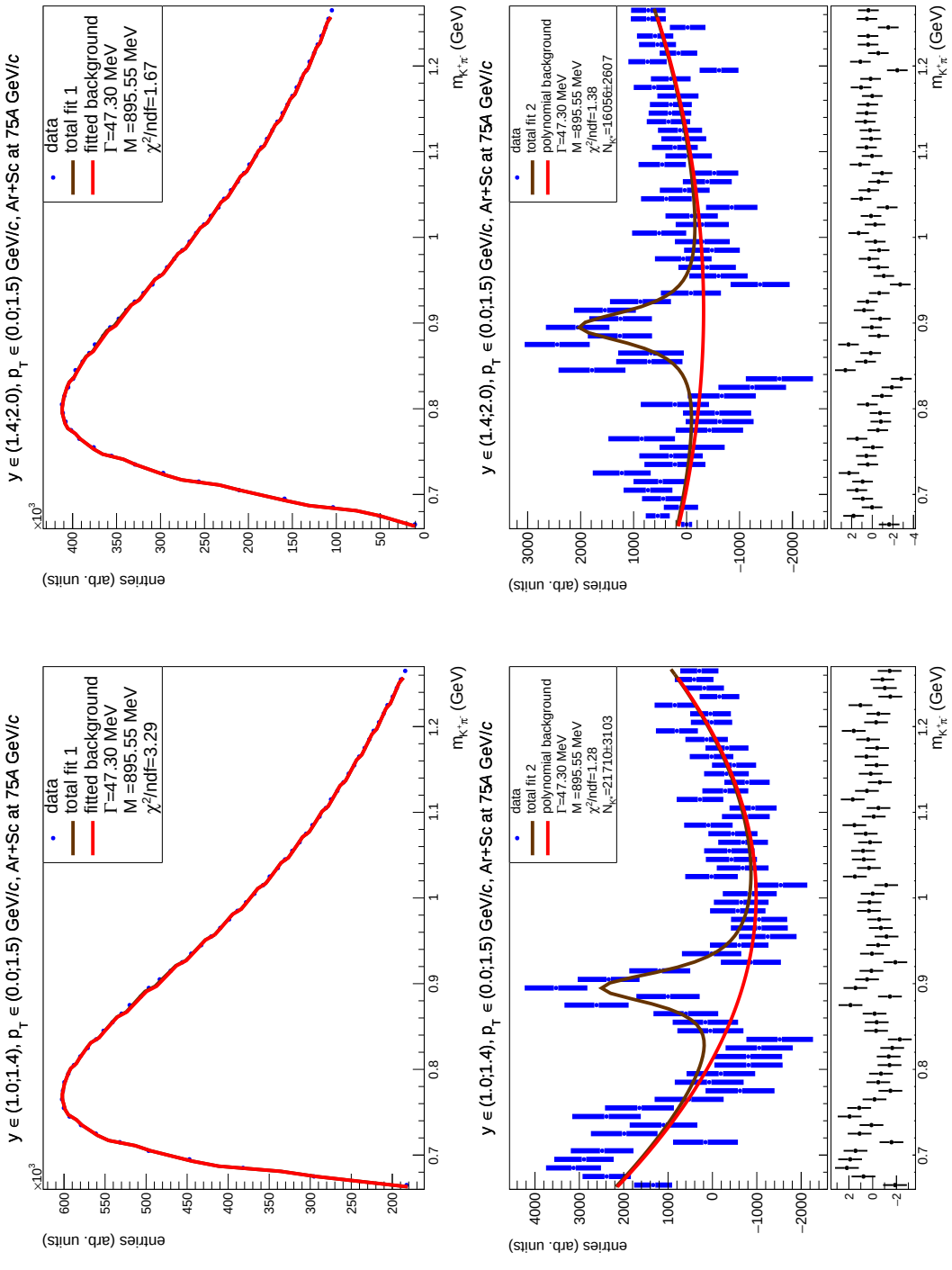

Figure 62: Invariant mass distributions in Ar+Sc collisions at beam momentum 75*A* GeV/*c*.

A INVARIANT MASS DISTRIBUTIONS

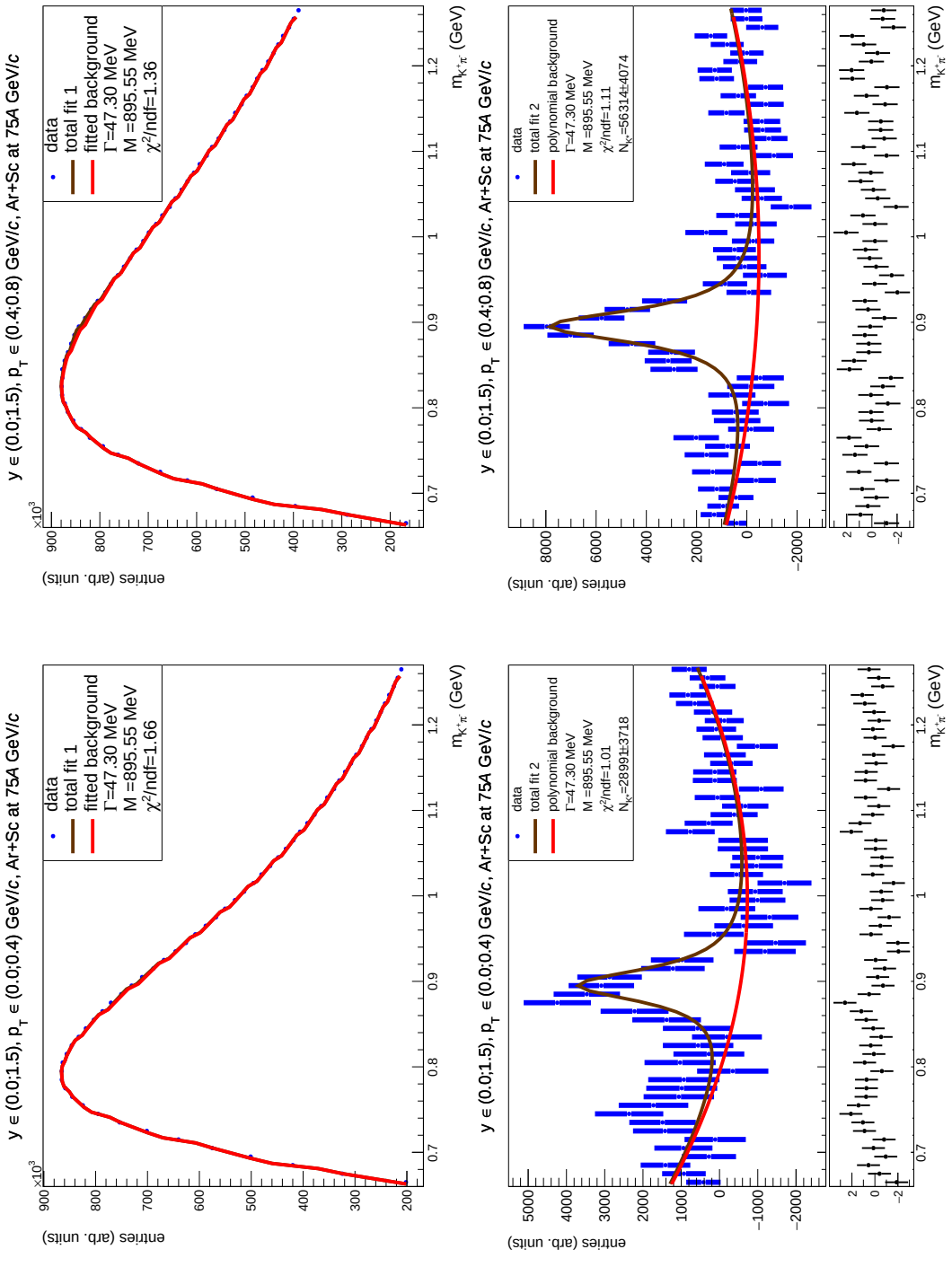

Figure 63: Invariant mass distributions in Ar+Sc collisions at beam momentum 75*A* GeV/*c*.

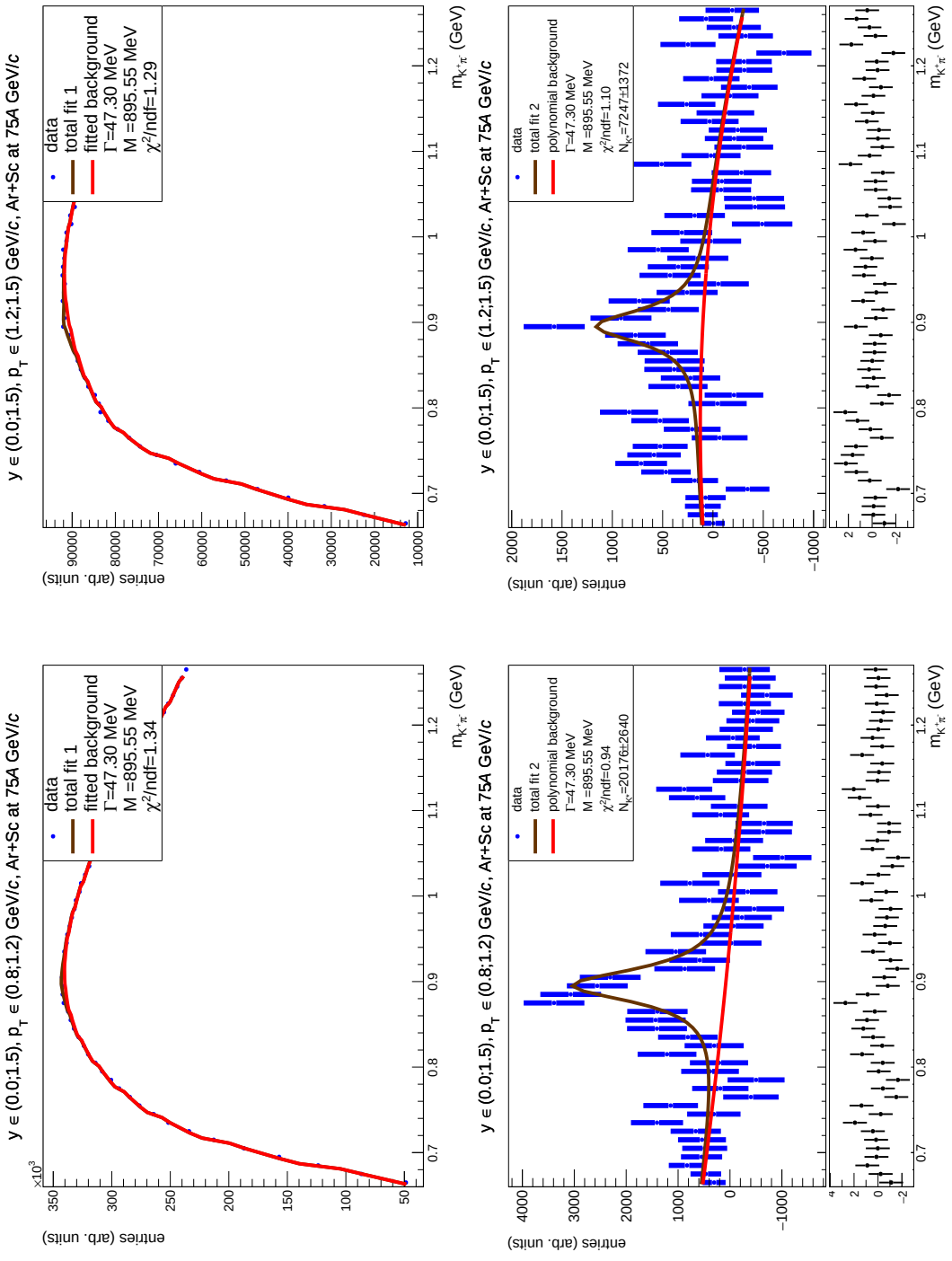

Figure 64: Invariant mass distributions in Ar+Sc collisions at beam momentum 75*A* GeV/*c*.

A INVARIANT MASS DISTRIBUTIONS

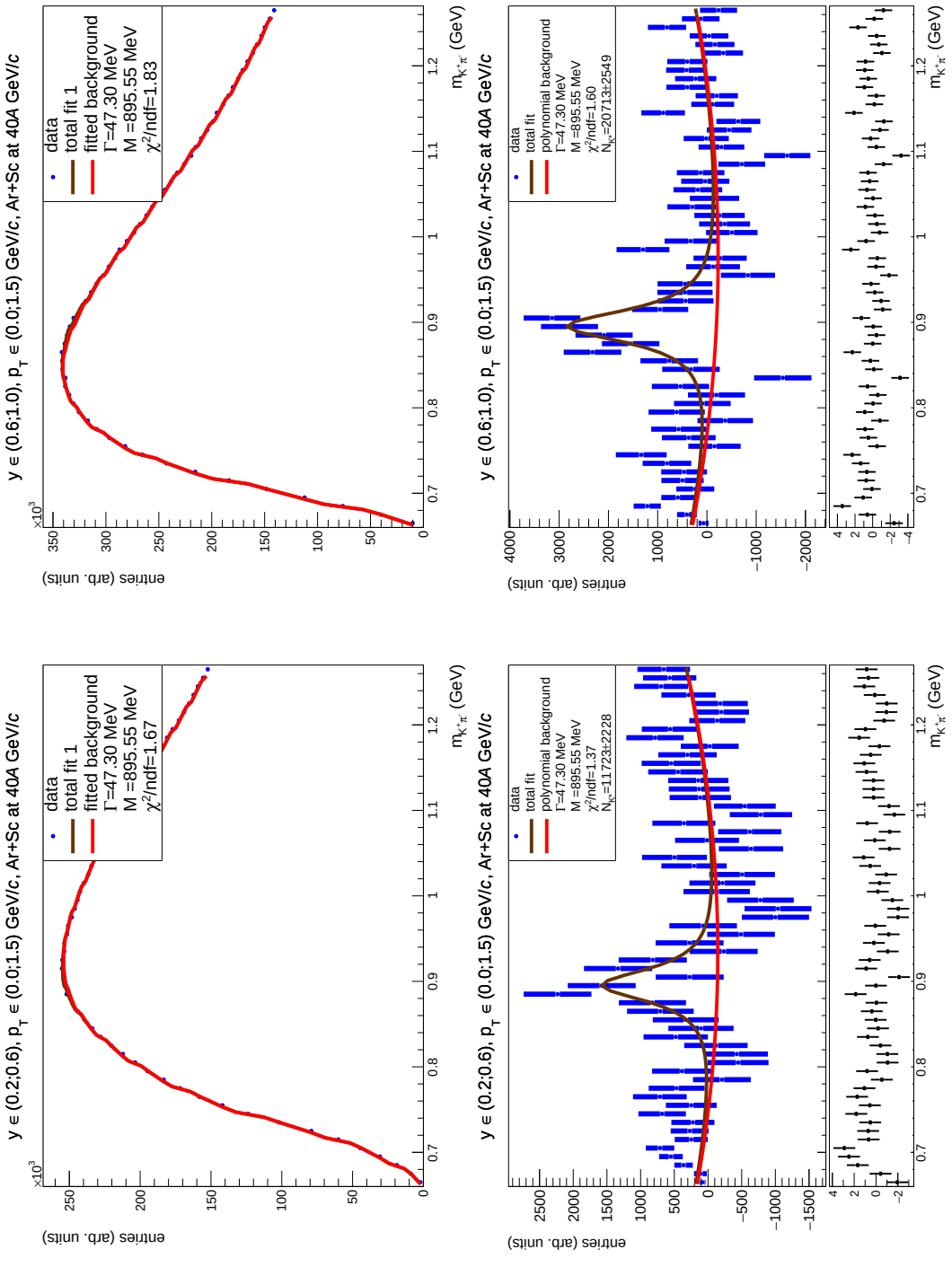

Figure 65: Invariant mass distributions in Ar+Sc collisions at beam momentum 40*A* GeV/*c*.

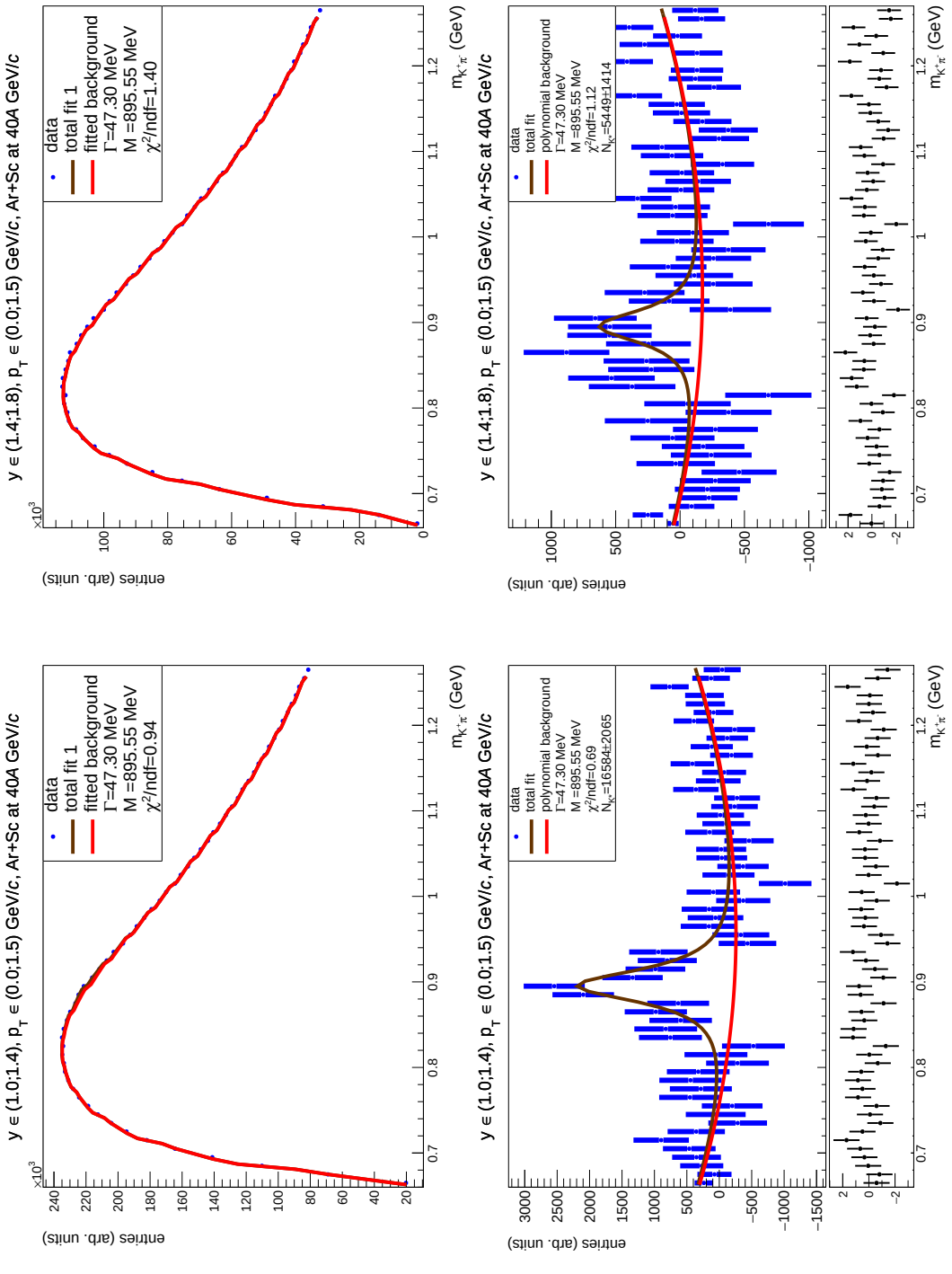

Figure 66: Invariant mass distributions in Ar+Sc collisions at beam momentum 40*A* GeV/*c*.

A INVARIANT MASS DISTRIBUTIONS

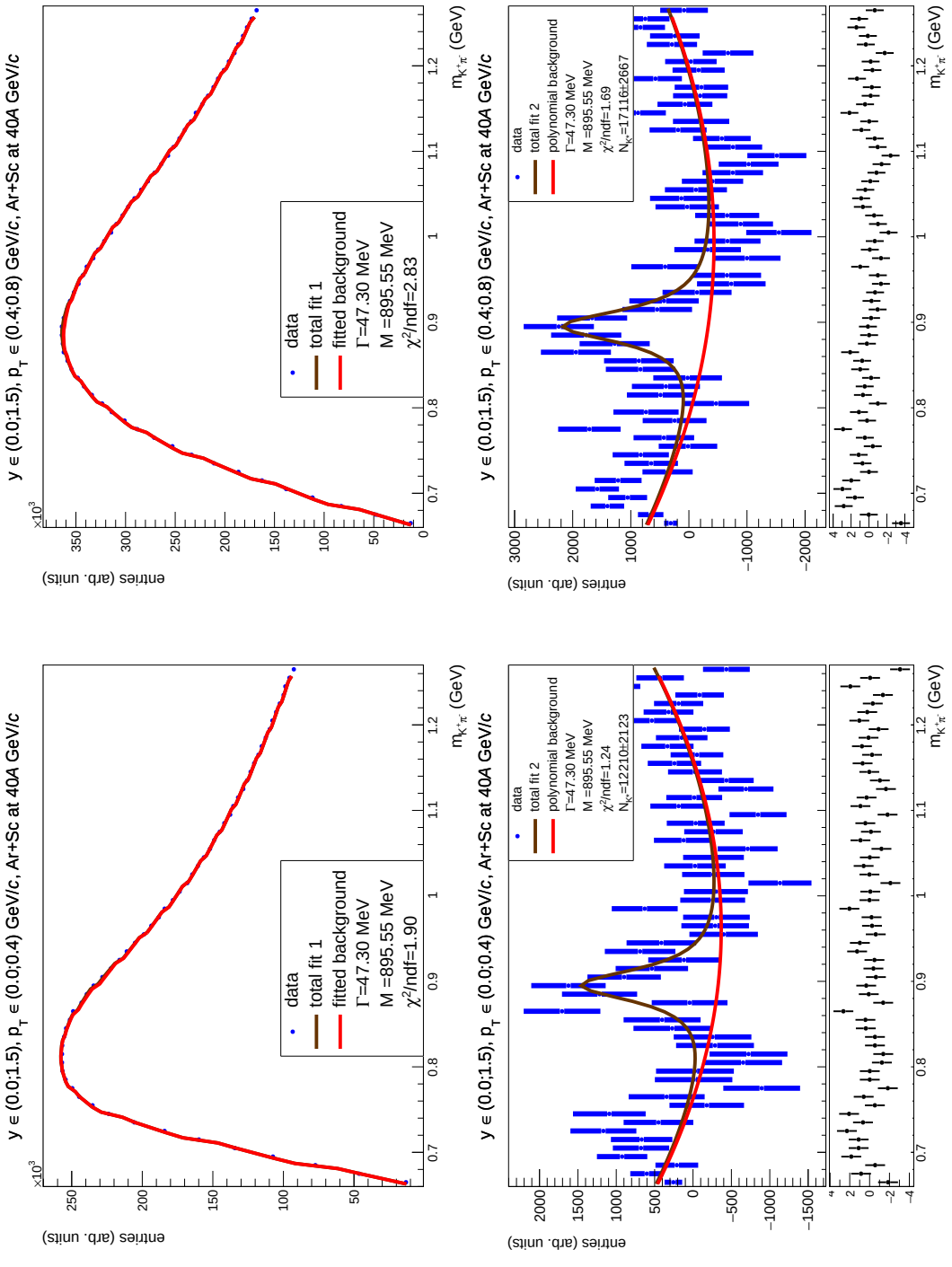

Figure 67: Invariant mass distributions in Ar+Sc collisions at beam momentum 40*A* GeV/*c*.

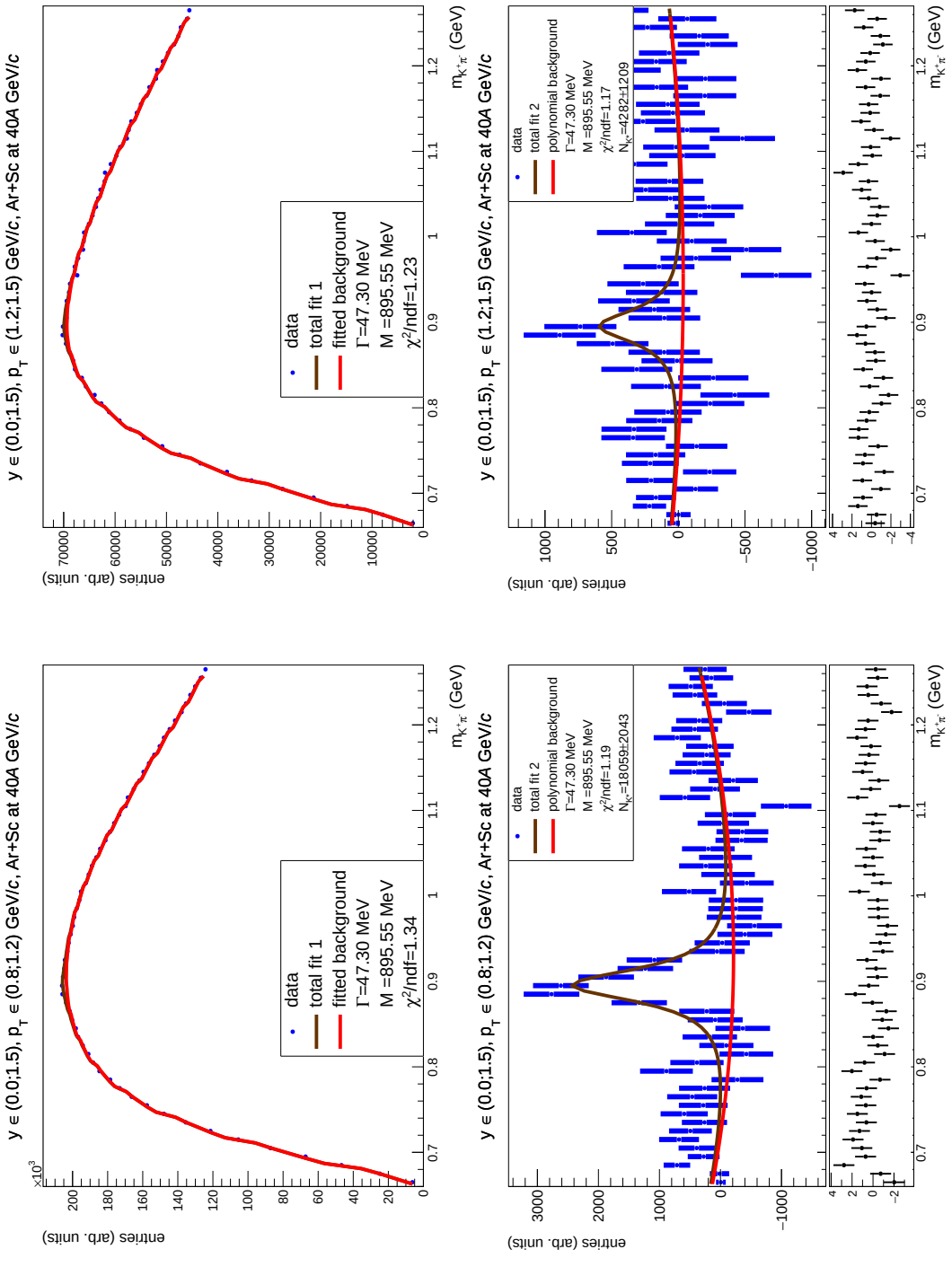

Figure 68: Invariant mass distributions in Ar+Sc collisions at beam momentum 40*A* GeV/*c*.